Magnetically-activated DNA and RNA

Ellen Parkes

Trinity College
University of Oxford

A thesis submitted for the degree of
Doctor of Philosophy

Trinity 2025

Abstract

Nucleic acids serve as the fundamental building blocks for life, encoding genetic information that enable organisms to function. Ground-breaking research translating nucleic acids into therapeutic modalities has culminated into more than 21 approved drugs, including the mRNA-based vaccines for COVID-19. Their simplicity in design and ability to target disease-causing genes that are deemed "undruggable" using conventional small molecules has accelerated research efforts. However, their susceptibility to nuclease degradation and anionic charge inhibiting cell internalisation has driven research into drug delivery strategies. A prevalent example is spherical nucleic acids, a delivery platform comprising nucleic acids radially arranged around a nanoparticle-based core that traverses the cell membrane and the blood-brain barrier. As fundamental building blocks, nucleic acids can be transformed into proteins through the process of transcription and translation for therapeutic effect. Recently, synthetic biology has been used to produce these therapeutic proteins inside the body, capitalising off synthetic cells as novel drug delivery devices. Synthetic cells have comparable dimensions to eukaryotic cells, comprising lipid bilayers that encapsulate a cell-free protein synthesis system and DNA templates that encode a desired function. The flexible design of synthetic cells increases their technological values, facilitating the production of pharmaceutically-relevant proteins by accommodating non-biological components, driving applications in drug delivery.

To realise the potential of these delivery platforms, the drug should be activated and/or released on-demand and targeted to a specific tissue. The ability to control the function of nucleic acids with an external stimulus is complementary to active targeting and holds promise for improving biodistribution in-vivo. An ideal stimulus is alternating magnetic fields, which are tissue-penetrating and biocompatible. Magnetic nanoparticles act as heating mediators and dissipate thermal energy in alternating magnetic fields. This heating, termed magnetic hyperthermia, is a clinical cancer therapy.

In this project, a novel delivery platform was designed, synthesised and validated, which exploited magnetic hyperthermia to control the function of nucleic acids. The design was inspired by the spherical nucleic acid architecture, whereby the installation of a superparamagnetic core enabled the heat dissipated in an alternating magnetic field to release bound DNA and activate a downstream process. Initially the platform was validated by controlling the release of an antisense oligonucleotide, influencing the on-demand degradation of target mRNA and selectively controlling gene knockdown with magnetic hyperthermia. The platform was then expanded to release the T7 promoter sequence and selectively control cell-free protein synthesis in an alternating magnetic field. These components were encapsulated inside a lipid bilayer, which enabled the in-situ production and release of cargo from within synthetic cells using magnetic hyperthermia. The magnetic regulation of gene expression throughout this project was achieved using clinically-tolerable magnetic field strengths and frequencies. The newly-developed delivery platform that harnessed magnetic hyperthermia to control the function of nucleic acids has the potential to revolutionise targeted drug delivery, activating the drug itself (in the case of antisense oligonucleotides) or catalysing the in-situ production and release of pharmaceutically-active molecules (in the case of synthetic cells) only at the target tissue.

Acknowledgements

I would like to express my sincerest gratitude to all those who contributed to my DPhil journey, your generosity and kindness has made me the researcher that I am today. First and foremost, I would like to thank my primary DPhil supervisor, Michael Booth. I am deeply grateful for your unwavering support and invaluable mentorship. Your proactivity in seeking-out opportunities has been instrumental in my career development and your open-mindedness has made the last four years a joy, enabling my creative vision to run wild. I have been extremely fortunate to work with brilliant scientists in the Booth group. Special mentions to Disha, you have been a constant throughout my DPhil, always making me feel seen, heard, and supported, having you has made this journey remarkably less solitary. To Giacomo and Charlie, you were instrumental in teaching me synthetic biology, a journey that was fraught with hurdles, but your influence meant that we always tackled them with such humour and positivity (most of the time). To Assala, a heartfelt thank you, your guidance and mentorship have been integral to the success of this project. To Denis and Jack, thank you for taking me under your wing in the early days, I am grateful for your efforts and patience in teaching me the fundamentals. Thank you to all the members of the Booth group and Office 230 (past and present), you continue to remind me the power of laughter.

I would like to thank the rest of my supervision team, Kylie Vincent and Yujia Qing, for their valuable advice and input throughout the project. I have truly learnt the importance of mentorship, in-particular I would like to thank the following: Emma Newton and Mark

Rackham for consistently being a guiding presence throughout this DPhil and my career thus far, you are inspirational to me; Richard England and his team at AstraZeneca for pouring their time and effort into my career development; Gemma-Louise Davies and Nguyen T. K. Thanh for their guidance on nanoparticle synthesis and magnetic hyperthermia. I would like to thank the EPSRC Centre for Doctoral Training in Inorganic Chemistry for Future Manufacturing for granting me this studentship, and the CDT management team for their unquestionable support throughout.

I would like to acknowledge my deeply supportive family; I am grateful for your belief in me, even when I lacked it myself. To Aunty Sophie and Uncle Darren, thank you for reminding me the importance of community – fuelling me with roast dinners, teaching me fire safety (or lack thereof), and always keeping me on the road (batteries and all). To my grandparents, Sue and Eric, thank you for gifting me the opportunity to pursue my interests and continuing to ground me in nature, one plant cutting at a time. To my parents and sister, Neal, Sarah, and Isobel; you inspire confidence within me, making me feel as though I belong, granting me the ability to take risks in my career and never failing to bring a smile to my face when I falter.

Thank you to my nephew/cat Leto; you came into my life at the optimal moment, reminding me that life is frivolous, naps are essential and grey squirrels are really tasty. Thank you to Evie and Ellie for your thoughtful nature, spurring me on with impromptu crafts and cups of tea, you have made our corner of the world a home.

Perhaps the most important thank you of all is to Felix, for whom has not only kept me sane, but enabled me to thrive throughout. Thank you for always lifting my spirits – evening strolls to our allotment, fermenting to ensure my gut microbiome is second to none, and maintaining a keen eye for my grammar slipups. You are integral to my contented life.

Published Work

The following paper has been published based on the work outlined in this thesis:

- **E. Parkes** *et al*., Magnetic activation of spherical nucleic acids enables the remote control of synthetic cells, *Nature Chemistry,* 2025, **17**, 1505-1513.

Abbreviations and Acronyms

θ	Bragg angle
α-HL	Alpha-hemolysin
β	Line broadening at the full half-width maximum of the most intense peak
β-Gal	β-galactosidase
ε	Molar extinction coefficient
ζ-potential	Zeta potential
ρ	Density
^{1}H NMR spectroscopy	Proton nuclear magnetic resonance spectroscopy
2′-F	2′-Fluoro
2′-MOE	2′-*O*-methoxyethyl
2′-OMe	2′-*O*-methyl
2-NBDG	2-(*N*-(7-nitrobenz-2-oxa-1,3-diazol-4-yl)amino)-2-deoxyglucose
3D	Three-dimensional
A	Adenosine
A site	Aminoacyl site
Abs	Absorbance
AGO2	Argonaute 2
AHSL	Acyl homoserine lactone
ALAS1	Aminolevulinic acid synthase
AMFs	Alternating magnetic fields
ApoE	Apolipoprotein E
APTES	3-aminopropyltriethoxysilane
ASGPR	Asialoglycoprotein receptor
ASO	Antisense oligonucleotide

ATP	Adenosine triphosphate
C	Cytosine
c_{DBCO}	Concentration of DBCO
CFPS	Cell-free protein synthesis
CNS	Central nervous system
dATP	Deoxyadenosine triphosphate
dCTP	Deoxycytidine triphosphate
dGTP	Deoxyguanosine triphosphate
dTTP	Deoxythymidine triphosphate
DBCO	Dibenzocyclooctyne
DCC	*N*,*N*'-dicyclohexylcarbodiimide
DFHBI	(*Z*)-4-(3,5-difluoro-4-hydroxybenzylidene)-1,2-dimethyl-1*H*-imidazol-5(4*H*)-one
dGFP	dasherGFP
DLin-DMA	1,2-dilinoleyloxy-*N*,*N*-dimethyl-3-aminopropane
DLS	Dynamic light scattering
DMPC	1,2-Dimyristoyl-*sn*-glycero-3-phosphocholine
DNA	Deoxyribonucleic acid
DOTMA	1,2-di-*O*-octadecenyl-3-trimethylammonium-propane
dsDNA	Double stranded deoxyribonucleic acid
DSPC	1,2-distearoyl-*sn*-glycero-3-phosphocholine
D_{XRD}	Crystallite diameter
E site	Exit site
E. coli	*Escherichia coli*
Egg-PC	Egg phosphatidyl choline
ELISA	Enzyme-linked immunosorbent assay
EMA	European Medicines Agency
EtOAc	Ethyl acetate
ExoT	Pseudomonas *aeruginosa* exotoxin T
f	Magnetic frequency
FDA	U.S. Food and Drug Administration
FDG	Fluorescein di-β-d-galactopyranoside

G	Guanine
GalNAc	*N*-acetylgalactosamine
GFP	Green fluorescent protein
GM3S	Ganglioside-monosialic acid 3 synthase
GUVs	Giant unilamellar vesicles
H	Magnetic field strength
HEPES	2-(4-(2-hydroxyethyl)piperazin-1-yl)ethanesulfonic acid
HER2	Human epithelial growth factor receptor 2
HOX	Homeobox
IGEPAL-*co*-520	Polyoxyethylene-5-nonylphenylether
IONPs	Iron oxide nanoparticles
IONPs@SiO_2	Iron oxide silica core-shell nanoparticles
IV-CoA	Isovaleryl coenzyme A
IV-HSL	*N*-isovaleryl-L-homoserine lactone
IVT	In-vitro transcription
K	Crystallite-shape factor
KMT2A	Lysin methyltransferase 2A
l	Path length
LCST	Lower critical solution temperature
LDLR	Low-density lipoprotein receptor
LNA	Locked nucleic acid
LNPs	Lipid nanoparticles
χmax	Maximum Mmagnetic susceptibility
M_C	Mass concentration of nanoparticles
$m_{core\text{-}shell}$	Mass of the individual core-shell nanoparticle
MHRA	United Kingdom Medicines and healthcare Products Regulatory Agency
miRNA	Micro ribonucleic acid
mNG	mNeonGreen
MOPS	3-morpholinopropane-1-sulfonic acid
MRI	Magnetic resonance imaging
mRNA	Messenger ribonucleic acid

N_A	Avogadro's number
$N_{\text{core-shell}}$	Number of nanoparticles
N_{DBCO}	Number of molecules of DBCO
NHS ester	*N*-hydroxysuccinimide ester
NIR	Near-infrared
$Ø_{\text{bore}}$	Internal diameter of a solenoid coil
P site	Peptidyl site
PAGE	Poly(acrylamide) gel electrophoresis
PCR	Polymerase chain reaction
PDI	Polydispersity index
PE	Petroleum ether
PEG	Poly(ethylene glycol)
PFO	Perfringolysin O
PMO	Phosphorodiamidate morpholino oligomer
PNA	Peptide nucleic acid
POPC	1-palmitoyl-2-oleoyl-*sn*-glycero-3-phospholipid
PSar	Poly(sarcosine)
PURE	Protein synthesis using recombinant elements
r_{core}	Radius of the nanoparticle core
$r_{\text{core-shell}}$	Radius of the nanoparticle core-shell
RES	Reticuloendothelial system
RF1	Single release factor
RISC	Ribonucleic acid-induced silencing complex
RNA	Ribonucleic acid
RNAi mechanism	Ribonucleic acid interference mechanism
RNase H	Ribonuclease H
rt-qPCR	Reverse transcription quantitative polymerase chain reaction
SARS-CoV-2	Severe acute respiratory syndrome coronavirus 2
SD	Shine-Dalgarno sequence
siRNA	Small interring ribonucleic acid
SMN1	Survival motor neuron 1
SNAs	Spherical nucleic acids

SPAAC	Strain-promoted azide-alkyne cycloaddition
SPR	Surface plasmon resonance
ssDNA	Single stranded deoxyribonucleic acid
SQUID	Superconducting quantum interference device
T	Thymine
TBE	Tris-Borate-EDTA
TE	Tris-ethylenediaminetetraacetic acid
TEM	Transmission electron microscopy
TEOS	Tetraethylorthosilicate
T_m	Melting temperature
TNF-α	Tumour necrosis factor-alpha
tRNA	Transfer ribonucleic acid
TXR	Texas Red™ dextran
U	Uracil
UV	Ultraviolet
UV-vis	Ultraviolet-visible
v/v	Volume/volume
VLPs	Virus-like particles
w/o	Water-in-oil
w/v	Weight/volume
XRD	X-ray diffraction

Contents

1

Introduction

1.1. Structure and function of nucleic acids

1.1.1. DNA structure

Nucleic acids serve as the fundamental building blocks for life, encoding the genetic information that enable organisms to function. Deoxyribonucleic acid (DNA) comprises monomeric units, termed nucleotides, which in-turn consist of a five-carbon deoxyribose sugar molecule in combination with a nitrogen-containing base (cytosine, guanine, adenosine or thymine) and a phosphate group (Fig. 1.1A).

The nitrogen-containing base is covalently bound to the 1′-carbon of the deoxyribose molecule, denoted the *N*-glycosidic bond, and a phosphodiester bond links the 3′-hydroxyl of the sugar molecule to the 5′-hydroxyl of the next molecule to grow a polymer chain with a phosphate backbone. The chain terminates such that there is an exposed 5′-hydroxyl at one end and 3′-hydroxyl at the other.

Two DNA polymer chains form a right-handed double helix through Watson-Crick-Franklin base pairing, in which hydrogen bonds are formed between adenine and thymine bases, and separately guanine and cytosine bases. The nitrogen-containing bases reside in the middle of the double helix, with the phosphate backbone off-set to form major and minor grooves along the helical axis (Fig. 1.1B) [1,2].

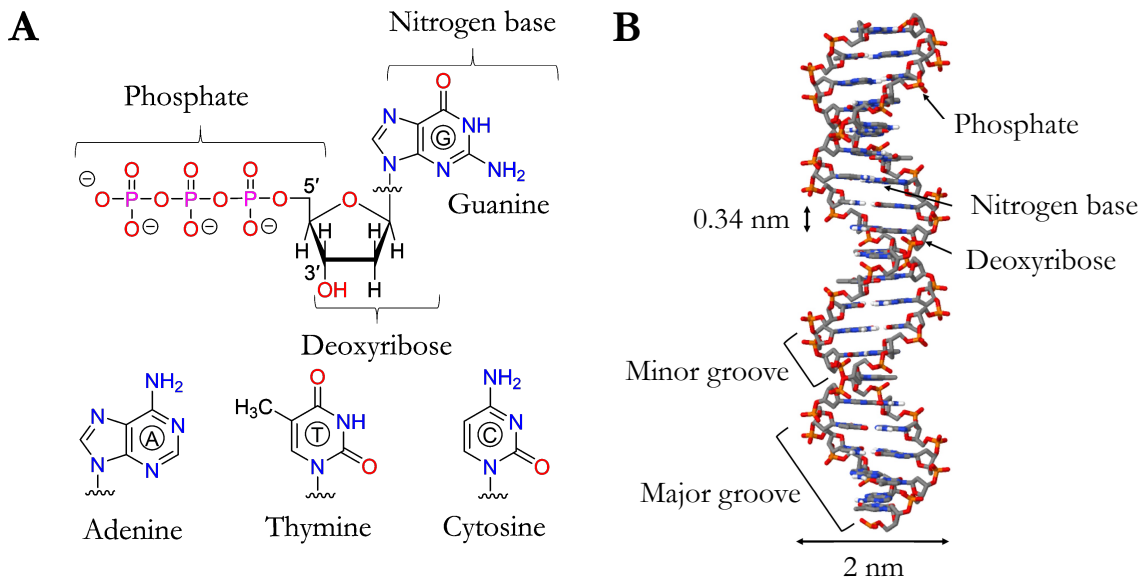

Fig. 1.1 Chemical structure of DNA. (A) DNA nucleotide comprising a five-carbon deoxyribose sugar molecule, a nitrogen-containing base (cytosine, guanine, adenosine or thymine) and a phosphate group. **(B)** DNA double helix showing the major and minor grooves. Figure 1B adapted from "Understanding biochemistry: structure and function of nucleic acids" by Minchin and Lodge.[1] (© 2019) under a creative commons license (CC-BY 4.0).

1.1.2. DNA replication

DNA replication is an intricate process that remains functionally conserved across all cellular life, proving crucial for the inheritance of genetic information. DNA replication has a high degree of accuracy, achieved in-part by replication machinery termed replisomes, multiprotein complexes that encompass helicase, primase and DNA polymerase activities [3]. A replicative helicase enzyme, fuelled by the hydrolysis of adenosine triphosphate (ATP), catalyses the unwinding of parental double-stranded DNA (dsDNA) at the origin of replication (Fig. 1.2) [4,5]. The origin of replication is a unique sequence that acts as a specific binding site for proteins that initiate the replication process, leading to the formation of the diverging replication fork [6]. The running replication fork separates into two DNA strands and the synthesis of leading and lagging strands is initiated by DNA polymerase [7]. The leading strand is continuously synthesised and the lagging strand is synthesised in discontinuous pieces, denoted Okazaki fragments, which are joined by the action of DNA ligase [6]. Individual DNA building blocks, deoxynucleotide triphosphates (dATP, dTTP, dCTP, and dGTP) form hydrogen bonds with their complementary base on the single-stranded DNA (ssDNA) template. A phosphodiester bond is formed between the 5′-hydroxyl of the incoming nucleotide and the free 3′-hydroxyl on the existing template strand, releasing pyrophosphate as the by-product [1]. The accuracy of DNA replication is ascribed to the proofreading ability of DNA polymerase and the ability to selectively excise mismatched bases that have been incorporated at the end of the growing DNA chain [6]. DNA replication is terminated when converging replication forks meet and the replisome disassembles [7].

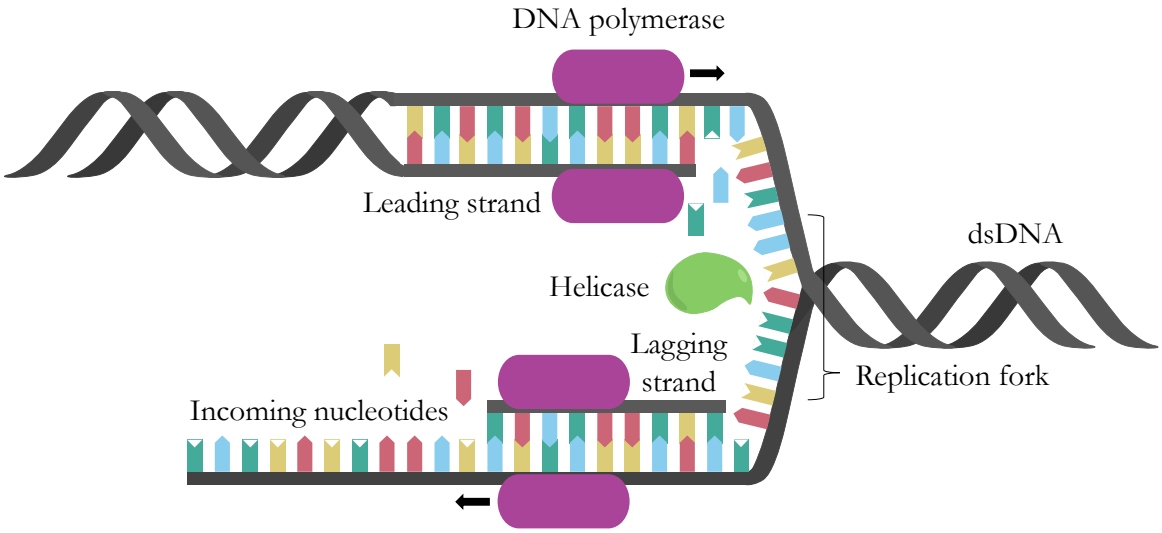

Fig. 1.2. Schematic of DNA replication. Helicase unwinds the parental dsDNA to form the replication fork. DNA polymerase initiates the synthesis of the leading and lagging strands, whereby the leading strand is continuously synthesised and the lagging strand is synthesised in discontinuous pieces (Okazaki fragments). A phosphodiester bond is formed between the incoming deoxynucleotide triphosphates (dATP, dTTP, dCTP, and dGTP) and the 3′-hydroxyl on the existing template strand, releasing pyrophosphate and synthesising the DNA chain.

1.1.3. DNA transcription and RNA structure

The genetic information stored in DNA is transcribed into ribonucleic acid (RNA), which acts as a genetic messenger during protein synthesis. RNA comprises a five-carbon ribose sugar molecule, a nitrogen-containing base (cytosine, guanine, adenosine or uracil) and a phosphate group (Fig. 1.3). The chemical structure of RNA is somewhat similar to DNA with the nitrogen-containing base covalently bound to the ribose molecule and a phosphodiester bond linking the 3′-hydroxyl of the ribose molecule to the 5′-hydroxyl of the next molecule. In contrast to DNA, RNA molecules degrade more readily [1]. Transcription and the regulation of gene expression is a major facilitator of cell differentiation, homoeostasis and speciation [1].

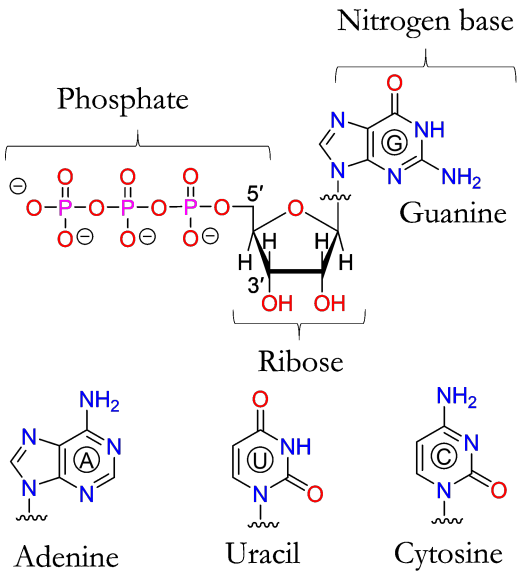

Fig. 1.3. Chemical structure of RNA nucleotides. RNA nucleotide comprising a five-carbon ribose sugar molecule, a nitrogen-containing base (cytosine, guanine, adenosine or uracil) and a phosphate group.

The DNA-binding protein, RNA polymerase, transcribes DNA into RNA in the 5′ to 3′ direction. RNA polymerase is primer-independent and binds upstream of the target gene. The elongating RNA polymerase interacts and unwinds the parental dsDNA to form an active transcription pocket (Fig. 1.4). The RNA molecule being synthesised, known as nascent RNA, forms a dynamic DNA-RNA heteroduplex (9 to 11 nucleotides in length) through Watson-Crick-Franklin base-pairing, reforming the double strand once the polymerase has passed through [5]. This unwinding leads to positive and negative supercoiling, defined as the torsional stress on the double helix through overtwisting or under-twisting, ahead and behind the RNA polymerase that is relieved by DNA topoisomerases [8]. RNA polymerase is able to disengage the 3′-end of the RNA molecule from the active transcription pocket, regulating transcription progression and 'backtracking' to remove the last nucleotide [9]. Transcription is terminated by the incorporation of termination signals that influence the dissociation of RNA polymerase, and the release of the intact RNA product. A prominent example in bacteria is the incorporation of A – T

nucleotide pairs preceding a symmetric DNA sequence that is transcribed into an RNA "hairpin" structure, sterically-aiding the release of the RNA transcript from the polymerase exit tunnel [10]. In bacteria, RNA polymerase binding is controlled by transcription factors and upstream from the transcription start site is marked by a specific DNA "promoter" sequence.

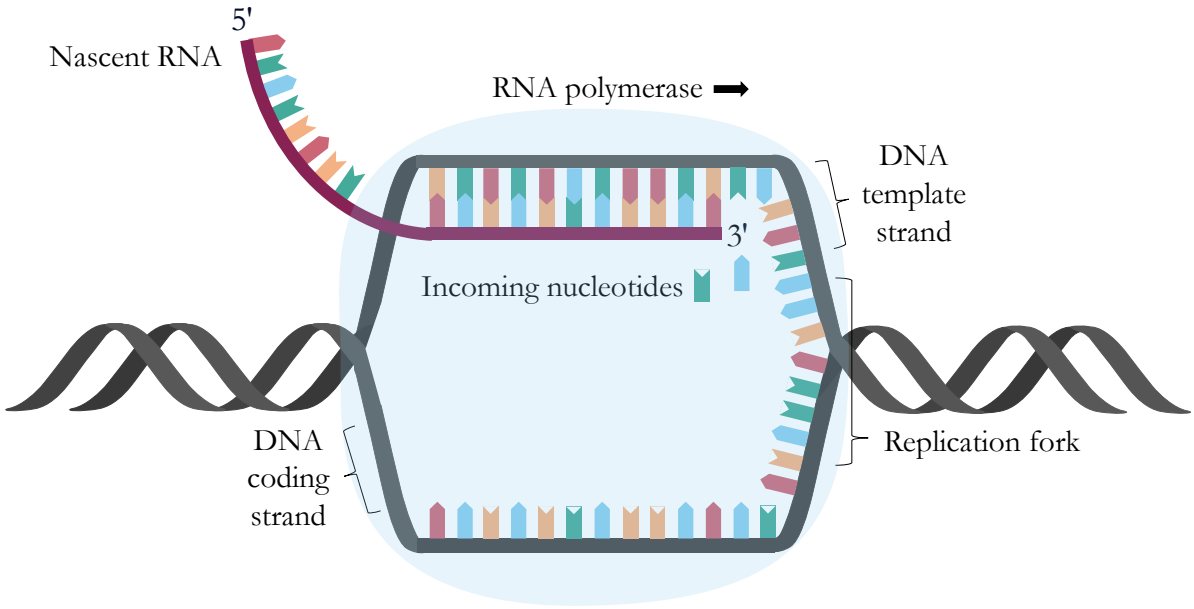

Fig. 1.4. Schematic of DNA transcription. RNA polymerase unwinds the parental dsDNA to form an active transcription pocket. Hydrogen bonding between the incoming nucleotide and its complementary base pair on the DNA template allows for the formation of the phosphodiester bond. The double strand is reformed once the polymerase has passed through. Transcription is then terminated by incorporating termination signals that influence the dissociation of RNA polymerase and allow for the release of the intact RNA product.

1.1.4. RNA translation

It should be emphasised that not all functional RNAs are translated into proteins. Many non-coding RNAs exist such as transfer RNAs (tRNAs), ribosomal RNAs, small interfering RNAs (siRNAs), and microRNAs (miRNAs). tRNAs are single stranded adapter molecules that are critical in the translation of messenger RNA (mRNA) into amino acid sequences and their folding into proteins. They function by carrying an anticodon that is complimentary

to a specific mRNA codon (which is defined as a sequence of three nucleotides that encodes a particular amino acid [11]). There are 64 different trinucleotide codons: 61 specify amino acids and three are stop codons (UAA, UAG and UGA) that signal to the ribosome to halt protein synthesis [1]. The most common start codon (AUG) encodes the amino acid methionine, which is the first amino acid residue in all eukaryotic proteins [12]. Aminoacyl tRNA synthetase activates the 3′-hydroxyl of tRNA with the anticodon (methionine initially).

Protein synthesis can be defined by three phases: initiation, elongation, and termination. Initiation describes recruitment of initiation factors, methionyl tRNA, and the small ribosomal subunit to the mRNA (Fig. 1.5). The small ribosomal subunit, in association with the methionyl tRNA, scans along the 5′-untranslated region of mRNA until the first AUG start codon is identified [13]. The large ribosomal subunit then docks to complete the translation complex. Translation then proceeds by elongation of the polypeptide chain, directed by the three ribosome-binding sites for tRNA including the P (peptidyl), A (aminoacyl), and E (exit) sites [13]. The first step is achieved by the next aminoacyl tRNA binding to the A site and pairing with the second mRNA codon, whereby a peptide bond is formed between the initiator methionyl tRNA (now in the P site) and the aminoacyl tRNA (in the A site). The methionine is transferred to the aminoacyl tRNA in the A site prior to a process called translocation, where the ribosome moves three nucleotides along the mRNA (one codon). The peptidyl tRNA with the growing chain translocates from the A site to the P site and the spent tRNA translocates from the P site to the E site. The binding of a new aminoacyl tRNA to the A site induces the release of the spent tRNA from the E site, where it leaves the ribosome [13]. This process continues until a stop codon (UAA, UAG or UGA) is read in the A site. The final phase, termination, is when the release factor protein (single release factor (RF1) in the case of eukaryotes) enters the A site and the ester bond linking

the peptide chain to the tRNA in the P site is broken. The newly-synthesised peptide is released from the ribosome and the two ribosomal subunits disassociate and are recycled [1].

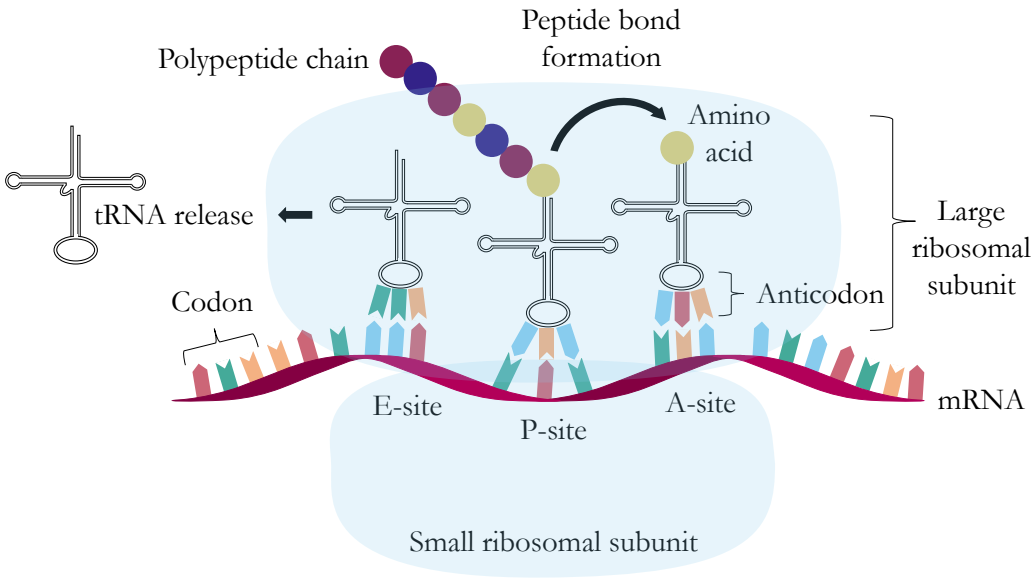

Fig. 1.5. Schematic of RNA translation. The small ribosomal subunit locates the AUG start codon and the large ribosomal subunit then docks to complete the translation complex. Translation is directed by three ribosome-binding sites for the tRNA including the P (peptidyl), A (aminoacyl), and E (exit) sites. The incoming aminoacyl tRNA binds to the A site and a peptide bond is formed with the peptidyl tRNA with the growing peptide chain (now in the P site). The ribosome then moves three nucleotides (one codon) along, a process known as translocation. The spent tRNA translocates from the P site to the E site where the binding of a new aminoacyl tRNA to the A site induces the release of the spent tRNA from the E site. This process continues until a stop codon (UAA, UAG or UGA) is read in the A site.

1.2. Regulation of gene expression in therapeutics

It was postulated more than half a century ago that the introduction of functional gene copies can modulate dysfunctional genes that manifest into diseases [14]. Thenceforth, ground-breaking research translating nucleic acids into therapeutic modalities has culminated into 21 approved drugs, including the mRNA-based vaccines for severe acute respiratory syndrome coronavirus 2 (SARS-CoV-2) that were awarded the 2023 Nobel Prize in Physiology and Medicine [15–17]. Their simplicity of design, aided by the rise of sequencing

technologies, and their ability to target 85% of the genome that is deemed "undruggable" using small molecules has accelerated research efforts [18,19]. As such, nucleic acids have garnered much attention in the field of drug discovery, offering a diverse toolkit for precisely controlling gene expression and in-turn inhibiting the translation of mutant proteins and regulating disease-causing genes [20].

1.2.1. Antisense oligonucleotides

Nucleic acid-based therapies extend beyond mRNA-payloads and the encoding of antigens to include siRNA and antisense oligonucleotides (ASOs) [18]. The most prevalent clinically-approved nucleic acid-based therapeutics are ASOs comprising short, single-stranded sequences (6-9 kDa) [21]. ASOs can be divided into three main modes of action: ribonuclease (RNase) H-mediated degradation, translation blocking, and splicing modulation (Fig. 1.6A) [16]. ASOs that are RNase H competent bind to sequence-specific mRNA through Watson-Crick-Franklin base pairing. The endogenous RNase H enzyme recognises the DNA–RNA heteroduplex as a substrate and catalyses the degradation of RNA, thereby silencing target gene expression [15].

Controlling gene expression can be achieved further by blocking translation or by modulating splicing. To block translation, ASOs are designed to bind to the translation initiation codon of the transcript, causing downregulation of a mutant protein through translational arrest [18]. In contrast, splicing is the act of processing the RNA before it is transcribed to mature mRNA by removing or "splicing-out" specific sequences (denoted introns) and then connecting together the remaining sequences (denoted exons). To modulate splicing, ASOs are designed to bind to intron-exon junctions on the target RNA transcript to interfere with RNA-RNA and/or RNA-protein interactions [15]. Interfering with splicing machinery is beneficial for the treatment of disorders with a known splicing defect.

ASOs can interact with intron-exon junctions to destabilise splicing sites or displace/recruit splicing factors. This enables the selective exclusion or retention of exons (denoted exon skipping or exon inclusion respectively) by the spliceosome, restoring normal gene function by either re-establishing the normal reading frame (evaluated by dividing the nucleotides in the mRNA sequence into their respective codons) or excluding mutated segments of DNA [16]. ASO-mediated splice correction can promote isoform switching, thereby restoring the expression of functional protein isoforms and/or diminishing the expression of harmful ones [15]. Nusinersen (commercially known as Spinraza) is an example of a splice-modulating ASO that has received regulatory approval to treat an autosomal recessive disorder caused by mutations in the survival motor neuron 1 (SMN1) gene. Such mutations result in SMN protein deficiency and further motor neuron deficiency. In this disorder, pre-mRNA encodes a paralogue SMN2 gene that lacks exon 7, thereby producing truncated and a non-functional SMN protein. Nusinersen modulates the splicing of SMN2 pre-mRNA in order to promote the translation of the full-length SMN protein via the inclusion of exon 7 [15].

1.2.2. Small-interfering RNA

siRNA comprises short, double stranded RNA sequences with a characteristic 19 base pair duplex and a terminal 2-nucleotide 3′ overhangs (13 kDa) [15,18]. siRNA takes advantage of the natural RNA interference (RNAi) mechanism and recruits the RNA-induced silencing complex (RISC), localised in the cytoplasm, to degrade target mRNA. siRNA comprises a guide strand (also denoted the antisense strand) and a passenger strand (also denoted the sense strand) (Fig. 1.6B). The passenger strand guides the siRNA to the catalytic RISC protein Argonaute 2 (AGO2) and as such must contain a stable charged phosphate analogue that can bind to the phosphate-binding pocket of AGO2 [18,19]. AGO2 catalyses the cleavage of the target transcript that is bound and complementary to positions 10 and 11 of the guide

RNA strand [15] (also known as splicer activity). This cleavage downregulates the target transcript and induces gene silencing. Givosiran (commercially known as Givlaari) is an example of a siRNA that has received regulatory approval to treat acute hepatic porphyria, a symptom of aminolevulinic acid synthase (ALAS1) overexpression. Givosiran leverages RNAi machinery to "knockdown" elevated levels of ALAS1-mRNA and in-turn supress porphyria attacks [15].

It should be emphasised that there are nucleic acid-based therapeutics that have alternative modes of action, including but not limited to the first gene-editing therapeutic, Casgevy, that is clinically approved to treat sickle cell disease, leveraging the CRISPR/Cas9 system [22].

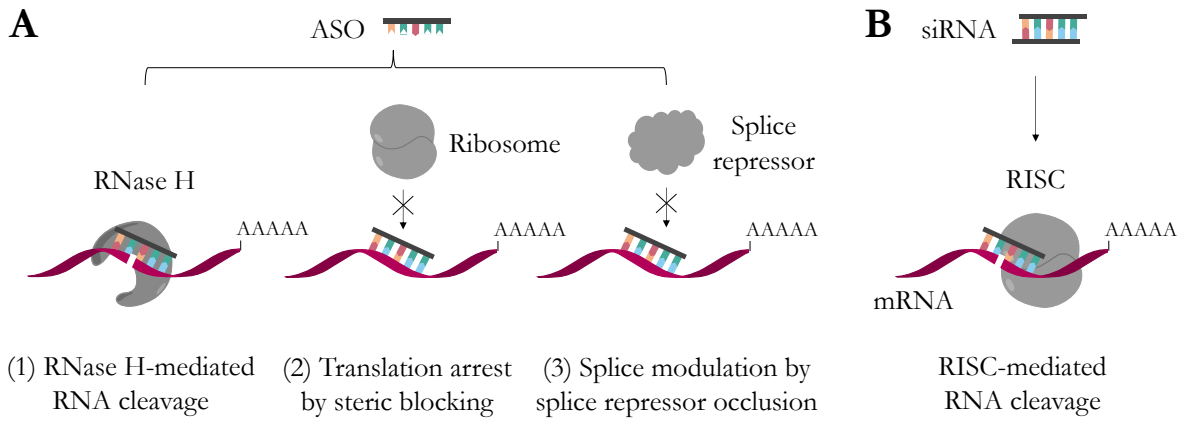

Fig. 1.6. Mechanisms of action for siRNA and ASOs. (A) ASOs bind to sequence-specific mRNA and either catalyse the cleavage of mRNA through the recruitment of the endogenous RNase H enzyme (1), downregulate mRNA expression through steric blocking and translational arrest (2), or bind to the intron-exon junctions of pre-mRNA to destabilise splicing sites or displace/recruit splicing factors (3). **(B)** siRNA takes advantage of the RNAi mechanism and recruits the RISC to degrade mRNA.

1.2.3. Chemical modification

Despite the clinical potential of ASOs and siRNA, their susceptibility to nuclease degradation and their anionic charge inhibiting cell internalisation remains a translational challenge [15]. Chemical modification represents an effective strategy to enhance the

pharmacokinetics, pharmacodynamics and biodistribution of nucleic acid-based therapeutics. Commonly explored chemical modifications can be divided into three main categories: backbone modification, ribose sugar modification and terminal modification.

First generation modifications focussed on the chemistry of the oligonucleotide backbone, with the most notable example being the incorporation of phosphorothioate linkages, which are formed by replacing one of the non-bridging oxygen atoms with a sulphur atom (Fig. 1.7). The atom replacement improves the charge distribution and results in increased overall lipophilicity that promotes binding to proteins in the plasma and within cells [19]. The interaction between oligonucleotides and plasma proteins (such as albumin) improves the pharmacokinetic profile by increasing the circulation time and reducing the renal clearance [15]. ASO designs readily incorporate phosphorothioate linkages without impeding RNase H activity. However this is at the expense of immunostimulatory effects and a lower transcript RNA binding affinity as compared with their unmodified counterparts [23]. There are further concerns with the introduction of a chiral centre at each modified phosphorous atom, whereby each chiral centre has differing physiochemical properties in terms of hydrophobicity, nuclease resistance, target affinity, and RNase H activity [15]. Synthesising phosphorothioate ASOs with a defined stereochemistry adds another layer of complexity, nevertheless, the challenge is being tackled by companies such as Wave Life Sciences [15]. Phosphorothioate linkages negatively impact the activity of siRNAs and so the linkages are reserved for the termini only. Nevertheless, the incorporation of phosphorothioate linkages imparts resistance to cellular nucleases and impacts long-lasting drug effects [15].

Alternatively, the oligonucleotide backbone can be replaced with a neutral phosphorodiamidate linkage and further the five-membered ribose heterocycle replaced with a six-membered morpholino ring [15]. These phosphorodiamidate morpholino oligomers

(PMOs) have a promising safety profile and have resulted in four clinically approved PMO-based drugs including Eteplirsen, Golodirsen, Casimersen, and Viltolarsen, all steric blocking ASOs targeting Duchenne Muscular Dystrophy [24]. Similarly to phosphorothioate linkages, PMOs contain chiral centres, whereby their effect has not been fully explored [15]. In addition, PMOs suffer from rapid excretion in-vivo and are incompatible with commercial transfection agents, unable to form the necessary complex [24].

Peptide nucleic acids (PNAs) are also an example of an uncharged oligonucleotide that has gained traction, comprising a neutral pseudopeptide backbone of repeating *N*-(2-aminoethyl)glycine linkages. PNAs retain a strong binding affinity to transcript RNA and have the added advantage of nuclease resistance. However, mirroring PMOs, PNA-RNA hybrids are not substrates for RNase H and so PNAs act by steric blocking mechanisms, and interact minimally with serum proteins, resulting in rapid excretion in-vivo [25].

Second generation modifications involve alterations to the 2′-position of the ribose sugar, most commonly via the introduction of 2′-*O*-methyl (2′-OMe), 2′-*O*-methoxyethyl (2′-MOE) or 2′-Fluoro (2′-F) groups (Fig. 1.7). These modified ASOs typically conform to a "gapmer" design, and are characterised by a central region of unmodified DNA nucleotides flanked by 2′-modified nucleotides (RNA-like bases). These 2′-ribose modifications (with the exception of 2′-F) and the consequential replacement of the 2′-hydroxyl group were found to improve nuclease resistance and prolong the therapeutic half-life. All ribose sugar modifications influence the molecular conformation and enhance the binding affinity for transcript RNA by promoting a 3′-*endo* pucker conformation of the ribose, thereby increasing the melting temperature of the heteroduplex by ~2 °C [15,26]. It is worth noting that 2′-ribose modifications prevent RNase H recruitment and are therefore reserved for ASOs

that act by steric blocking, and for the flanking sequences in the gapmer design [23]. The requirement for siRNA binding to AGO2 proteins results in more complex design requirements. Even so, 2′-modified nucleotides (RNA-like bases) are used on the 3′-terminus of some siRNA constructs and 2′-OMe and 2′-F modifications have further been reported with care taken not to ablate RISC loading and silencing activity [15]. Alnylam Pharmaceuticals have exploited an alternating pattern of 2′-OMe and 2′-F modifications to increase siRNA potency by more than 500-fold relative to unmodified siRNA in some instances [15]. Terminal modifications are focussed towards siRNA, which requires the guide strand to be phosphorylated at the 5′ terminus for AGO2 binding. Typically a phosphate mimic that is not recognised as a substrate for cellular phosphatases is used, such as 5′-(E)-vinylphosphonate [15].

The 2′-position of the ribose sugar can be modified with a methylene bridge, constraining the conformation of the 2′-oxygen and the 4′-carbon atoms. This modification, termed a locked nucleic acid (LNA), increases the binding affinity with transcript RNA at the expense of preventing RNase H recognition, thereby unless used in a gapmer design, LNAs rely on steric blocking [27].

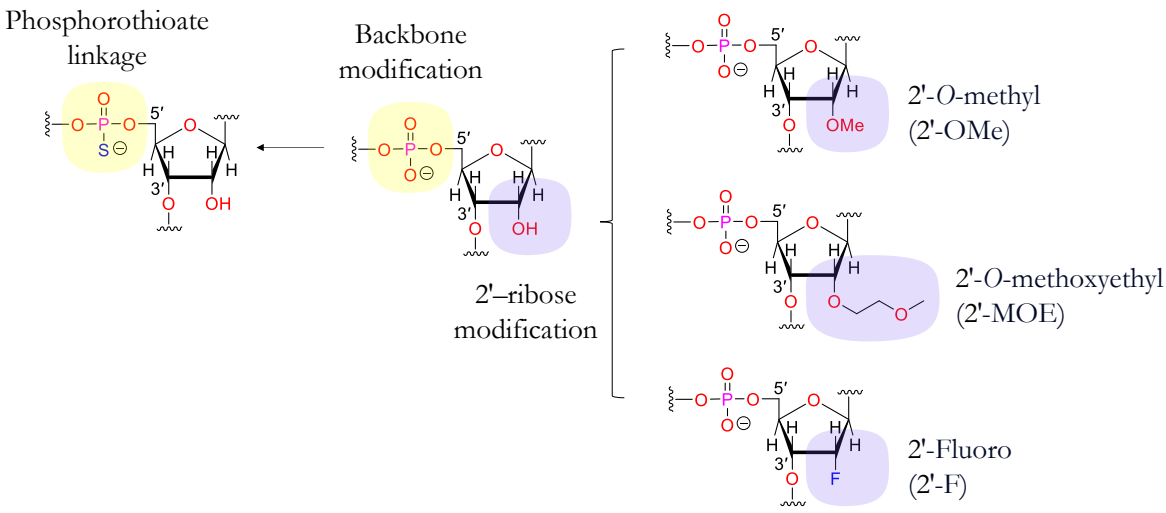

Fig. 1.7. Common chemical modifications of nucleic acid-based therapeutics. Schematic of first-generation modifications, notably the incorporation of phosphorothioate linkages and the replacement one of the non-bridging oxygen atoms with a sulphur atom, and second-generation modifications, primarily to the 2′-position of the ribose sugar and most commonly the addition of 2′-OMe, 2′-MOE, and 2′-F groups.

1.2.4. Delivery strategies

1.2.4.1. Gymnosis

The cellular stability afforded by second generation (ribose sugar) modifications have proven sufficient for the delivery of ASOs to a wide variety of tissues without the need for additional delivery agents (referred to as gymnosis) [28]. Gymnosis describes the cytosolic and/or nuclear uptake of nucleic acids without facilitation by chemical or physical means of drug delivery [29]. The notion of gymnosis was generalised by Stein *et al.* and since then the method has garnered widespread application [30]. This is due to a multitude of advantages including: lower inherent toxicity by virtue of no cationic or amphiphilic transfection agents; the ability to deliver to cell lines that are known to be difficult to transfect; close correlation of the resulting gene silencing patterns between in-vitro and in-vivo experiments; and the overarching convenience of the approach [30,31]. Despite this, gymnosis remains highly inefficient, requiring significantly higher concentrations of ASOs (0.1–10 μM) compared

with delivery agents (1–10 nM), and suffering from liver accumulation [28,29]. The unfavourable biodistribution remains a major translational challenge with concerns raised about adverse side effects from unwanted accumulation [23,28,32].

1.2.4.2. Chemical conjugation

An alternative delivery approach is to directly conjugate biomolecules that target specific cell-surface receptors. For instance, siRNA does not efficiently undergo endocytosis by gymnotic delivery and requires modification with targeting ligands [28]. The most prevalent targeting ligand comprises a trimer of *N*-acetylgalactosamine (GalNAc). GalNAc is a sugar derivative and avidly binds to the asialoglycoprotein receptor (ASGPR) that is highly expressed on hepatocytes (Fig. 1.8A) [33]. These advances have culminated in the United States Food and Drug Administration (FDA)-approved drugs Givosiran and Lumasiran and the European Medicines Agency (EMA)-approved drug Inclisarin, all of which are GalNAc-siRNA conjugates, and further the FDA-approved drug Wainua, a GalNAc-ASO conjugate [18]. Lipids (such as cholesterol) are also conjugated to nucleic acids [29]. A reoccurring drawback to chemical modification is unfavourable biodistribution. In fact, state-of-the-art cholesterol conjugates (based on DNA/RNA heteroduplexes), aiming to target the central nervous system (CNS), resulted in a significantly higher ASO biodistribution (by >100-fold) to the peripheral tissues than to the brain, raising concerns of adverse side effects.[34]

1.2.4.3. Lipid nanoparticles

The expansion of lipid-based delivery to include lipid nanoparticles (LNPs) has culminated in the FDA-approved drug Patisiran, an siRNA developed to treat polyneuropathy [18]. Lipid nanoparticles typically comprise phospholipids and cholesterol, cationic or ionisable lipids, and poly(ethylene glycol) (PEG)-modified lipids (Fig. 1.8B) [35]. Cationic lipids have a head

group with a permanent charge, such as the quaternary ammonium lipid 1,2-di-*O*-octadecenyl-3-trimethylammonium-propane (DOTMA), which has been shown to improve fusion with cellular membranes. Ionisable lipids, such as 1,2-dilinoleyloxy-*N*,*N*-dimethyl-3-aminopropane (DLin-DMA), are pH sensitive and become protonated at low pH. The permanent or induced positive charge allows for complexation with the anionic backbone of DNA/RNA and serves as the driving force for stable LNP formation [18]. Ionisable lipids are of particular interest as they give rise to a neutral charge at physiological pH that in-turn reduces interaction with blood cells and improves biocompatibility. The biocompatibility of lipids can be improved further by introducing biodegradable motifs such as ester groups [36]. The proton buffering capacity of ionisable lipids also facilitates endosomal escape by destabilising and rupturing the endosomal membrane through osmotic swelling (known as the "proton sponge effect") [37].

A commonly-used phospholipid is 1,2-distearoyl-*sn*-glycero-3-phosphocholine (DSPC), a component of the mRNA-based vaccines for SARS-CoV-2. The geometry and melting temperature (~54 °C) of DSPC stabilises the LNP structure [36]. Cholesterol can impart further stability by modulating the membrane integrity and rigidity, and separately contribute to improve biodistribution with derivatives such as cholesteryl oleate showing higher selectivity for liver endothelial cells than for hepatocytes [36,38]. PEG-modified lipids can be used to impart "stealth" properties, shielding the LNP from aggregation, opsonisation, and phagocytosis [39]. PEGylation also enhances the particle stability by decreasing aggregation. The continued expansion of LNP technologies are hindered by safety concerns resulting from their lipid components, such as reactogenicity, toxicity, efficacy loss and allergic reactions [40]. LNP technologies suffer from unreliable drug loading; benchmarked LNP formulations have been shown to contain 40-80% empty vesicles (no mRNA encapsulated), impacting payload distribution and dosage uniformity [41].

1.2.4.4. Spherical nucleic acids

Spherical nucleic acids (SNAs) represent an alternative nanoparticle-based delivery strategy. SNAs comprise nucleic acids (ASOs or siRNA) that are densely packed and radially arranged around a nanoparticle core, which are generally, though not always, formed of gold, silica, or iron oxide (Fig. 1.8C) [42]. The resulting steric hinderance protects from nucleolytic degradation, as does the high local salt concentration that deactivates enzymes in close proximity, culminating in a rate of degradation four times slower than that of the free duplexes [15,42]. SNAs self-deliver into more than 50 different cell types without the need for additional transfection agents, binding to scavenger receptors through the displacement of adsorbed serum proteins [43,44]. The dense coating of nucleic acids ($\sim 2 \times 10^{13}$ oligos cm^{-2}) impacts cellular uptake and there is a positive correlation between the degree of endocytosis and the density of attached nucleic acid strands [43,45]. SNAs are nontoxic, eliciting a minimum innate immune response, and are stable as a result of the DNA phosphate backbone that confers a highly negative zeta (ζ)-potential [42,44].

The discovery that SNAs can traverse the blood-brain barrier, allowing delivery to the CNS and the promotion of tumour apoptosis in glioblastoma-bearing mice, has brought SNAs to the forefront of nucleic acid delivery [15,16,44]. Unfortunately however, the majority of SNA particles are deposited in the liver and kidneys [15]. Their indiscriminate uptake poses challenges for targeting in-vivo, with future development focussing on the incorporation of targeting moieties such as the adsorption of human epithelial growth factor receptor 2 (HER2) monoclonal antibody for targeting HER2-positive breast cancer cells [42,46].

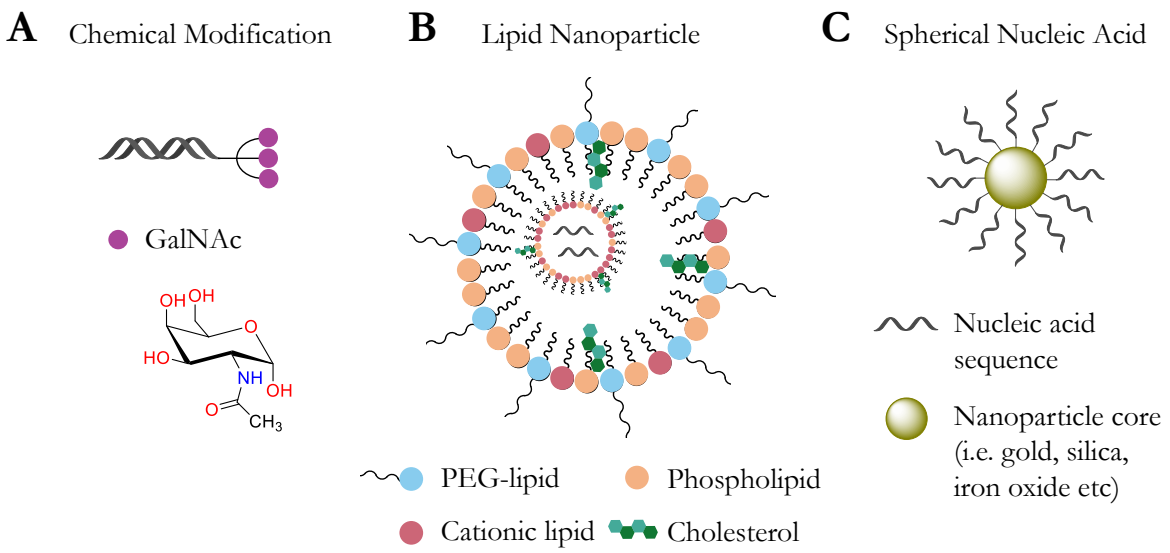

Fig. 1.8. Delivery strategies for nucleic acid-based therapeutics. (A) Direct chemical modification with small molecules such as GalNAc, which targets hepatocytes in the liver and underpins the Givosiran, Lumasiran and Inclisarin drugs (clinically-approved GalNAc-siRNA conjugates). **(B)** Encapsulation within lipid nanoparticles, clinically-approved to deliver the drug Patisiran (an siRNA therapeutic) and comprising phospholipids and cholesterol, cationic or ionisable lipids, and PEG-modified lipids. **(C)** Incorporation into SNAs comprising nucleic acids (ASOs or siRNA) densely packed and radially arranged around a nanoparticle core (such as gold, silica, and iron oxide amongst others).

1.3. Regulation of gene expression in synthetic cells

The complexity of reprogramming living cells has driven research into synthetic mimics, denoted synthetic cells; non-living compartments capable of imitating the behaviour, function, and structure of living cells[47,48]. Synthetic cells are typically constructed from the bottom-up, taking advantage of lipid vesicles and, notably, giant unilamellar vesicles (GUVs), which have comparable dimensions (diameters above 1 μm) and curvature with eukaryotic cells [49]. These systems are unconstrained by the complexity associated with engineering living cells (editing, deleting or replacing genes) and can accommodate non-biological components to attain new functionalities [50]. The flexible and modular design of synthetic cells significantly increases their technological value, opening up applications in drug delivery, biosensing and biomanufacturing amongst others [48,51]. The feasibility of

synthetic cells was first demonstrated by Chang *et al.* in 1957 and since then the ability to regulate gene expression as a design feature has become increasingly sophisticated. Typically, gene-expressing synthetic cells comprise a cell-free protein synthesis (CFPS) system bound by a lipid membrane, programmed according to DNA templates that are specific to the desired biological activity [52]. The encapsulated CFPS system enables gene regulation and expression capabilities, diversifying the tool kit available for synthetic cells.

1.3.1. Cell-free protein synthesis

CFPS harnesses the transcription and translation machinery of living cells to enable protein synthesis in-vitro [53]. Importantly, CFPS is a powerful tool for enabling high-throughput protein expression with applications in functional genomics and antibody production [54]. CFPS and crude extract-based systems originate from pioneering work by Nirenberg and Matthaei in 1961 [55], in which cell extracts were harvested by a three-step process comprising cell lysis, a runoff reaction, and dialysis. Cell lysis is implemented to remove the cell wall and insoluble substances, aiming to obtain only the biochemical components necessary for energy generation, transcription and translation; the runoff reaction decouples the ribosomal subunits from endogenous translation events; and dialysis provides a suitable storage buffer [56,57]. Cell extract-based CFPS benefits from low cost and high protein yield, however, the preparation is labour intensive and difficult to standardise [58,59].

With this in mind, CFPS based on *Escherichia coli* (*E. coli*) was devised soon thereafter, most notably the Protein synthesis Using Recombinant Elements (PURE) was developed by Shimizu *et al.* in 2001 [60]. The PURE system derives all components necessary for transcription and translation from *E. coli* [57]. The composition of the PURE system comprises 36 purified proteins (including T7 RNA polymerase and tRNA synthetases), translation factors, enzymes for energy regeneration (such as creatine kinase) and ribosomes. Other

components such as nucleotides, amino acids, tRNAs, energy substrates (such as creatine phosphate) and essential ions (such as magnesium and potassium) are required [57]. The PURE system can be tuned further by encouraging molecular crowding through the addition of PEG 8000 or Dextran, emulating the significantly higher density of biomolecules involved in protein synthesis in-vivo [58]. The advantages of the PURE system over cell extract-based CFPS is fourfold: improved safety, evading issues from live transgenic cells; increased tolerance and operation even in the presence of toxins; the ability for long-term storage through freeze-drying techniques; faster responses indicative of shorter reaction times, greater sensitivity and a wider detection range [57]. Such advantages are at the expense of a greater cost and lower protein yields [54].

PURE expresses proteins using the T7 RNA polymerase and promoter system (Fig. 1.9). The bacteriophage T7 RNA polymerase is composed of one subunit that transcribes DNA in the 5′ to 3′ direction with high selectivity towards its own promoter sequence [61]. T7 RNA polymerase binds to two distinct regions of the T7 promoter sequence, namely polymerase binding takes place between position –17 and position –5 or –6, and initiation of transcription takes place downstream of position –5 or –6 [62]. Transcription initiation is relatively insensitive to proportions of the coding strand being missing upstream of position –6, allowing for the design of shorter T7 promoter sequences [63].

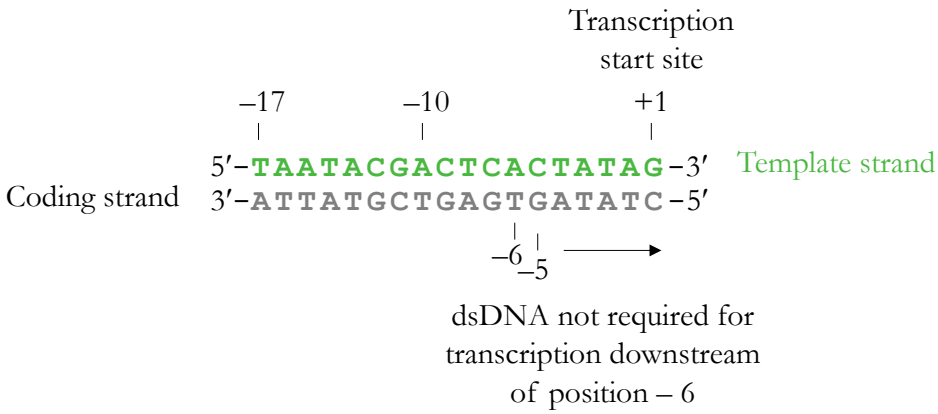

Fig. 1.9. T7 promoter sequence. The T7 promoter sequence consists of a coding strand and a template strand. T7 RNA polymerase binding takes place between position –17 and position –5 or –6 and initiation of transcription takes place downstream of position –5 or –6. dsDNA is not required for transcription downstream of position –6, allowing for the design of shorter T7 promoter sequences.

1.3.2. Bottom-up synthesis of synthetic cells

The formation of gene-expressing synthetic cells and the encapsulation of CFPS machinery (commonly the commercially-available PURExpress system) is typically achieved by the bottom-up synthesis of GUVs. In particular the inverted emulsion transfer method is an accessible preparation technique that allows for efficient encapsulation (Fig. 1.10) [49]. In the emulsion transfer method, an aqueous solution containing the CFPS machinery and sucrose forms the inner solution and is suspended within lipid-containing oil. The amphiphilic lipid molecules spontaneously self-assemble into a monolayer at the surface of the aqueous droplets, generating a water-in-oil (w/o) emulsion. In a parallel step the lipid-containing oil is suspended on the surface of an aqueous buffer containing glucose, generating another lipid monolayer at the w/o interface. The addition of sucrose in the inner solution establishes a mass gradient that is exploited to force the w/o emulsion droplets across the second lipid monolayer by centrifugation, forming a lipid bilayer and resulting in GUV formation [49,52]. This approach suffers from issues with reproducibility, which is highly dependent on

environmental conditions, and from heterogeneous expression across synthetic cell populations, which results from the stochasticity of solute partitioning during synthesis [64,65]. Nevertheless, the membrane composition can be fine-tuned with different ratios of lipids present in biological membranes, such as 1-palmitoyl-2-oleoyl-*sn*-glycero-3-phospholipid (POPC) or egg phosphatidyl choline (egg-PC) [65]. Membrane proteins can be incorporated by spontaneous insertion, fusion of the GUVs with protein containing liposomes or by CFPS and protein expression inside the GUVs [49].

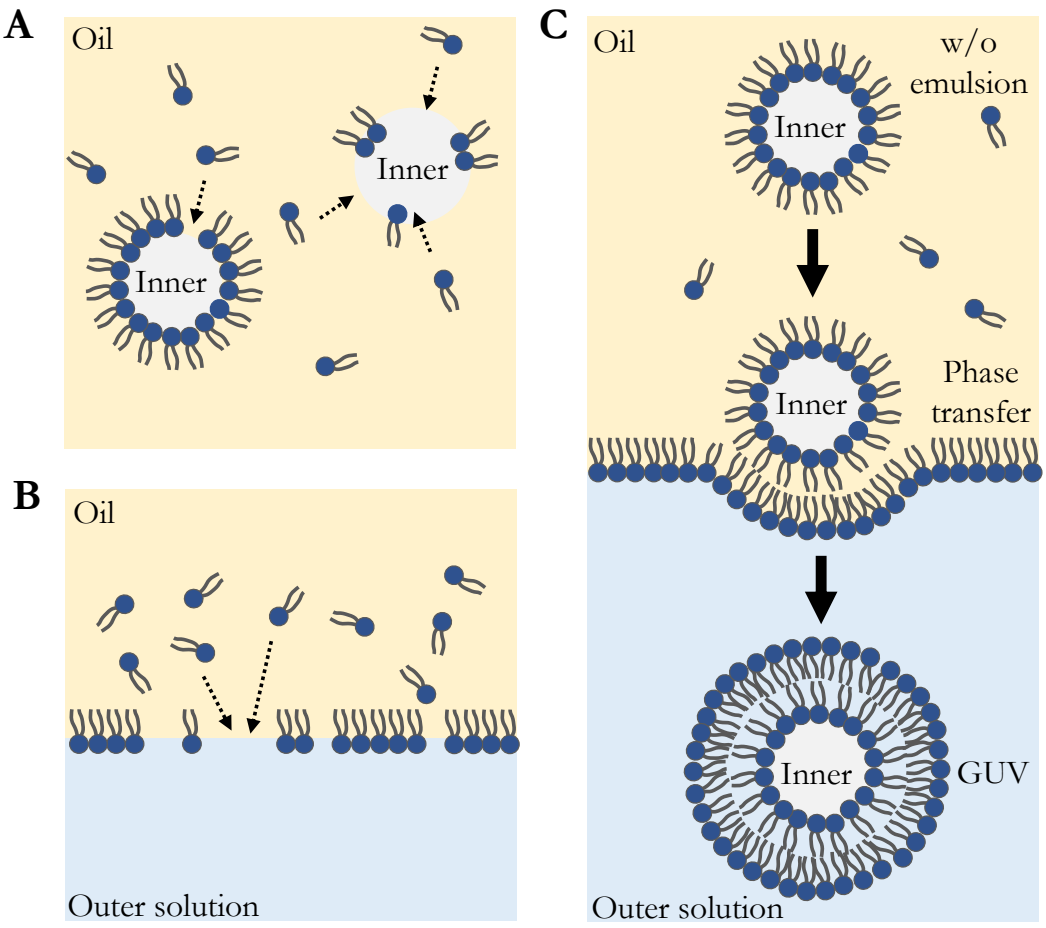

Fig. 1.10. Schematic detailing the inverted emulsion transfer method. (A) An aqueous solution containing the CFPS machinery and sucrose in suspended in lipid-containing oil, causing the self-assembly into a lipid monolayer and forming a w/o emulsion. **(B)** Lipid-containing oil is suspended on the surface of glucose-containing buffer, forming another lipid monolayer. **(C)** The w/o emulsion droplets are forced across the lipid monolayer by centrifugation to form a lipid bilayer and a resulting GUV. Figure reproduced from "Engineering cellular communication between light-activated synthetic cells and bacteria" by Smith et al.[52] (© 2022) under a creative commons license (CC-BY-NC-ND 4.0).

1.3.3. Applications of synthetic cells

The stability and intracellular fate of GUVs is critical to clinical translation and has attracted much research, being modulated by the membrane composition, charge and size amongst others [66–68]. The rapid elimination of GUVs in-vivo is due to opsonisation, subsequent recognition by macrophages and clearance by the reticuloendothelial system (RES) [69]. This has driven research into the stabilisation of liposomes with polymers [69]. In particular, PEG has been incorporated into the membrane of GUVs, proving successful at prolonging blood circulation with reported half-lives as high as 45 h in humans [70,71].

The promising half-life of synthetic cells in-vivo demonstrates their potential for applications in medicine. In addition, the sheer size of GUVs, with diameters above 1 μm, is advantageous for increasing the drug loading capacity of lipid-based carriers and impacting sustained release profiles over long periods of time [49]. This has resulted in the development of synthetic cells as drug delivery vehicles. Compelling examples include the excretion of an exotoxin from GUVs for the treatment of 4T1 breast cancer in tumour-bearing mice, which triggered the increased expression of an apoptotic marker (caspase 3) [72]; and the engineering of GUVs to release insulin after injection into type-1 diabetic mice, successfully mediating glucose levels for up to five days [73]. The added functionality of in-situ protein production and the controlled release of pharmaceutically active biomolecules holds promise for the delivery of unstable drugs, and also circumvents any side effects caused by drug leakage during storage and/or circulation that may arise from pre-loading vesicles [74]. This was realised by Chen *et al.* in 2022, producing recombinant human basic fibroblast growth factor inside GUVs for the promotion of angiogenesis and tissue regeneration, which in-turn proved non-immunogenic in mice and stable for a half-life of 6 h [75].

To realise synthetic cells as drug delivery vehicles, the cargo should be released on-demand and targeted to the therapeutic site of interest. In aid of this, two types of targeting strategies have been developed, active targeting and passive targeting. Active targeting requires the attachment of specific ligands, most notably antibodies and their fragments, peptides and aptamers [76]. In contrast, passive targeting is achieved by the adsorption of biomolecules in the bloodstream such as the serum apolipoprotein E (ApoE), which targets the low-density lipoprotein receptor (LDLR) expressed on hepatocytes [18]. Additional levels of control can be incorporated by inducing drug release and/or in-situ protein production specifically at the therapeutic site of interest. The ability to control protein expression in GUVs has been achieved with RNA-based regulators, known as riboswitches, which regulate gene expression in response to the binding of small molecules with the mRNA transcript. RNA riboswitches allow for transcriptional control by switching between truncated and full-length mRNA, and translational control by modulating mRNA conformation and the resulting accessibility of the ribosome binding site [77]. This mechanism of action has been applied to the upregulation of gene expression and the synthesis of proteins in GUVs and in response to small molecule activators (Fig. 1.11) [77–79]. In particular, cargos have been released from GUVs on-demand by the in-situ synthesis of the pore-forming protein alpha-hemolysin (α-HL) [77,78]. This approach relies on membrane-permeable small molecules (such as theophylline and arabinose) that are not well suited to therapeutic applications, taking into account the dynamic nature of disease sites where changes in local physiochemistry can impact off-target effects and/or failure of activation [50].

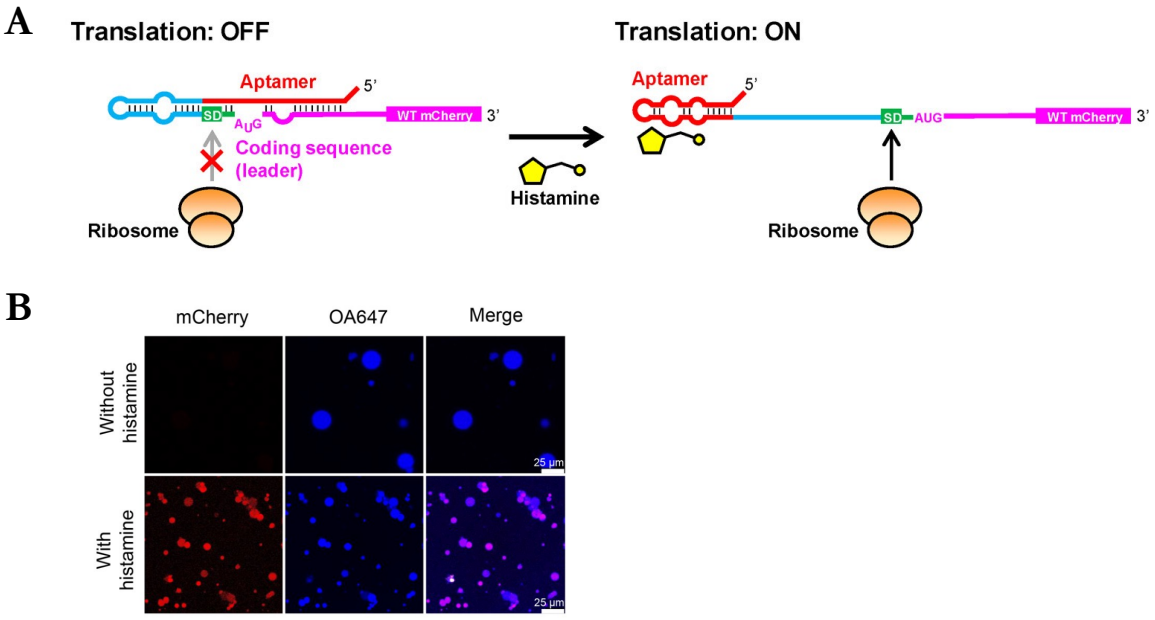

Fig. 1.11. Schematic detailing the regulation of gene expression in response the binding of small molecule activators to mRNA. (A) The small molecule, histamine, was used to disrupt the mRNA secondary structure to provide newfound accessibility to the ribosome binding site (SD denotes the Shine-Dalgarno sequence), thereby upregulating gene expression and increasing translation efficiency of the fluorescent protein, mCherry. **(B)** Confocal microscopy images demonstrating the in-situ CFPS of mCherry inside GUVs and only in the presence of histamine. Figure reproduced from "Programmable artificial cells using histamine-responsive synthetic riboswitch" by Dwidar *et al.*[79] (© 2019) under an open access ACS AuthorChoice License.

1.4. Regulation of gene expression by an external stimulus

The regulation of gene expression by an external stimulus is complementary to traditional targeting methods (active and passive targeting, as described in section 1.2.3.) and offers a promising alternative to enhancing the on-demand release of nucleic acids and their targeted delivery to the therapeutic site of interest. The majority of approved nucleic acid-based therapeutics naturally accumulate in, and thus target, the liver [32]. Alongside the research effort into active targeting beyond the liver, such as cholesterol-ASO conjugates, there is scope for innovative strategies that inhibit the function of nucleic acids [34]. This would allow for the therapeutic to remain dormant whilst in circulation, until the remote-activation by an

external stimulus at the therapeutic site of interest. This on-demand control holds promise as a complementary strategy to active targeting for improving the biodistribution of nucleic acids in-vivo.

1.4.1. Temperature

Temperature has been explored as an exogeneous trigger. RNA thermometers have been used extensively in CFPS systems to control gene expression by modulating conformational changes in the mRNA secondary structure, occluding the ribosome binding site at one temperature and liberating it at another [80]. In particular, changes in temperature regulate accessibility to the Shine-Dalgarno (SD) sequence, thereby facilitating ribosome binding and initiating translation [81]. Monck *et al.* used RNA thermometers to regulate the translation of α-HL inside GUVs and facilitate the selective release of a pre-encapsulated small molecule cargo at elevated temperatures (42 °C) [50]. The increase in temperature modulated the mRNA conformation and permitted access to the ribosome binding site, controlling protein expression in GUVs, albeit with leakiness in expression leading to a poor on/off-state (Fig. 1.12) [50].

Beyond GUVs, polymers with a lower critical solution temperature (LCST), such as poly*(N*-isopropylacrylamide), have been incorporated onto the surface of SNAs alongside functional DNA strands [82,83]. At temperatures below the LCST, hydrophilic interactions with the surrounding water molecules cause the polymer to swell and shield the DNA. Conversely, at temperatures above the LCST, the hydrogen bonds with water are disrupted and the polymer contracts, exposing the DNA for selective binding [82]. This mechanism has been used to selectively cleave DNA by DNAzyme activation [83].

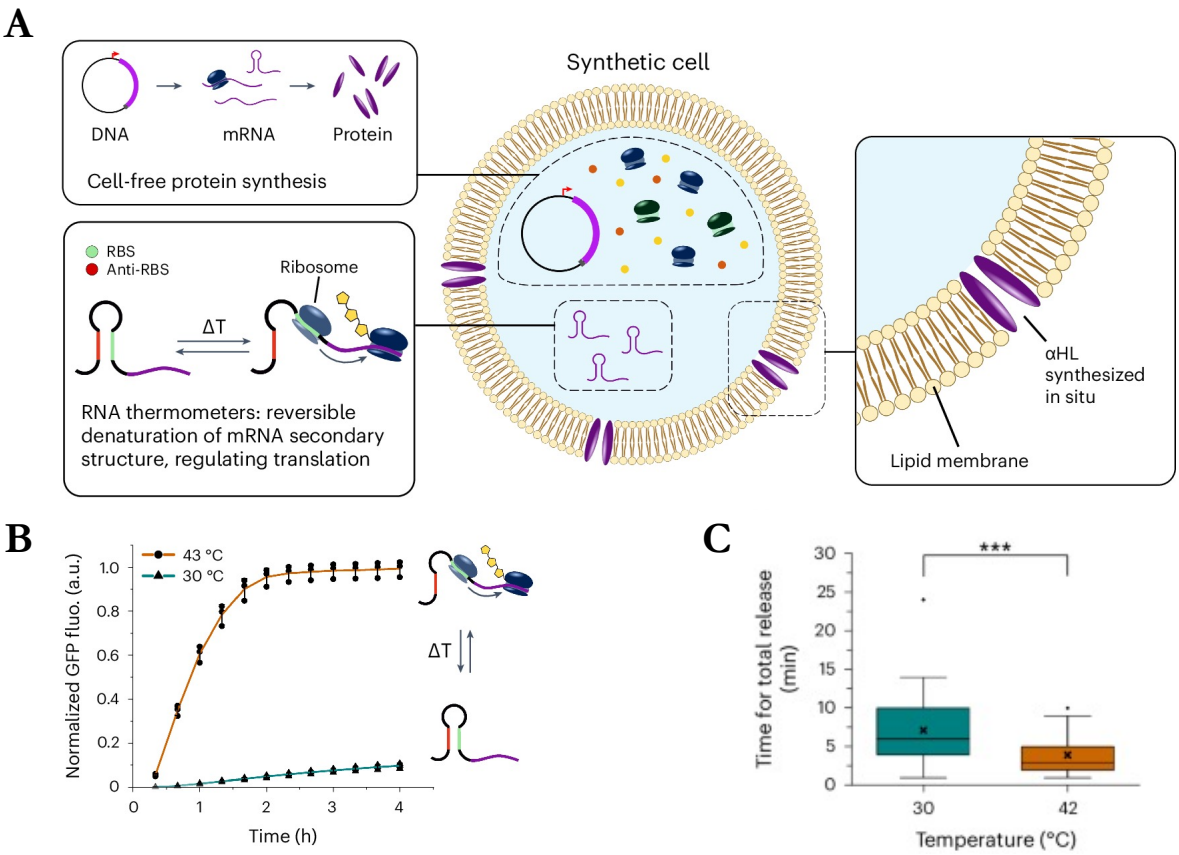

Fig. 1.12. Schematic detailing the temperature-mediated expression of a pore-forming protein for the selective release of small molecules from synthetic cells. (A) RNA thermometers were exploited to control CFPS inside synthetic cells in response to elevated temperature by permitting access to the ribosome binding site on transcript mRNA. **(B)** Testing of thermometer RNAT3-1 from Jia *et al.*[84]. The free energy to break the hairpin was insufficient at temperatures below 30 °C, preventing ribosomal binding and inhibiting CFPS and the expression of the green fluorescent protein, dasherGFP (dGFP). In contrast, increasing the temperature to 43 °C allowed for the denaturation of the hairpin, enabling ribosomal binding and further the expression of dGFP. **(C)** Time taken for the GUVs, encapsulating the CFPS machinery and the RNA thermometer platform, to synthesise the pore-forming protein α-HL and facilitate the release of cargo at varying temperatures (unpaired two-tailed *t*-test $P = 2.38 \times 10^{-7}$). Figure reproduced from "Genetically programmed synthetic cells for thermo-responsive protein synthesis and cargo release" by Monck *et al.*[50] (© 2024) under a creative commons license (CC-BY-NC-ND 4.0).

1.4.2. Photoactivation

Light (both in and beyond the visible spectrum) has been widely explored as an attractive external stimulus for regulating gene expression, as it offers tight spatiotemporal control and does not interfere with most cellular signalling pathways, acting orthogonally [85]. To this end,

a robust platform was developed by Booth *et al.* through the incorporation of light-sensitive groups into the T7 promoter sequence of linear DNA templates [86]. In this design, seven thymine bases were replaced with amino-C6-thymine bases in the standard T7 promoter sequence. *N*-hydroxysuccinimide (NHS) ester coupling was exploited to install 2-nitrobenzyl photocleavable biotinylated linkers into the T7 promoter region, which protruded from the major groove of the resulting dsDNA. The subsequent binding of monovalent streptavidin to each biotin group created a steric blockage that impeded T7 RNA polymerase from binding, thereby blocking transcription. Exposure to ultraviolet (UV) light at a wavelength of 365 nm (in the UVA regime) efficiently cleaved the 2-nitrobenzyl group and restored transcription of the DNA template [86]. The tight control of in-situ gene expression was exploited to activate the expression of α-HL, which in-turn inserted itself into the interface bilayer and enabled small molecule transfer between synthetic cells in a three-dimensional (3D) printed synthetic tissue [86]. This platform was expanded to catalyse the in-situ synthesis of the membrane permeable signalling molecule, acyl homoserine lactone (AHSL) derivative, inside GUVs and on-demand in the presence of UVA light (Fig. 1.13) [52]. AHSLs are used in bacterial quorum sensing, a key communication pathway for bacteria and their development as biofilms [87]. Smith *et al.* controlled quorum-sensing-based communication between synthetic cells and bacteria by regulating the in-situ synthesis of an AHSL synthase (*BjaI* AHSL) on-demand and only in the presence of UVA light at a wavelength of 365 nm. *BjaI* AHSL converted the membrane impermeable substrates, isovaleryl coenzyme A (IV-CoA) and S-adenosylmethionine (SAM), into the membrane permeable signalling molecule *N*-isovaleryl-L-homoserine lactone (IV-HSL), which diffused across the lipid bilayer and activated green fluorescent protein (GFP) expression in bacterial receiver cells [52]. This lays the foundations for the in-situ production of small molecules from synthetic cells and their application as targeted drug delivery vehicles.

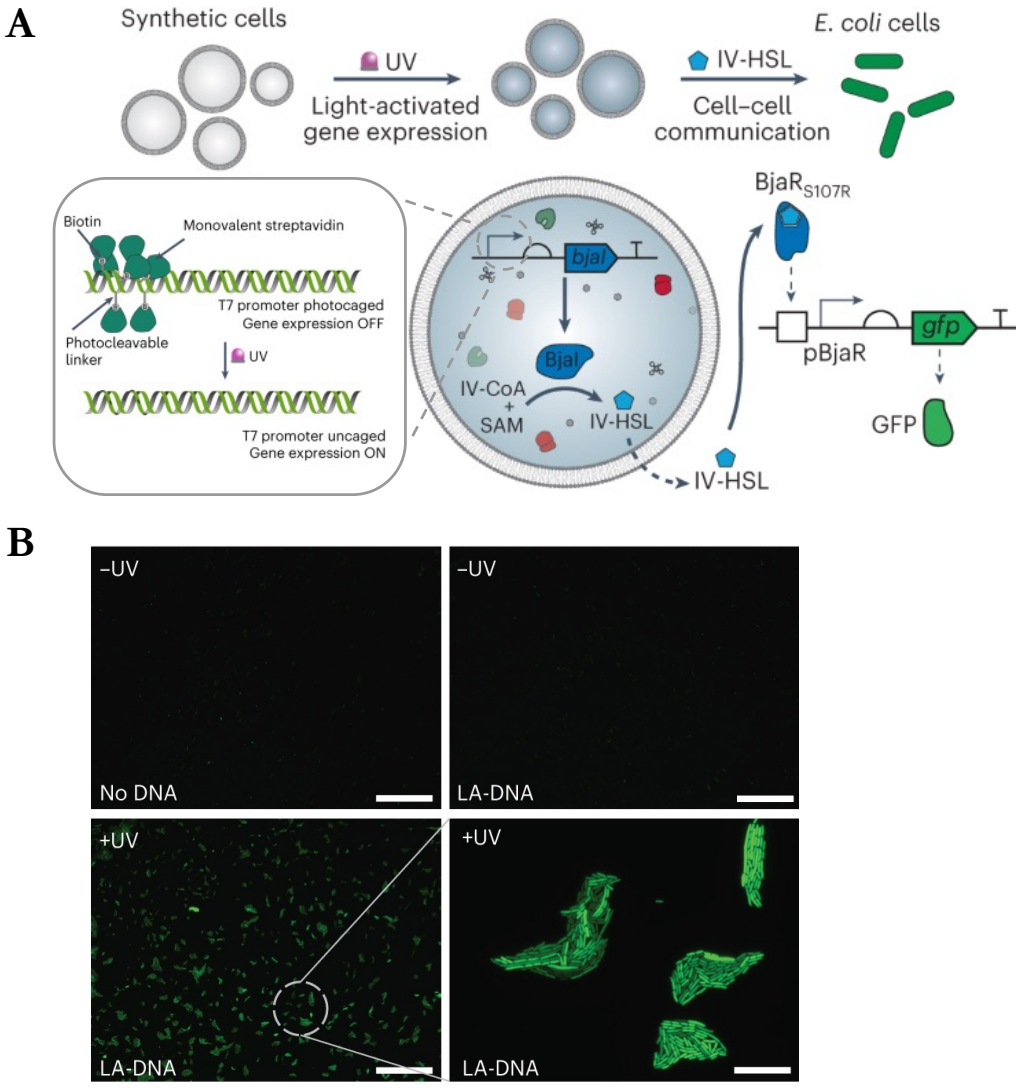

Fig. 1.13. Schematic detailing the light-mediated communication between synthetic cells and living cells. (A) PURExpress (CFPS system) and light-activatable DNA templates encoding the protein of interest, *BjaI* AHSL, were encapsulated inside GUVs. In the absence of light, transcription was impeded by photocleavable blocking groups that prevented T7 RNA polymerase from binding. In the presence of UV light, the blocking groups were cleaved and the ability of the T7 RNA polymerase to bind and initiate transcription was restored, allowing *BjaI* AHSL to be translated. *BjaI* AHSL subsequently converted the substrates, IV-CoA and SAM, into the membrane permeable signalling molecule IV-HSL. IV-HSL diffused across the lipid bilayer and activated GFP expression in bacterial receiver cells, modulating cell to cell communication. **(B)** Confocal microscopy images of bacterial receiver cells embedded in agarose alongside light-activatable GUVs. GFP expression was activated under UV light irradiation by probing the on-demand synthesis of *BjaI* AHSL and subsequently IV-HSL. GFP fluorescence was not observed in absence of UV light or in agarose containing GUVs without DNA templates encoding *BjaI* AHSL. Scale bar = 200 μm. Scalebar (bottom right, zoomed in) = 20 μm. Images are representative of n = 2 independent experiments. Figure adapted from "Engineering cellular communication between light-activated synthetic cells and bacteria" by Smith *et al.*[52] (© 2022) under a creative commons license (CC-BY-NC-ND 4.0).

In a similar vein light has been used to control the function of ASOs [88–90]. In this case, ASOs were modified with terminal amine groups, which in-turn were coupled to photocleavable biotinylated linkers and caged with streptavidin proteins [88,90]. The ASO activity was silenced through topological constraint and/or steric blocking, which was recovered upon UVA (wavelength of 365 nm) [88,89] or blue light (wavelength of 455 nm) [88] irradiation. In a novel development, Mazzotti *et al.* targeted two different mRNA transcripts by incorporating orthogonal photocages into two different ASO sequences that were then activated with two different wavelengths of light (nitrobenzyl with UVA at 365 nm wavelength and coumarin with blue light at 455 nm) [90]. A photocleavable 2-nitroveratryl bromide was used to modify phosphorothioate linkages chemoselectively in the backbone of ASOs [89]. The recovery of RNase H activity was only achieved after UVA irradiation, restoring the hybridisation ability of the modified-ASO by removing the photocage. This was at the expense of a strong reduction in aqueous solubility when the ASO was modified [89]. The majority of the research in this area focuses on using UV (specifically UVA, which is the most benign of the three UV classifications) and blue light, though it still poses cytotoxicity risks and has limited ability to penetrate bodily tissue (by <1 mm), hindering its use in therapeutic applications [91,92].

Near-infrared (NIR) light is more suitable for penetrating bodily tissue (up to 5 mm for NIR ≅ 750 nm) than UVA and blue light [92,93]. To exploit this, stimuli-responsive "Y-motif" DNA secondary structures and LCST polymers have been incorporated onto Au nanorods for the codelivery of siRNA and doxorubicin [94]. The heat is dissipated into the surrounding solution when Au nanorods are irradiated with NIR light. This causes the LCST polymers to shrink and expose the DNA "Y-motifs", which then dissociate in the presence of endogenous micro-RNAs and the intracellular fuel ATP, thereby releasing the

siRNA/doxorubicin and inducing cell apoptosis [94]. Despite the promise of Au nanorods, NIR light suffers from limited tissue penetration [92].

1.4.3. Magnetism

An ideal external stimulus for controlling gene expression is alternating magnetic fields (AMFs), which are deeply tissue-penetrating (>10 cm) and biologically benign [95,96]. Superparamagnetic nanoparticles dissipate thermal energy to the surrounding medium as a result of Brownian and Néel fluctuations in the presence of an AMF [97]. Brownian relaxation is described as the physical rotation of the particle, whereas Néel relaxation is described as the rotation of the magnetic moment within the particle. If the applied AMF is strong enough to rotate the particle itself or to displace the magnetic moment from the preferred orientation, then relaxation back to equilibrium releases thermal energy to the surrounding fluid, by way of shear stress (Brownian) or the rearrangement of atomic dipole moments (Néel) [98]. This localised heating, termed magnetic hyperthermia, is clinically-proven (and approved) to ablate malignant tumours by exploiting the differing heat tolerance between tumour and healthy cells, whereby healthy cells can survive above physiological temperature for longer [99]. Hyperthermia can be divided into two classifications: ablation and mild hyperthermia. Ablation is defined by short (10 min) bursts at temperatures above 50 °C, which aim to denature proteins and achieve apoptosis. In contrast, mild hyperthermia is defined by longer bursts (up to 1 h) at temperatures between 39 °C and 42 °C, which aim to increase perfusion, improve blood flow and activate an immune response [100]. Magnetic hyperthermia was commercialised by MagForce and its system operates at a frequency of 100 kHz, optimised to minimise eddy currents within the body and reduce patient discomfort [101,102].

It is worth noting that ultrasound has also been exploited to induce hyperthermia amongst other phenomenon such as cavitation and formation of gas bubbles to permeabilise liposomes containing DNA payloads [103]. Ultrasound benefits from being a non-invasive technique that can be guided by real-time imaging and enables precise spatial targeting; however, it is known to cause DNA fragmentation, which reduces the transfection efficiency, and the ability of ultrasonic waves to attenuate tissue is inversely proportional to their frequency [104].

Iron oxide nanoparticles (IONPs) (typically magnetite and/or maghemite) have been extensively researched due to their inherent biocompatibility, forming the basis of clinically-approved and globally-marketed medicines as iron supplements and contrast agents for magnetic resonance imaging (MRI) [105,106]. Superparamagnetic IONPs (<100 nm) are of particular interest for biomedical applications as they do not exhibit coercivity or remanent magnetisation, thereby avoiding issues arising from magnetic aggregation in blood vessels and imparting a high magnetic susceptibility [107]. These properties have diversified the applications of IONPs to include heating mediators for magnetic hyperthermia, which have been successfully deployed in-vivo [102].

There is a significant local-to-global temperature difference upon exposure to an AMF at distances shorter than 3 nm from the surface of the IONPs [109]. This gradient has been mapped by attaching dsDNA with varying lengths (such as 10 to 12 base pairs) and therefore varying melting temperatures (T_m). The temperature at the surface of the IONPs is then determined by correlating the specific length of ssDNA released, through the unwinding and denaturing of the dsDNA at various magnetic field strengths (*H*) and frequencies (*f*), to the known T_m of that specific dsDNA [110,111]. This mechanism has previously been used to

release DNA in-vivo, but required a high frequency of 400 kHz that is not compatible with the only clinically-available magnetic hyperthermia system by MagForce [95,102].

Magnetic hyperthermia has been investigated for rupturing lipid bilayers, releasing therapeutic small molecules from liposomes [102,112–114]. Lipids that have an amenable phase transition temperature, such as 1,2-Dimyristoyl-*sn*-glycero-3-phosphocholine (DMPC) lipids, have been incorporated into the lipid bilayer of GUVs to facilitate grain boundary defects in response to an increase in temperature and transport small molecule cargo [113,114]. Zhu *et al.* exploited this to tether streptavidin-coated IONPs to the surface of liposomes (200 nm in diameter) through the incorporation of biotinylated DMPC lipids (Fig. 1.14). These liposomes encapsulated the non-fluorescent fluorescein di-β-d-galactopyranoside (FDG) small molecule, and were themselves embedded in larger GUVs alongside the enzyme β-galactosidase (β-Gal). The application of an AMF with a field strength up to 40 mT and a frequency of 400 kHz resulted in magnetic hyperthermia that was exploited to form grain boundary defects in the DMPC lipid bilayer, thereby releasing the encapsulated FDG into the larger GUV. The β-Gal enzyme catalysed the hydrolysis of FDG and facilitated the production of fluorescein [114].

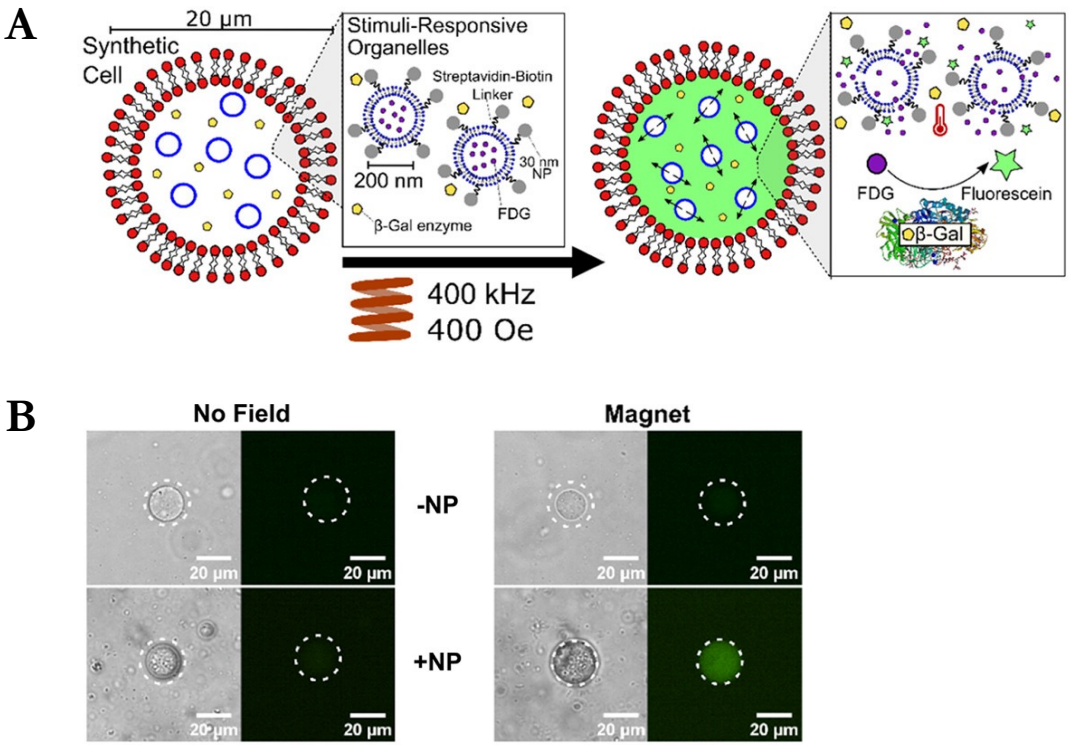

Fig. 1.14. Schematic detailing the control of synthetic cells with magnetic hyperthermia, rupturing the lipid bilayer and selectively releasing cargo. (A) Thermally-responsive liposomes (200 nm) encapsulating the non-fluorescent FDG were embedded in large GUVs that themselves contained the enzyme β-Gal and decorated with IONPs. The heat dissipated from the IONPs in an AMF was exploited to form grain boundary defects and rupture the lipid bilayer of the liposomes (200 nm), thereby releasing FDG into the large GUV. The β-Gal enzyme catalysed the hydrolysis of FDG, synthesising fluorescein in the large GUV. **(B)** Confocal microscopy images showing the production of fluorescein and increase in fluorescence in an AMF with and without IONPs embedded in the membrane. Figure adapted from "Magnetic modulation of biochemical synthesis in synthetic cells" by Zhu *et al.*[114] (© 2024) under a creative commons license (CC-BY 4.0).

The extent of localised heating from magnetic hyperthermia depends on the size of the exposed tissue, alongside the magnetic field strength-frequency product ($H \times f$) known as the Atkinson-Brezovich limit [115]. The clinical tests used by Atkinson-Brezovich to establish a safety limit ($H \times f = 4.85 \times 10^8$ A/m·s) were dependent upon a coil of diameter ~300 mm being placed around the torso of a patient[116,117]. It has since been found that a higher $H \times f$ safety limit is permissible if the exposed region of the body is smaller in diameter (~100 mm) [118]. A new upper safety limit was proposed by Hergt *et al.*

($H \times f = 5 \times 10^9$ A/m·s) [118] and supported by Herrero de la Parte *et al.* in more recent tolerance tests, which determined that exceeding the Atkinson-Brezovich limit up to 9.59×10^9 A/m·s is safe [116]. The $H \times f$ criterion for the system presented by Zhu *et al.* is 1.27×10^{10} A/m·s with $H = 40$ mT or 31.8 kA/m and $f = 400$ kHz, which exceeds the upper safety limit proposed by both Hergt *et al.* and Herrero de la Parte *et al.* [116,118]. In light of this, there is a need to develop drug delivery systems that operate within clinically-relevant magnetic field strengths and frequencies, being safe and compatible with the only clinically-approved magnetic hyperthermia system by MagForce (~100 kHz) in order to aid medical translation.

In addition, the presented programmable delivery vehicles do not have the added functionality of regulating gene expression itself. The ability to control the downstream function of the nucleic acid with magnetic hyperthermia would allow for the therapeutic to remain dormant whilst in circulation, until the remote-activation by an external stimulus that is bio-orthogonal, non-invasive and deeply tissue penetrating [95,96]. This remote control of nucleic acids with magnetic hyperthermia holds promise as a complementary strategy to active targeting for improving biodistribution in-vivo. In particular, the ability to control CFPS and the on-demand release of pharmaceutically active biomolecules from drug delivery vehicles, such as synthetic cells, circumvents any side effects caused by drug leakage during storage and/or in circulation, which may arise from pre-loading vesicles [74]. The development of a platform that harnesses the heat dissipated from magnetic hyperthermia to control the function of nucleic acids has the potential to revolutionise targeted drug delivery, activating the drug itself or catalysing biosynthesis of therapeutically-active biomolecules only at the therapeutic site of interest.

1.5. Summary of thesis work

The overarching aim of this work was to develop a controllable delivery platform, inspired by the SNA architecture, which harnessed the heat dissipated from the clinically-approved anticancer therapy, magnetic hyperthermia, to control the function of nucleic acids. In particular, the aim was to design the technology to be operable within clinically-tolerable magnetic field strengths and frequencies, aiding future translation towards in-vivo studies. This work was partitioned into the following chapters:

Chapter 2 details the design, synthesis, and characterisation of magnetically-activated SNAs that utilise magnetic hyperthermia to selectively release bound ASOs through the denaturation of covalently-attached dsDNA. A breakdown of this chapter includes: the development of the central SNA scaffold comprising superparamagnetic IONPs encapsulated in silica and functionalised with a copper-free click-handle; the conjugation of dsDNA with the "bottom" strand clicked to the SNA and the model ASO "top" strand hybridised on; the development of a novel SNA purification method; the validation of the magnetically-activated SNAs (ASO-bound) in the on-demand degradation of target mRNA only in the presence of the magnetic field, selectively controlling gene knockdown with magnetic hyperthermia.

Chapter 3 details the expansion of the magnetically-activated SNAs towards controlling CFPS (cell-free) of a model protein by way of releasing the T7 promoter sequence in the magnetic field (in replacement of the model ASO sequence). A breakdown of this chapter includes: the modification of the magnetically-activated SNAs with dsDNA comprising the T7 promoter sequence; the synthesis and validation of an inactive DNA template (~1 kb) encoding the protein of interest; the validation of the magnetically-activated SNAs (T7

promoter-bound) in the on-demand control of CFPS, activating the other otherwise inactive DNA template only in the presence of a magnetic field.

Chapter 4 details the encapsulation of the magnetically-activated SNAs (T7 promoter-bound) and an inactive DNA template encoding a protein of interest inside a lipid bilayer, enabling the on-demand production and release of cargo from within synthetic cells only in the presence of a magnetic field. A breakdown of this chapter includes: the encapsulation of the technology developed in Chapter 3 and the activation of biosynthesis inside synthetic cells using magnetic hyperthermia, with and without an opaque blocking material that is impenetrable by current activation methods; the expansion of the drug delivery platform, synthesising an inactive DNA template encoding a pore-forming protein for the selective release of an encapsulated model cargo with magnetic hyperthermia.

2

Design and validation of magnetically-activated spherical nucleic acids

2.1. Introduction

2.1.1 Applications of SNAs

The versatility of the SNA platform gives rise to applications in molecular diagnostics and gene regulation amongst others [42,44,119,120]. The most prevalent SNA architecture is based on a gold (Au) nanoparticle core functionalised with alkylthiolated oligonucleotides, radially-arranged and covalently-bound through the formation of robust Au-sulphur (S) bonds. The unique surface plasmon resonance (SPR) of Au nanoparticles, characterised by the

conduction of electrons on the surface of the nanoparticle resonating with the incident light, has been exploited to develop diagnostic assays [121,122]. SNA probes are designed to hybridise to their complementary target sequence and result in aggregate formation. SPR is highly dependent on the particle size and this reversible aggregation induces the SPR peak to red shift to longer wavelengths, resulting in a visible colour change from red to purple that can be tracked by ultraviolet-visible (UV-Vis) spectroscopy [120,122]. The promise of SNAs as probes for diagnostics is bolstered further by the narrow T_m of the bound oligonucleotides and of their complementary target strand (T_m (SNA) = 2-8 °C) as compared with the free DNA duplex (T_m (dsDNA) = ~10 °C) [42]. This narrow T_m enables high sensitivity, whereby fully complementary target strands can be differentiated from those containing a single base-pair mismatch due to the shift in the T_m of the duplex [122]. Beyond Au nanoparticles, a multitude of inorganic cores have been investigated, including semiconductor quantum dots [123], silica [124] and metal oxides [45]. In particular the incorporation of superparamagnetic IONPs gives rise to additional imaging applications, enabling the visualisation by MRI [45]. Metal complexes (such as gadolinium chelates) have also been conjugated to SNAs, synthesising particles with diagnostic and MRI capabilities [125].

The dense monolayer of DNA-bound SNAs (~50-200 strands per 15 nm particle) results in improved cellular uptake. SNAs are able to self-deliver, on the order of 10^6 copies per cell, into more than 50 different cell types and without additional transfection agents [42]. The exact endocytosis route is dependent on a multitude of factors including the size, surface charge and composition of the SNA core as well as the cell type [43]. However, for endothelial cells it is proposed that serum proteins are adsorbed onto the surface of SNAs and then subsequently displaced by scavenger receptors, mediating cellular uptake [43,126]. SNAs elicit a minimal immune response, whereby the interferon-β level (a signalling molecule produced by the immune system) is ~25 fold less than lipoplexes carrying the same DNA [44,127]. SNAs

are highly stable against flocculation as a result of a highly negative ζ-potential and the high local salt concentration deactivates enzymes in close proximity, culminating in a rate of degradation four times slower than the free duplexes [15,42]. The promise of SNAs and their highly effective gene regulating capabilities has impacted a breadth of research in their clinical translation [15,16,44]. Indeed, siRNA-bound SNAs have successfully downregulated the anti-apoptotic gene *Bcl2L12* that is overexpressed in glioblastomas, slowing tumour growth in murine models with no apparent off-target toxicity [128,129]. In addition to systemic administration, siRNA-bound SNAs have been applied topically to downregulate the gene ganglioside-monosialic acid 3 synthase (*GM3S*) that is overexpressed in diabetic mice and responsible further for insulin resistance and impeded wound healing. Topical treatment with *GM3S*-targeting SNAs resulted in full recovery and wound healing within 12 days in diabetic mice [130]. To this, ASO-bound and liposomal-based SNAs have shown promise in treating psoriasis by targeting the tumour necrosis factor-alpha (TNF-α), successfully suppressing the effect of cytokines and chemokines that lead to the activation of psoriasis [131]. The topical delivery of SNAs to the skin for the treatment of inflammatory skin disorders is being commercialised by Exicure Inc. [15].

2.1.2 Regulation of SNAs with an external stimulus

In spite of the clinical potential offered by SNAs in both diagnostics and gene regulation, there are limited reports of activating and controlling the bound oligonucleotide (predominantly ASO or siRNA) using an external stimulus. There is scope for mediating the lack of specificity within the SNA design and their inability to effectively distinguish between diseased and healthy tissues by rendering the attached ASO or siRNA inactive and unable to perform its downstream function until remote activation at the therapeutic site of

interest [82]. Advances in these controllable SNA systems are limited, with current research focussed on activation via temperature [82], pH [132] or NIR light [94].

Thermally-activated SNAs have been developed by shielding the attached DNA strands with the LCST polymer, pNIPAM [82,83]. The pNIPAM polymer swells and shields the DNA at temperatures below the LCST. In contrast, the pNIPAM polymer contracts at temperatures above the LCST, losing 90% of its volume and exposing the DNA for binding [82,133]. The acidic pH of the lysosome (pH 4.5 – 5) and/or endosome (pH 5.4 – 6.2) has also been exploited by incorporating poly(cytidine) extensions onto SNAs [132]. The poly(cytidine) extension has two roles: to bind to CG-rich DNA duplexes that carry the anticancer drug doxorubicin and to fold into an "i-motif" secondary structure in the presence of acidic pH, thereby destroying the CG-rich DNA duplex and releasing the loaded doxorubicin [132]. The differing pH between tumour tissue (~pH 6.8) and healthy tissue (pH 7.4), and at a cellular level the lysosome and endosome, enables a level of specificity, targeting the therapeutic site of interest [134]. However, issues arise from low accuracy and off-target delivery as a result of the heterogeneity of pH across the tumour environment [135]. In contrast, NIR light allows for spatiotemporal control with deeper penetration in biological tissues (up to 5 mm for NIR ≅ 750 nm) in comparison with UVA light (up to 1 mm for UVA light ≅ 350 nm), and minimal invasive surgery [92,136]. To exploit this, stimuli-responsive DNA (by way of modulating the secondary structure) and LCST polymers have been incorporated onto Au nanorods for the codelivery of siRNA and doxorubicin as described in Section 1.4.2 [94]. Despite its promise, NIR light suffers from limited tissue penetration, giving rise to the necessity to explore alternative stimuli.

2.1.3 Chapter overview

An ideal external stimulus for controlling the function of SNAs is AMFs, which are deeply tissue-penetrating (>10 cm) and biologically benign [95,96]. Superparamagnetic IONPs (<100 nm in diameter) dissipate thermal energy to the surrounding medium as a result of Brownian and Néel fluctuations in the presence of an AMF. This localised heating, termed magnetic hyperthermia, is clinically-proven (and approved) to ablate malignant tumours [99]. The aim of this chapter is to detail the design, synthesis, and characterisation of magnetically-activated SNAs that utilise magnetic hyperthermia to selectively release bound ASOs through the denaturation of covalently-attached dsDNA. This development process described herein consisted of the following activities:

- The development of the central SNA scaffold, comprising the synthesis of superparamagnetic IONPs via thermal decomposition, encapsulation in a biocompatible silica coating via reverse microemulsion, and functionalisation with a copper-free "click" handle.
- The conjugation of dsDNA, whereby the "bottom" strand was "clicked" to the silica shell and the model ASO "top" strand was hybridised on.
- The development and validation of a novel SNA purification method that was critical to rendering the attached ASO inactive in the absence of the applied AMF.
- Testing of the synthesised magnetically-activated SNAs (ASO-bound) in an RNase H-mediated degradation assay with and without magnetic hyperthermia to assess whether AMFs could be used as an external stimulus to selectively release the bound ASO and control gene knockdown with magnetic hyperthermia.

2.2. Development of the central SNA scaffold

2.2.1. Synthesis and characterisation of the magnetic core

The core of the magnetically-activated SNA was designed to incorporate a central magnetic nanoparticle (specifically an IONP) in the superparamagnetic regime (<100 nm). This was to facilitate magnetic hyperthermia, whereby superparamagnetic IONPs act as heating mediators and dissipate thermal energy to their surroundings as a result of Brownian (physical rotation) and Néel (magnetic dipole rearrangement) relaxations [98]. IONPs were synthesised in a one-pot protocol by thermally decomposing iron(III) acetylacetonate in the presence of oleylamine (a strong reducing agent and stabilising ligand) and benzyl ether (a solvent with a high boiling of 296 °C) [137–139]. The reaction mixture was dehydrated at 110 °C (ramp rate of 3 °C min^{-1}) for 1 h under an argon atmosphere, before being heated to 293 °C (ramp rate of 20 °C min^{-1}) and aged at this temperature for 1 h. The advantages of thermal decomposition over more accessible methods that forgo specialist equipment (heating mantle), such as co-precipitation, are three-fold: well-defined particle shape, controlled particle size; and small quantities of organic impurities [140,141].

The oleylamine-capped IONPs were of uniform shape and narrow size distribution, as confirmed by transmission electron microscopy (TEM); analysis of more than 100 individual nanoparticles across multiple different images revealed a diameter of D_{TEM} = 6.4 ± 1.0 nm (mean value ± the standard deviation) (Fig. 2.1).

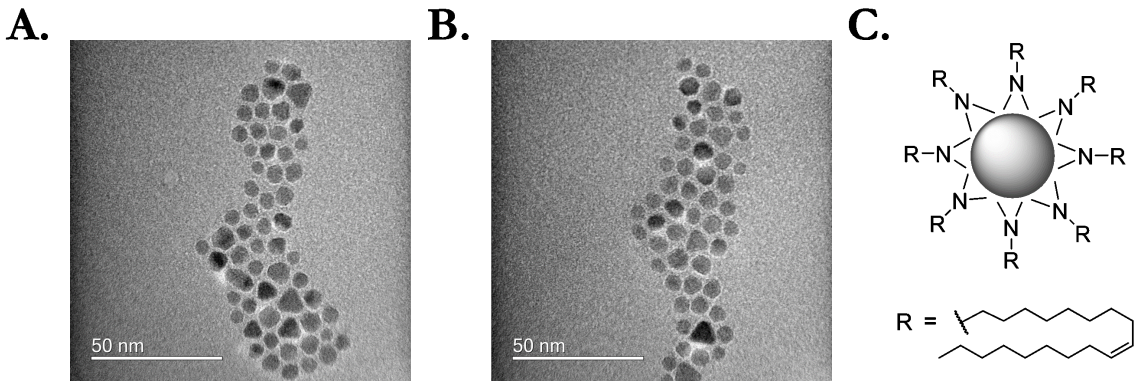

Fig. 2.1. Schematic of oleylamine-capped IONPs and bright field TEM images. (A, B) Bright field TEM images from an identical sample of oleylamine-capped IONPs. **(C)** Chemical structure and schematic oleylamine-capped IONPs.

Further structural information was obtained by X-ray diffraction (XRD), whereby the oleylamine-capped IONPs were crystalline and phase pure with the position and relative intensity of the diffraction peaks matching that of magnetite (RRuff ID: R061111) (Fig. 2.2A) [142]. The crystallite size (D_{XRD}) was calculated using the Scherrer Equation (Eq. 1) and estimated by considering the X-ray wavelength ($\lambda = 0.154$ nm), the crystallite-shape factor for a cubic lattice ($K = 0.9$), and the line broadening at the full half-width maximum of the most intense peak ($\beta = 0.0236$ rad) and its corresponding Bragg angle ($\theta = 0.312$ rad) [141]. The diameter $D_{XRD} = 6.2$ nm was comparable with that determined by statistical analysis of the TEM images, indicating that each particle was a single crystal [143].

$$D_{XRD} = \frac{K\lambda}{\beta \cos(\theta)} \qquad \textbf{Eq. 1}$$

Dynamic light scattering (DLS) was utilised to investigate the hydrodynamic size of the nanoparticles and proved larger than the crystallite size at $D_{DLS} = 8.4$ nm, taking into account the fluid interactions and adsorbed surfactant (Table 1).

Table 1. Oleylamine-capped IONP characterisation. Summary of the hydrodynamic diameter (analysis in number) and polydispersity index (PDI), as determined by DLS with the mean calculated from n = 3 repeat measurements.

Nanoparticle	Hydrodynamic diameter (nm)	PDI
Oleylamine-capped IONPs	8.4	0.43

The hysteresis curve measured at 300 K determined that the oleylamine-capped IONPs were superparamagnetic at room temperature with zero coercivity, in-turn confirming that the net magnetisation in the absence of an external field was zero (Fig. 2.2B). Their saturation magnetisation plateaued at 56.0 emu g_{Fe}^{-1}, a property which influences the thermal energy dissipated in an AMF with high saturation magnetisation values resulting in greater inductive heating [144].

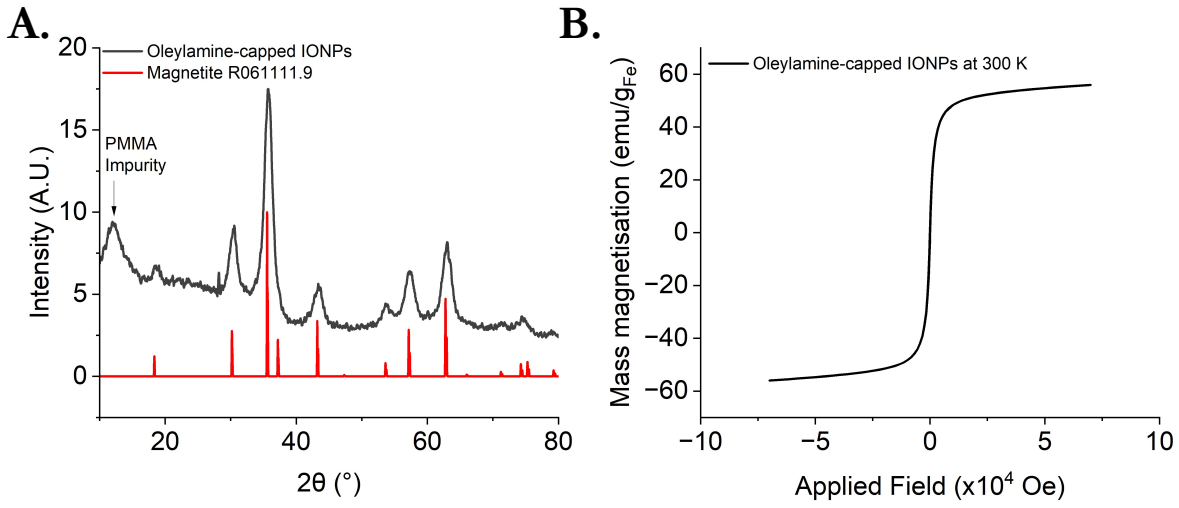

Fig. 2.2. Characterisation of oleylamine-capped IONPs. (A) XRD pattern of oleylamine-capped IONPs indexed against magnetite (RRuff ID:R061111). **(B)** Hysteresis curve of oleylamine-capped IONPs measured at 300 K.

2.2.2. Synthesis and characterisation of the silica shell

The oleylamine-capped IONPs were encapsulated in a silica (SiO_2) shell to obtain biocompatible iron oxide silica core-shell nanoparticles (IONPs@SiO_2) with a readily modifiable surface chemistry. The reverse microemulsion method was chosen for enhanced morphological control and reduced yields of by-product SiO_2 with no IONP core [145]. The oleylamine-capped IONPs were suspended in cyclohexane and underwent a ligand exchange with the amphiphilic surfactant, polyoxyethylene-5-nonylphenylether (IGEPAL-*co*-520) (Fig. 2.3). The addition of concentrated aqueous ammonium hydroxide influenced micelle formation, whereby the amphiphilic nature of IGEPAL-*co*-520 enabled the hydrophobic groups to extend outwards into the cyclohexane and the hydrophilic groups to extend inwards into the aqueous ammonium hydroxide phase [146]. The silica source, tetraethylorthosilicate (TEOS), was hydrolysed into silanol monomers in the aqueous domain that in-turn condensed with neighbouring silanol monomers and later siloxane network clusters on the surface of the nanoparticle to form SiO_2 shells around single IONP cores [147]. In the final step, 3-aminopropyltriethoxysilane (APTES) was added to modify the surface of the IONPs@SiO_2 with reactive amine (NH_2) groups.

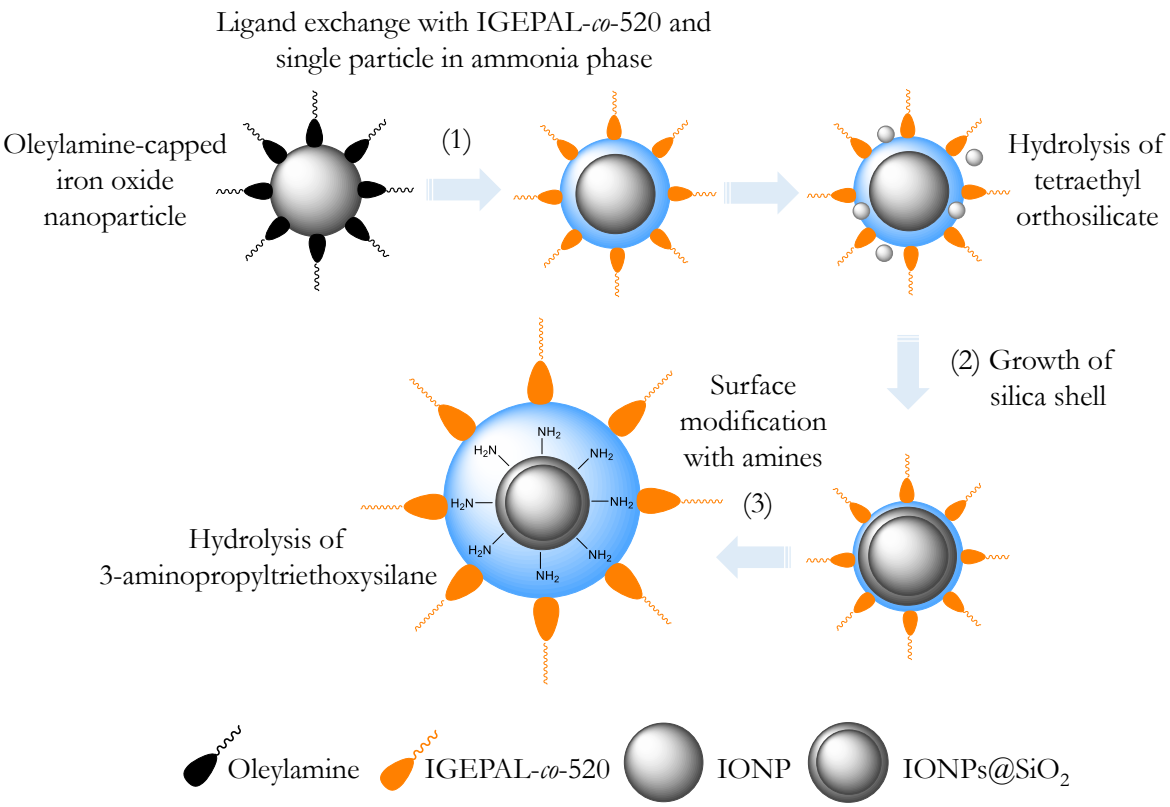

Fig. 2.3. Schematic detailing the reverse microemulsion method for synthesising IONPs@SiO_2. Oleylamine-capped IONPs underwent ligand exchange with the surfactant IGEPAL-*co*-520 and form single IONPs within aqueous domains in the presence of concentrated ammonium hydroxide **(1)**. Tetraethylorthosilicate was nucleated in the presence of aqueous ammonium hydroxide and was subject to hydrolysis and condensation on the surface of the IONP, thereby growing the silica shell **(2)**. (3-aminopropyl)triethoxysilane) was added to modify the surface of the IONPs@SiO_2 with NH_2 groups **(3)**.

The NH_2-modified IONPs@SiO_2 were characterised by TEM, revealing monodisperse particles with a diameter of D_{TEM} = 20.9 ± 1.8 nm (mean value ± the standard deviation) and no observed by-product SiO_2 (Fig. 2.4).

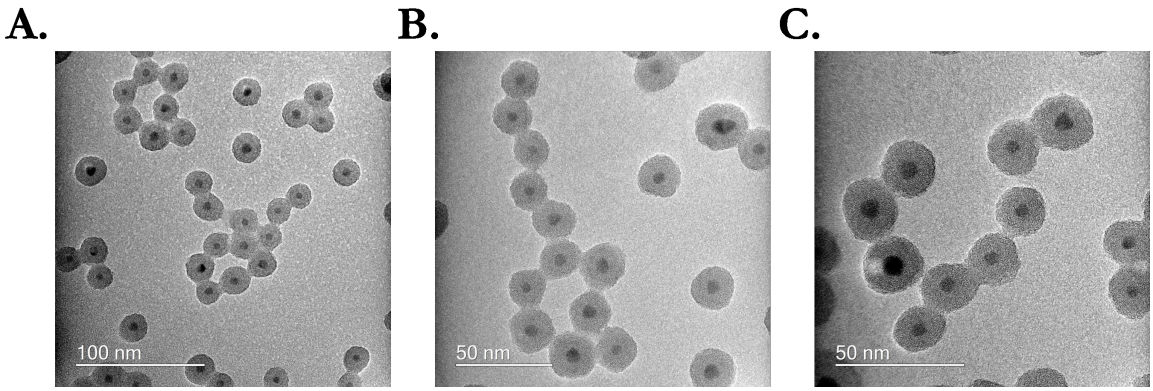

Fig. 2.4. Bright field TEM images of NH_2-modified IONPs@SiO_2. (A-C) Bright field TEM images of an identical sample of NH_2-modified IONPs@SiO_2.

DLS was utilised to investigate the hydrodynamic size after encapsulation and synthesis of NH_2-modified IONPs@SiO_2, which increased the mean diameter to D_{DLS} = 36.7 nm. The ζ-potential further indicated the addition of protonatable NH_2 groups with a measured charge of ζ = +17.8 mV (Table 2).

Table 2. NH_2-modified IONPs@SiO_2 characterisation. Summary of the hydrodynamic diameter (analysis in number), PDI and ζ-potential, as determined by DLS with the mean calculated from n = 3 repeat measurements.

Nanoparticle	Hydrodynamic diameter (nm)	PDI	ζ-potential (mV)
NH_2-modified IONPs@SiO_2	36.7	0.38	17.8

2.2.3. Modification with the DBCO click-handle

A copper-free click-handle was installed on the surface of the NH_2-modified IONPs@SiO_2 by coupling to an NHS ester-modified dibenzocyclooctyne (DBCO). The success of the reaction was tracked by UV-vis spectroscopy and the absorbance of DBCO at its excitation maximum wavelength of 309 nm (Fig. 2.5). The shoulder associated with the DBCO peak may be indicative of a partial rearrangement, leading to an analogue of DBCO with an

identical mass, but without the reactive alkyne group [148]. Future strategies to prevent this rearrangement to an inactive analogue include coordinating Cu(I) prior to storage.

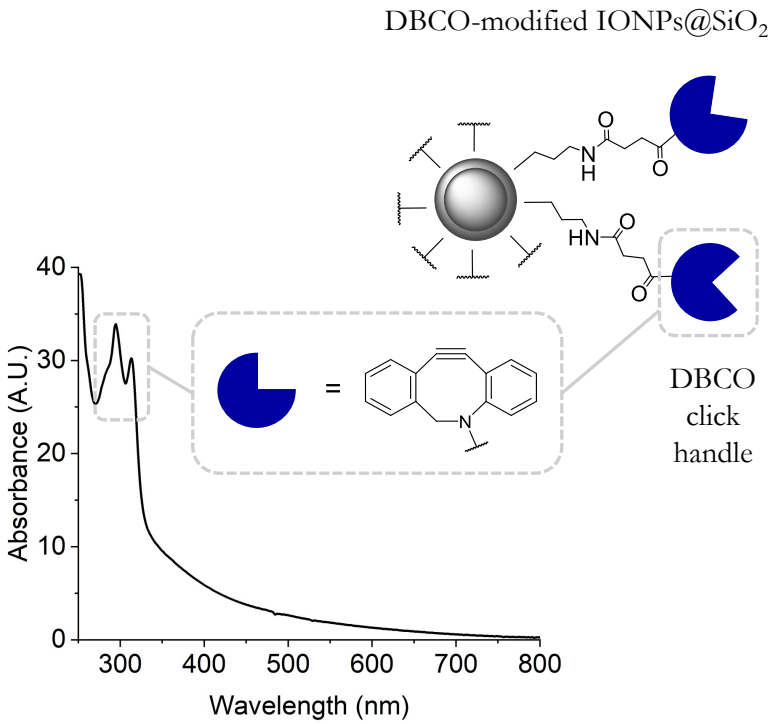

Fig. 2.5. Characterisation of DBCO-modified IONPs@SiO_2. UV-vis spectrum of DBCO-modified IONPs@SiO_2 synthesised by NHS ester-coupling, highlighting the characteristic DBCO absorption.

The Beer Lambert Law (Eq. 2) was used to determine the concentration of DBCO (c_{DBCO}) in units of mol·dm^{-3} at a molar extinction coefficient of ε = 12,000 $M^{-1}cm^{-1}$ (309 nm), taking into account the absorbance (Abs) (measured at 309 nm) and the path length (l) of 1 cm [149].

$$\mathrm{Abs} = \varepsilon c_{DBCO} l \qquad \textbf{Eq. 2}$$

Avogadro's number (N_A) was then used to calculate the number of DBCO molecules (N_{DBCO}) present in a known volume by multiplying N_A by moles of DBCO in units of mol (Eq. 3).

$$N_{DBCO} = N_A \times mol_{DBCO} \qquad \textbf{Eq. 3}$$

The number of DBCO molecules was divided by the total number of nanoparticles present in a known volume. This nanoparticle concentration in units of particles·ml^{-1} was calculated according to previous literature [150–153]. In essence, each individual IONPs@SiO_2 was approximated as spherical in shape. The mass of the individual core-shell IONPs@SiO_2 ($m_{core\text{-}shell}$) was estimated using the radii of both the core IONPs (r_{core}) and core-shell IONPs@SiO_2 ($r_{core\text{-}shell}$) from TEM analysis, and the known densities of silica (ρ = 2.20 g·cm^{-3}) and magnetite (ρ = 5.24 g·cm^{-3}) (Eq. 4–6). The concentration of the core-shell IONPs@SiO_2 ($N_{core\text{-}shell}$) was calculated from the mass concentration of nanoparticles in units of mg·mL^{-1} (M_C) and the mass of the individual core-shell IONPs@SiO_2 ($m_{core\text{-}shell}$) (Eq. 7).

$$m_{core} = \frac{3}{4}\pi\, r_{core}^3\, \rho_{magnetite} \qquad \textbf{Eq. 4}$$

$$m_{shell} = \frac{3}{4}\pi \left(r_{core-shell}^3 - r_{core}^3\right) \rho_{silica} \qquad \textbf{Eq. 5}$$

$$m_{core-shell} = m_{core} + m_{shell} \qquad \textbf{Eq. 6}$$

$$N_{core-shell} = \frac{M_C}{m_{core-shell}} \qquad \textbf{Eq. 7}$$

The resulting number of DBCO molecules decorating each core-shell nanoparticle averaged 4000. DLS measurements inferred the successful modification by DBCO with an increase in hydrodynamic diameter from D_{DLS} = 36.7 nm for NH_2-modified IONPs@SiO_2 compared with D_{DLS} = 142.0 nm for DBCO-modified IONPs@SiO_2, suggestive of the aggregation induced by the addition of bulky and hydrophobic DBCO groups. A shift in surface charge from ζ = +17.8 mV to ζ = -13.9 mV (Table 3) is consistent with the change in surface chemistry.

Table 3. DBCO-modified IONPs@SiO_2 characterisation. Summary of the hydrodynamic diameter (analysis in number), PDI and ζ-potential, as determined by DLS with the mean calculated from n = 3 repeat measurements.

Nanoparticle	Hydrodynamic diameter (nm)	PDI	ζ-potential (mV)
DBCO-modified IONPs@SiO_2	142.0	0.20	-13.9

2.3. Conjugation of DNA

2.3.1. Modification with the azide click-handle

Tethering the dsDNA to the DBCO-modified IONPs@SiO_2 was important to maximise the localised heating experienced by the dsDNA as a result of magnetic hyperthermia, in-turn influencing the amount of the model DNA strand released for downstream applications. Copper-free strain-promoted azide-alkyne cycloaddition (SPAAC) was utilised to conjugate the dsDNA, comprising the carrier strand (denoted the "bottom" strand) "clicked" to the DBCO-modified silica shell and the model strand (denoted the "top" strand), in this case an ASO sequence, hybridised on (Fig. 2.6A,B). The ASO (18 base sequence) was optimised by previous members of the Booth group to target and selectively degrade mRNA encoding the fluorescent protein mVenus [88,88,90]. This ASO served as a proof-of-concept, enabling the use of an RNase H-mediated mRNA degradation assay and the selective release of the hybridised ASO to track the cleavage of mVenus mRNA both with and without exposure of the dsDNA-modified IONPs@SiO_2 to an AMF. The theoretical T_m of the annealed dsDNA ASO was calculated[154] to be ~71 °C, factoring in the salt concentrations required for the RNase H assay (100 mM potassium chloride (KCl) and 20 mM magnesium chloride ($MgCl_2$)) and providing a benchmark for the theoretical thermal energy required to denature the double helix and release the ASO "top" strand for controlling gene knockdown downstream. It was important to design dsDNA with a robust T_m to prevent the ASO "top"

strand from releasing in the absence of magnetic hyperthermia and engineer a more efficient "off" state.

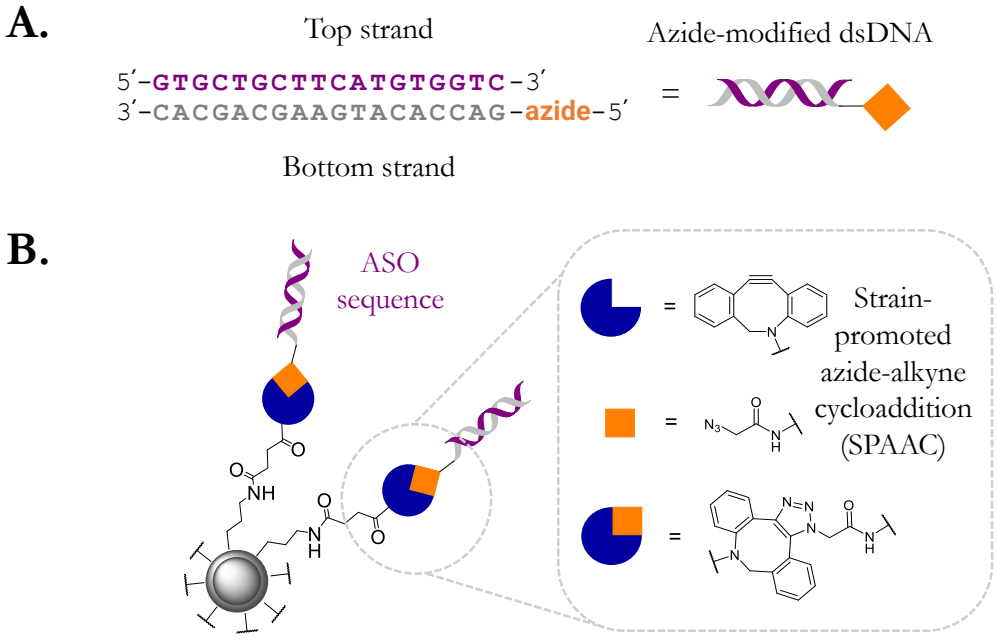

Fig. 2.6. Schematic of spherical nucleic acid synthesis. (A) Schematic showing the sequences of the "top" and "bottom" (azide-modified) ASO strands. **(B)** Schematic detailing the conjugation of the dsDNA, comprising the "bottom" strand covalently bonded to the DBCO-modified silica shell through SPAAC and the "top" strand, in this case an ASO sequence targeting mVenus mRNA, hybridised on to synthesise the SNA.

To enable the modification of the commercially-available NH_2-modified DNA, 2-azidoacetic acid NHS ester was synthesised by activating the carboxylic acid in 2-azidoacetic acid with NHS and *N*,*N*'-dicyclohexylcarbodiimide (DCC) chemistry (Fig. 2.7A) [155]. The bifunctional 2-azidoacetic acid NHS ester was synthesised at a yield of 23% and the product was characterised by proton nuclear magnetic resonance (^{1}H NMR) spectroscopy to reveal chemical shifts at 2.81 ppm (amide protons) and 4.17 ppm (NHS ester protons). The T7 promoter "bottom" strand was modified with an azide (N_3) click-handle by reacting 2-azidoacetic acid NHS ester with the commercially-available "bottom" strand, which had an active primary amine group at the 5′-end from the

incorporation of a six-carbon amino linker. The resulting N_3-modified "bottom" strand was characterised by oligonucleotide mass spectrometry, which confirmed the successful NHS ester coupling with its major peak (2) reflecting the expected molecular mass of 5748 Da (Fig. 2.7B). The minor peak (1) is an impurity of the "bottom" DNA strand with no active six-carbon amino linker. The DNA was not purified further as the impurity with no N_3 modification was not expected to interfere with the SPAAC or indeed react with the DBCO-modified IONPs@SiO_2.

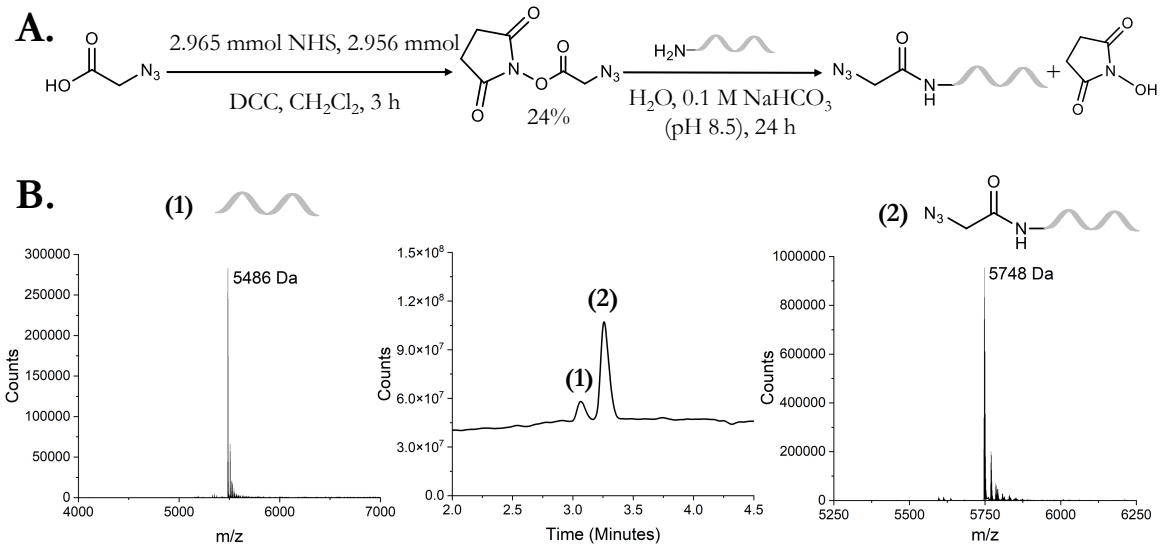

Fig. 2.7. Schematic of azide-modified DNA synthesis and characterisation. (A) Reaction scheme for the synthesis of 2-azidoacetic acid NHS ester and its subsequent conjugation to amine-modified DNA, yielding the desired azide-modified DNA product. **(B)** Oligonucleotide mass spectrometry of the azide-modified DNA "bottom" strand, whereby the major peak (2) deconvolutes to give the expected mass of 5748 Da, indicating a successful terminal modification and the minor peak (1) corresponds to the "bottom" DNA strand with no active six-carbon amino linker.

This N_3-modified "bottom" DNA strand and the NH_2-modified "bottom" strand were annealed to the unmodified "top" ASO strand and analysed by poly(acrylamide) gel electrophoresis (PAGE) (Fig. 2.8). The annealed dsDNA is of higher molecular mass than the individual (separate) "top" and "bottom" DNA strands for both the dsDNA with (N_3-

dsDNA) and without (NH_2-dsDNA) the click-handle and therefore the dsDNA travels a shorter distance through the PAGE gel in the direction of the electric current. The absence of bands associated with the free "top" ASO and/or "bottom" DNA strands and the presence of a single band in both of the lanes associated with the dsDNA indicates the success of the annealing reaction.

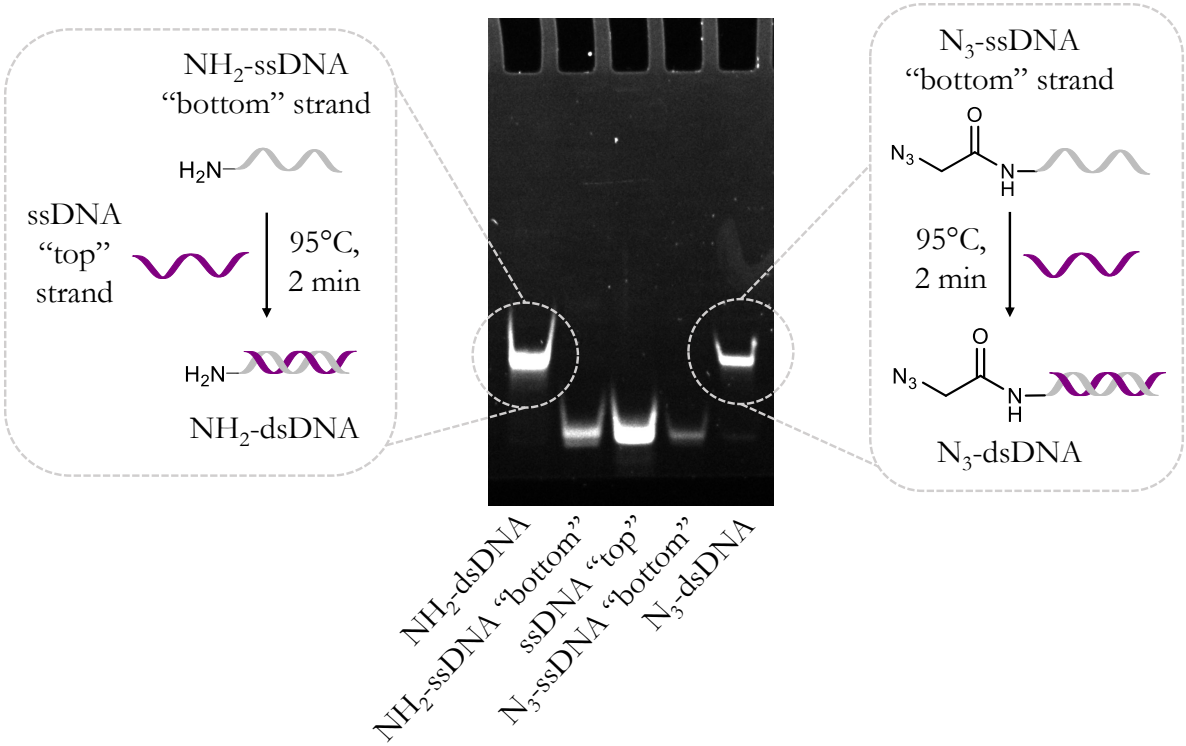

Fig. 2.8. Quantification of dsDNA ASO formation. Native 16% (volume/volume) (v/v) PAGE tracking the successful annealing of the DNA "bottom" strand with (N_3-ssDNA "bottom", right-hand side schematic) and without (NH_2-ssDNA "bottom", left-hand side schematic) the N_3 click-handle to the ASO top strand (ssDNA "top"), and the resulting dsDNA with (N_3-dsDNA) and without (NH_2-dsDNA) the click-handle. The dsDNA is of higher molecular mass and so travels slower down the gel in the direction of the electric current (top to bottom of the gel).

2.3.2. Synthesis and characterisation of the SNAs

The SNA synthesis was carried out by reacting the N_3-modified dsDNA ASO onto the surface of the DBCO-modified IONPs@SiO_2 by SPAAC. The N_3-modified dsDNA was

frozen in the presence of DBCO-modified IONPs@SiO_2 and low concentrations of salt, mimicking the freeze-directed synthesis of SNAs [156]. The reaction was placed in a refrigeration bath at -7 °C for 4 h prior to freezing at -20 °C overnight, taking advantage of ice crystals gradually forming, concentrating the reagents into "micro-pockets" and alleviating steric and electrostatic hindrances, thereby encouraging SNA formation [156,157]. Excess dsDNA is critical to the success of the freeze-directed synthesis and SNA formation [156]. More specifically it was found that a final dsDNA concentration of 3 μM was necessary for the successful SNA formation with the nanoparticles at a final concentration of 5 $mg \cdot ml^{-1}$. The success of the reaction and SNA formation was monitored initially by tracking the change in ζ-potential to highly negative values, indicative of the presence of the negatively charged phosphate backbones associated with the loaded DNA. In addition, a control system comprising dsDNA without the click-handle (NH_2-modified dsDNA) was employed. The NH_2-modified dsDNA lacks the reactive group to covalently-bond to the DBCO-modified IONPs@SiO_2, thus any dsDNA detected on the surface of the nanoparticles is likely to be electrostatically-bound (non-specifically adsorbed). High concentrations of DNA were adsorbed to the surface of the nanoparticles (alongside the attachment of covalently-bound DNA) with the freeze-directed method, as inferred from the negative ζ-potential of both the SNAs synthesised with dsDNA modified with (ζ = -55 mV) and without (ζ = -41 mV) the click-handle (Fig. 2.9).

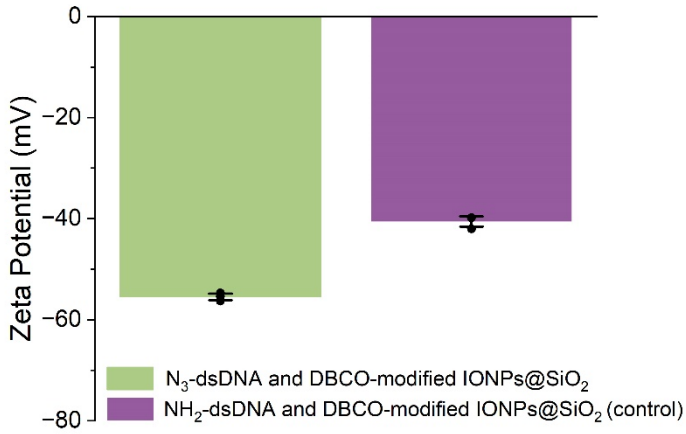

Fig. 2.9. ζ-potential data for the freeze-directed synthesis of spherical nucleic acids. ζ-potential data for SNAs synthesised with dsDNA modified with and without the click-handle with a highly negative ζ-potential observed for both species, suggesting that the dsDNA without the click-handle is non-specifically adsorbing to the surface of the nanoparticles.

This nonspecific adsorption posed issues for the downstream application, as inferred by an RNase H-mediated mRNA degradation assay in the absence of magnetic hyperthermia. The optimised ASO forms a characteristic DNA-RNA heteroduplex with the target mRNA encoding the fluorescent protein mVenus. The RNase H enzyme recognises the heteroduplex as a substrate and hydrolyses the phosphodiester bonds of the target mRNA. The RNase H-mediated degradation of the target mRNA into two smaller RNA fragments (A and B) was tracked by agarose gel electrophoresis (Fig. 2.10A). The SNA synthesised with the dsDNA ASO catalysed the degradation of mRNA encoding mVenus (~1 kb) without the application of magnetic hyperthermia. This was determined by the absence of a single band on the agarose gel associated with the intact mRNA (comparable with the lane with no ASO present) and the presence of multiple bands of lower molecular weight (comparable with the lane with the ASO present) (Fig. 2.10A). It was hypothesised that the adsorbed dsDNA leaches into solution under physiological conditions and results in the SNA being active and catalysing the degradation of target mRNA without the application of magnetic hyperthermia (Fig. 2.10B). Significant nonspecific adsorption, characterised by

dsDNA noncovalently-binding to the surface of the nanoparticles, was therefore detrimental to the controlled release mechanism.

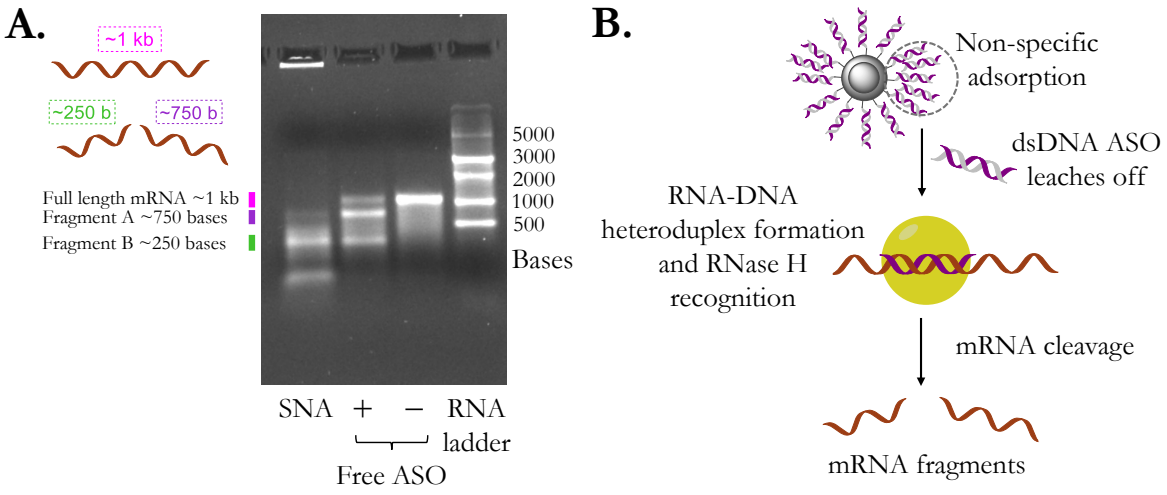

Fig. 2.10. Quantification of the effects of dsDNA non-specific adsorption. (A) 1.5% (weight/volume) (w/v) agarose gel showing the degradation of mRNA encoding mVenus (~1 kb) without the application of magnetic hyperthermia and in the presence of SNAs synthesised with dsDNA ASO, determined by the absence of a single band on the agarose gel associated with the intact mRNA (comparable with lane three with no ASO present, denoted – ASO) and the presence of multiple bands of lower molecular weight (comparable with lane two with the ASO present, denoted + ASO). **(B)** Schematic detailing the leaching of adsorbed dsDNA ASO from the surface of the nanoparticles and in the absence of an AMF, catalysing the RNase H-mediated degradation of target mRNA into two smaller fragments (A and B) without the application of magnetic hyperthermia.

2.4. Development and validation of the novel SNA purification

2.4.1. Minimising nonspecific adsorption of DNA

A variety of alternative methods were explored, aiming to maximise dsDNA loading whilst minimising the nonspecific adsorption. The most prevalent method for synthesising SNAs involves slowly increasing the concentration of sodium ions to either ≤0.15 M (no surfactant) or ≤2 M (surfactant), known as "salt-aging" [42]. The addition of positively charged sodium ions screen the repulsive interactions between neighbouring DNA strands, thereby encouraging higher densities of DNA to assemble on the surface of the

nanoparticles. The inclusion of a surfactant (such as TWEEN® 20) is critical to both maintaining stability, passivating the surface of the nanoparticles and preventing aggregation, and promoting the desorption of pre-adsorbed biomolecules [42,158,159]. Initially SPAAC was carried out in Milli-Q water with TWEEN® 20 (a surfactant chosen in accordance with the literature [42,159]). This yielded SNAs with dsDNA electrostatically-bound to the surface of the nanoparticle, as inferred from the negative ζ-potential of both the SNAs synthesised with dsDNA modified with (ζ = -14 mV) and without (ζ = -11 mV) the click-handle (Fig. 2.11A). Salt-aging (with the addition of TWEEN® 20) was explored, however, this method was also ineffective at preventing the nonspecific adsorption of dsDNA with a negative ζ-potential observed for SNAs synthesised with dsDNA modified with (ζ = -13 mV) and without (ζ = -19 mV) the click-handle (Fig. 2.11A).

To combat the evident nonspecific adsorption from conventional SNA synthesis methods, increasing the concentration of salt [160] and heating in buffer [161–163] were investigated (as recommended in the literature). There was a positive trend between increasing the concentration of sodium chloride (NaCl) and decreasing the extent of nonspecific adsorption, as determined from the observed ζ-potential values becoming incrementally more positive for reactions with the control dsDNA without the click-handle and in response to increasing concentrations of NaCl (from 0.5 – 1 M) (Fig 2.11B). However, this was at the expense of DNA loading as the increased salt concentration caused the nanoparticles to crash out of solution due to the "salting-out" effect [164]. The most promising set of conditions with 0.1 M 3-morpholinopropane-1-sulfonic acid (MOPS) buffer and 0.5 M NaCl were chosen to take forward into experiments investigating the effects of heating the SNAs in tris-ethylenediaminetetraacetic acid (TE) buffer post synthesis. SNAs with and without the click-handle were subjected to heating in TE buffer at 55 °C for 5 min with shaking at 800 rpm. Indeed, there was an apparent desorption of pre-adsorbed dsDNA from the surface

of the nanoparticles, tracked by the recovery of the ζ-potential to more positive values in the control SNA and with dsDNA that did not contain the click-handle (Fig. 2.11C). After heat treatment, the SNA with the click-handle maintained a highly negative ζ-potential (ζ = -46 mV before and ζ = -38 mV after TE treatment), whereas the SNA without the click-handle (control) experienced a shift to more positive ζ-potential values (ζ = -14 mV before and ζ = 6 mV after TE treatment). However, concerns were raised about this method because the model DNA "top" strand, which is hybridised onto the "bottom" carrier strand, has the potential to be released as a result of the heat exposure. This is likely to impact the overall loading of the "top" strand, reducing the concentration of functional DNA that is released selectively as a result of magnetic hyperthermia and in-turn impacting the "on" state and efficiency of the technology.

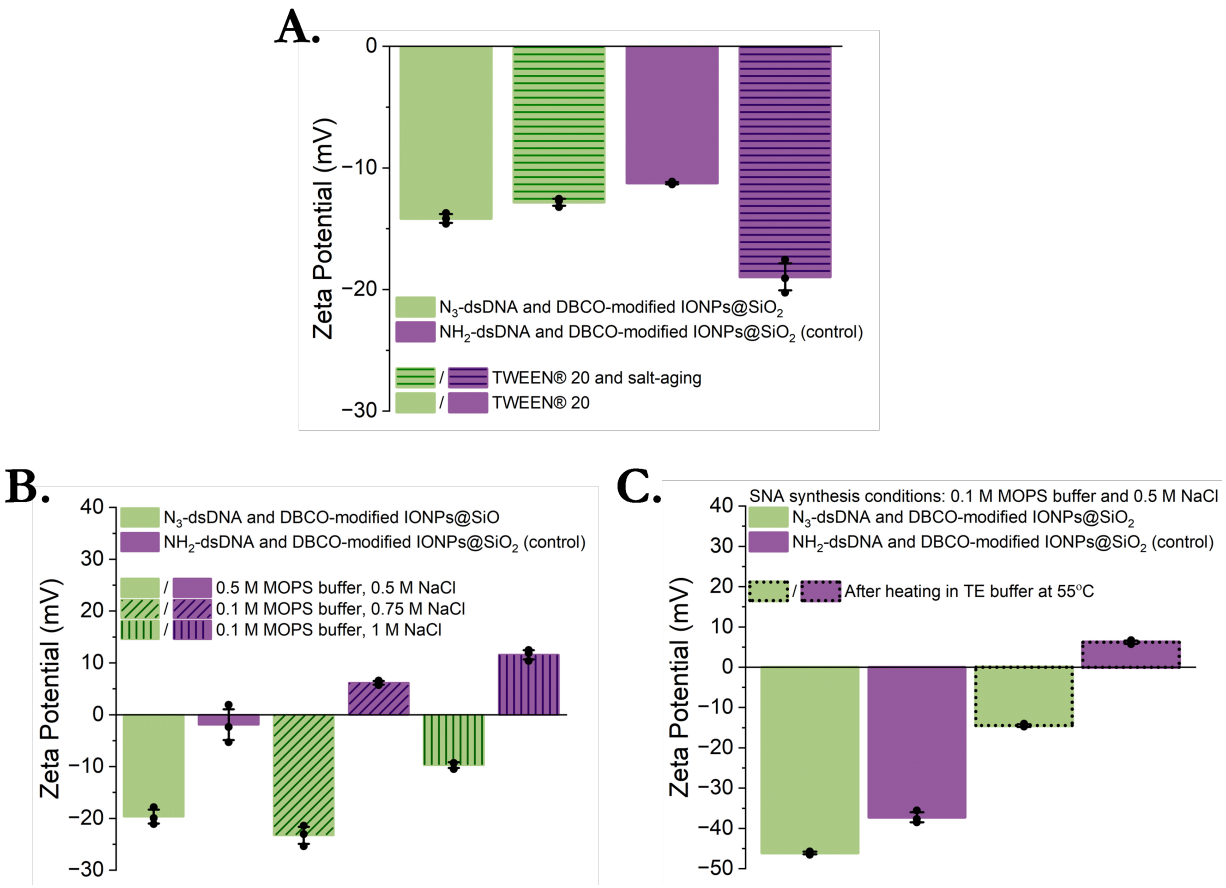

Fig. 2.11. ζ-potential data and evaluation of dsDNA nonspecific adsorption to the surface of the nanoparticles. (A) ζ-potential data from SPAAC in Milli-Q water with TWEEN® 20 and separately employing salt-aging (and TWEEN® 20), the persistence of nonspecific adsorption was inferred from the negative ζ-potential of both the SNAs synthesised with dsDNA modified with and without the click-handle. **(B)** ζ-potential data from SPAAC with increasing concentrations of NaCl, showing a positive trend, whereby nonspecific adsorption decreased in response to increasing concentrations of NaCl (from 0.5 – 1 M) as inferred by the ζ-potential values become incrementally more positive for reactions with the control dsDNA without the click-handle. **(C)** ζ-potential data from heating the SNAs in TE buffer at 55 °C, showing desorption of pre-adsorbed dsDNA from the surface of the nanoparticles that was tracked by the recovery of the ζ-potential to more positive values in the control SNA and with dsDNA that did not contain the click-handle.

2.4.2. Development of the novel SNA purification

To mediate this, a novel purification method was developed to produce SNAs decorated solely with covalently-bound DNA. The method stemmed from the observation that the SNAs remained in the well of a 1.5% (w/v) agarose gel. This was determined both visually,

by the retention of a brown band in the well, and fluorometrically, by the evident fluorescence associated with the binding of the nucleic acid stain GelRed® to the dsDNA attached to the surface of the nanoparticles (Fig. 2.10). The newly-developed purification involved pulling pre-adsorbed DNA from the surface of the nanoparticle using an electric current that was applied through a 1.5% (w/v) agarose gel; the covalently-constructed SNA did not travel through the gel and was then extracted through brief sonication of the excised well in Milli-Q water (Fig. 2.12).

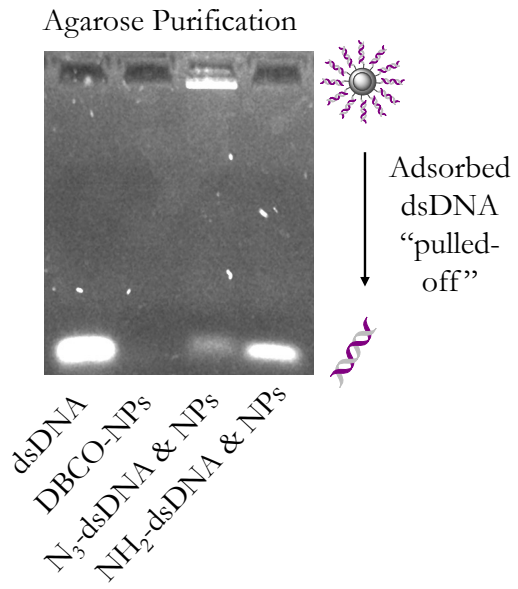

Fig. 2.12. Novel purification for spherical nucleic acids. 1.5% (w/v) agarose gel showing the novel purification developed for SNAs, successfully removing adsorbed dsDNA from the surface of the nanoparticles using an electric current. The covalently-constructed SNA (with the azide-modified dsDNA) did not travel through the gel and was then extracted through brief sonication of the excised well in Milli-Q water (lane three). The electrostatically-bound dsDNA was pulled-off by applying an electric current to the 1.5% (w/v) agarose gel and can be seen to travel through the gel at a comparable rate with the free dsDNA (lane one). The majority of the electrostatically-bound dsDNA was pulled-off the SNA constructed with amine-modified dsDNA only (lane four, control sample).

The resulting covalently-constructed SNA (synthesised with the N_3-modified dsDNA) remained colloidally stable as determined by the highly negative ζ-potential induced by the phosphate DNA backbone, decreasing to $\zeta = -38.9$ mV from $\zeta = -13.9$ mV for DBCO-

modified IONPs@SiO_2. The decrease in hydrodynamic diameter to D_{DLS} = 112.2 nm upon SNA formation, as compared with D_{DLS} = 142.0 nm for DBCO-modified IONPs@SiO_2, is indicative of the newly-formed and monodisperse colloid, stabilised by DNA-to-DNA electrostatic repulsion (Table 4).

Table 4. dsDNA-modified IONPs@SiO_2 (SNA) characterisation. Summary of the hydrodynamic diameter (analysis in number), PDI and ζ-potential, as determined by DLS with the mean calculated from n = 3 repeat measurements.

Nanoparticle	Hydrodynamic diameter (nm)	PDI	ζ-potential (mV)
dsDNA-modified IONPs@SiO_2	112.2	0.37	-38.9

2.4.3. Determination of DNA loading

The ASO loading was determined by denaturing the dsDNA attached to the IONPs@SiO_2 at 95 °C for 5 min in urea-containing dye and comparing the amount of released DNA to a calibration curve of known concentration on a 1.5% (w/v) agarose gel (Fig. 2.13). In a similar vein to calculating the number of DBCO molecules loaded onto a single nanoparticle (detailed in Section 2.2.2 and in accordance with previous literature [150–153]), the concentration of attached ASO strands was related to the calculated nanoparticle concentration in units of particles·ml^{-1} to give an estimated loading of 5 dsDNA per nanoparticle, which is in-line with literature values for SNAs comprising dsDNA[156].

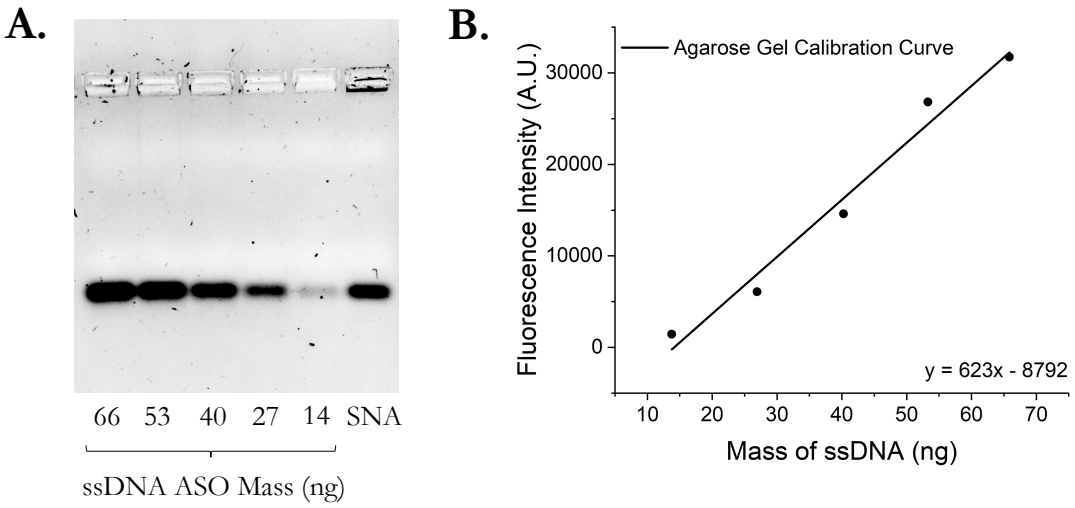

Fig. 2.13. Calibration curve to determine SNA ASO loading. (A) 1.5% (w/v) agarose gel of known masses of the free ASO and a known volume of SNA heated at 95 °C in urea-containing dye to release the bound ASO. Due to SNA volume/concentration constraints, the data is indicative of n = 1 biological repeats. **(B)** Calibration curve of the nucleic acid stain GelRed® fluorescence intensities (determined by ImageJ software) against the known ASO mass, the linear regression (fitted in Origin) was used to extrapolate the concentration of bound ASO strands on individual SNAs.

2.5. Magnetic control of gene knockdown

The newly-developed SNAs (ASO-bound) were tested in an RNase H-mediated degradation assay with and without magnetic hyperthermia. The aim was to probe whether AMFs could be used as an external stimulus to selectively release the bound ASO and control gene knockdown. The mass of bound ASO was determined as described previously (Section 2.4.2) and was maintained in-line with that conventionally used in an RNase H assay (2 ng of ASO). The AMFs were generated using an NAN201003 Magnetherm (Nanotherics Ltd) with an 18-turn coil of 50 mm internal diameter (Fig. 2.14A). The magnetic field strength and frequency were optimised to obtain the maximum global heating, determined by a fibre optic probe submerged in solution, in a minimum timeframe and with 2 ng of ASO. Additional considerations included: a frequency compatible with the only clinically-available magnetic hyperthermia system (MagForce), which operates at a

frequency of 100 kHz in order to minimise eddy currents within the body and reduce patient discomfort [102]; a magnetic field-frequency product below the safety limits proposed by Hergt *et al* [118] ($H \times f = 5 \times 10^9$ A·m^{-1}·s^{-1}). As such the AMF parameters chosen were a magnetic field strength of 30 mT and a frequency of 103.4 kHz (the latter value is fixed by the 200 nF capacitor on the Magnetherm), for which $H \times f = 2.47 \times 10^9$ A·m^{-1}·s^{-1}.

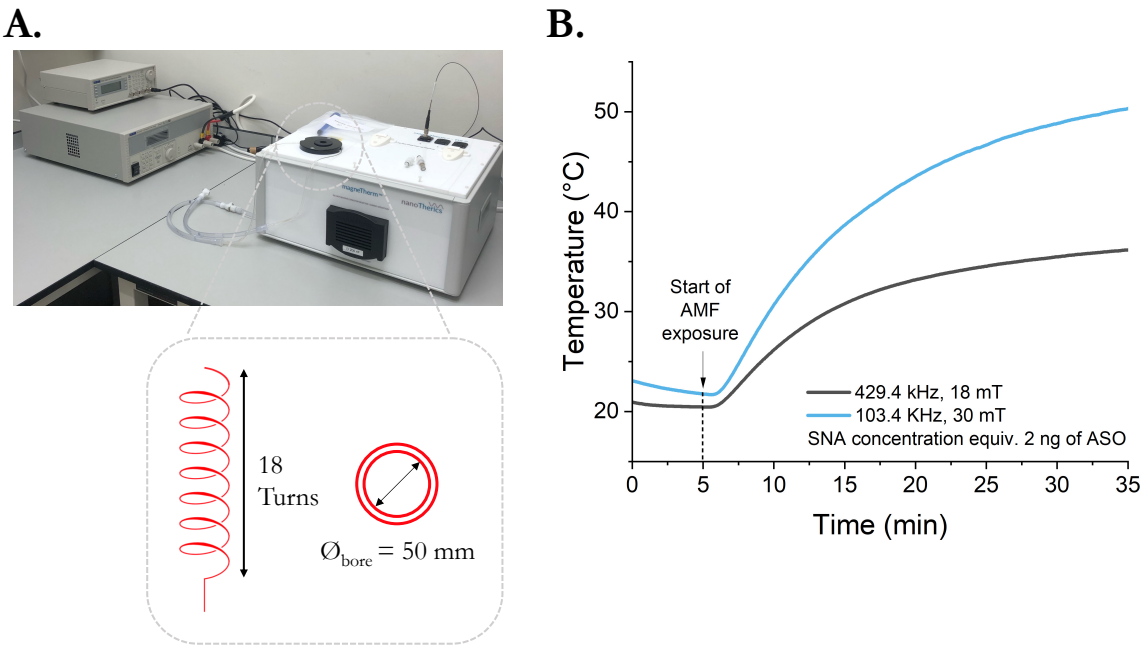

Fig. 2.14. AMF set-up and optimised parameters. (A) NAN201003 Magnetherm (Nanotherics Ltd) system fitted with an 18-turn coil of 50 mm internal diameter. **(B)** Global heating over time, determined by a fibre optic probe submerged in solution, in the presence of 2 ng of ASO total with a magnetic field strength of 18 mT or 30 mT and a frequency of 429.4 kHz or 103.4 kHz.

The ASO-bound SNAs were exposed to an AMF (30 mT, 103.4 kHz) for 90 min, whereby sufficient localised heating was observed to denature the bound dsDNA and release the ASO selectively for cognate mRNA binding. The characteristic DNA-RNA heteroduplex with the target mRNA encoding the mVenus protein was successfully recognised by the RNase H enzyme and the RNA portion was cleaved into two smaller fragments (A and B). The degraded mRNA fragments were tracked by agarose gel electrophoresis (Fig. 2.15). The

ASO-bound SNA catalysed the degradation of the mRNA transcript (~1 kb) only in the presence of the applied AMF, determined by the absence of a single band on the agarose gel associated with the intact mRNA (comparable with the lane with no ASO present) and the presence of multiple bands of lower molecular weight (comparable with the lane with the ASO present). The mRNA remained intact in the presence of the ASO-bound SNA and in the absence of magnetic hyperthermia, as determined by the retention of a single band on the agarose gel. This was indicative of the efficient "off" state that was only possible after the newly-developed agarose purification.

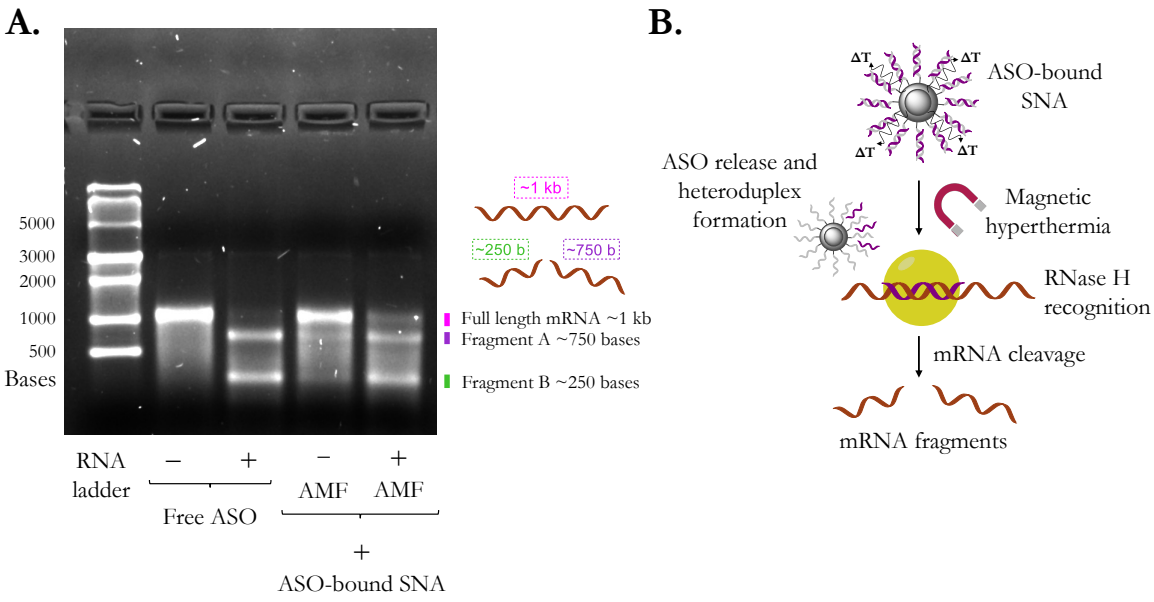

Fig. 2.15. Magnetic control of gene knockdown. (A) On-demand gene knockdown only in the presence of an AMF. The mRNA transcript encoding mVenus (~1 kb) remained intact when no ASO was present and was subsequently cleaved into two smaller RNA fragments (A at ~750 bases and B at ~250 bases) by the recruitment of the RNase H enzyme in the presence of catalytic amounts of ASO (1:4 equivalents ASO/mRNA). In a similar vein, the mRNA remained intact when the ASO-bound SNA was present but without the application of an AMF and was subsequently cleaved into two smaller RNA fragments (A and B) when the ASO-bound SNA was exposed to an AMF (30 mT, 103.4 kHz) for 90 min. The ASO was only released from the surface of the SNA in the presence of an AMF and prior to activation remained inactive and unable to perform its downstream function. **(B)** Schematic detailing the release mechanism, whereby localised heating at the surface of the nanoparticle, induced by magnetic hyperthermia, releases the ASO for downstream binding to its cognate mRNA. The formation of a DNA-RNA heteroduplex and recruitment of the endogenous RNase H enzyme causes the selective degradation of the RNA portion, downregulating the mRNA.

2.6. Conclusion

A dynamic delivery platform has been developed, which mimics the SNA architecture and harnesses the heat dissipated from magnetic hyperthermia (a deeply tissue-penetrative anticancer therapy) to release model DNA strands (in this case ASOs) and selectively control gene knockdown. Importantly, the on-demand downregulation of a model mRNA sequence (mRNA encoding the fluorescent protein mVenus) was achieved with a magnetic excitation frequency of ~100 kHz; this is compatible with the only clinically available magnetic hyperthermia system by MagForce, which was optimised to minimise eddy currents within the body and reduce patient discomfort [102]. In the future, the utilisation of click chemistry will allow for the easy replacement of the model ASO with any DNA sequence, with the potential to expand to other clinically relevant therapeutics such as mRNA. The promising "off" state and the ability to inhibit the therapeutic function of the bound ASO until activation at the target tissue (by way of AMF exposure) serves as a compelling proof-of-concept for the newly-developed controllable drug delivery platform that has the potential to enable high potency with fewer off-target effects from on-demand drug release.

3

Application of magnetically-activated spherical nucleic acids in the remote control of cell-free protein synthesis

3.1. Introduction

3.1.1. Applications of CFPS

In recent years CFPS systems have transitioned from a research tool, enabling the fundamental understanding of transcription and translation, to a powerful technological platform with the ability to meet the demands for efficient and scalable protein production [165]. Indeed, advancements in productivity, cost, and complexity of recombinant

(genetically-engineered) proteins synthesised from CFPS have aided their commercialisation [166]; CFPS systems have found use in the production of high-throughput protein libraries and personalised medicines amongst others [165].

CFPS allows for high-throughput protein production, for which its advantages over in-vivo expression systems are three-fold: the avoidance of time-intensive molecular cloning steps with linear polymerase chain reaction (PCR) templates [165]; the ability to synthesise with accelerated timelines [167]; and the emergence of miniaturisation with protein interactions studied on microchip devices [168]. However, limitations include batch to batch variability and instability of components stored overtime [169]. Isotope-labelled amino acids are easily incorporated in CFPS systems and enable the structural analysis of proteins by NMR and/or mass spectrometry, holding importance for structural biology and proteomics. The ability to efficiently incorporate isotope-labelled amino acids and express the translated proteins with high purity allows for NMR analysis without purification, proving fast and reliable [170,171]. In the way of high-throughput screening, CFPS has been applied to antibody discovery and has aided the detailed characterisation of the binding affinities associated with a library of monoclonal antibodies, which were developed to bind to SARS-CoV-2 with high affinity, in a process avoiding laborious in-vivo protein expression protocols [167,172]. These screening assays can be further scaled-up, and CFPS has been utilised to analyse the protein folding of up to 900,000 protein domains in one-week [173].

CFPS has also found application as a tool for personalised medicine and has been implemented in several human clinical trials, offering a rapid and adaptable platform for synthesising protein-based therapeutics [174]. In-particular, the synthesis of antibodies has been realised using CFPS, such as the immunoglobin G protein Trastuzumab, which is an approved adjuvant therapy for HER2-positive breast cancer [48,175]. Indeed, polypeptides (recombinant proteins and antibodies) constitute one of the fastest-growing classes of

therapeutics, accounting for 28% of all novel drugs approved by the EMA, FDA and/or United Kingdom Medicines and healthcare Products Regulatory Agency (MHRA) in 2024 [176]. Beyond antibody production, CFPS has also found application in vaccine development, including the rapid and on-demand production of fusion proteins for B-cell lymphoma vaccines [177] and the production of virus-like particles (VLPs) to design a VLP-antigen vaccine with increased stability and lower immunogenicity for hepatitis B [178]. CFPS has emerged as a rapid and economical strategy for vaccine production, offering high yields that are unattainable in traditional protein expression systems as a consequence of toxicity issues with living cells [177].

3.1.2. Regulation of CFPS with an external stimulus

The ability to control CFPS systems with an external stimulus would allow for the real-time regulation of pharmaceutically-active biomolecule production, opening up new avenues for targeting biosynthesis in-vivo, minimising systemic side effects, and/or modulating cellular behaviour [179]. To enable this additional level of functionality, the remote control of CFPS systems using an external stimulus such as small molecules, temperature and light has been widely explored. Relevant examples and their respective advantages and disadvantages are detailed in Section 1.3.3 and Section 1.4.

3.1.3. Chapter overview

An ideal stimulus for controlling CFPS is AMFs, which are deeply tissue-penetrating (>10 cm) and biologically benign [95,96]. As such, the aim of this chapter is to detail the modification of the magnetically-activated SNAs to enable their application in controlling CFPS of a model protein by way of harnessing the heat dissipated by superparamagnetic IONPs in an applied AMF. This development process described herein consisted of the following activities:

- SNA modification, replacing the conjugated dsDNA with the T7 promoter sequence.
- The synthesis and validation of an inactive DNA template (~1 kb) encoding the protein of interest.
- The application of the T7 promoter-bound magnetically-activated SNAs in controlling CFPS by way of activating the other otherwise inactive DNA template only in the presence of an applied AMF.

3.2. Modification of the SNAs

3.2.1. Modification of the T7 promoter sequence

In order to access new applications in modulating CFPS, the magnetically-activated SNAs were modified with dsDNA comprising the T7 promoter sequence. The T7 promoter sequence (23 base sequence) was designed to include five extra bases (GAAAT) at the 5′-end of the standard template sequence (18 base sequence) (Fig. 3.1A,B). This was to ensure an appropriate theoretical T_m of the annealed dsDNA T7 promoter, calculated as ~58 °C, providing a benchmark for the theoretical thermal energy required to break the hydrogen bonds in the double helix and release the T7 promoter “top” strand for controlling CFPS downstream.

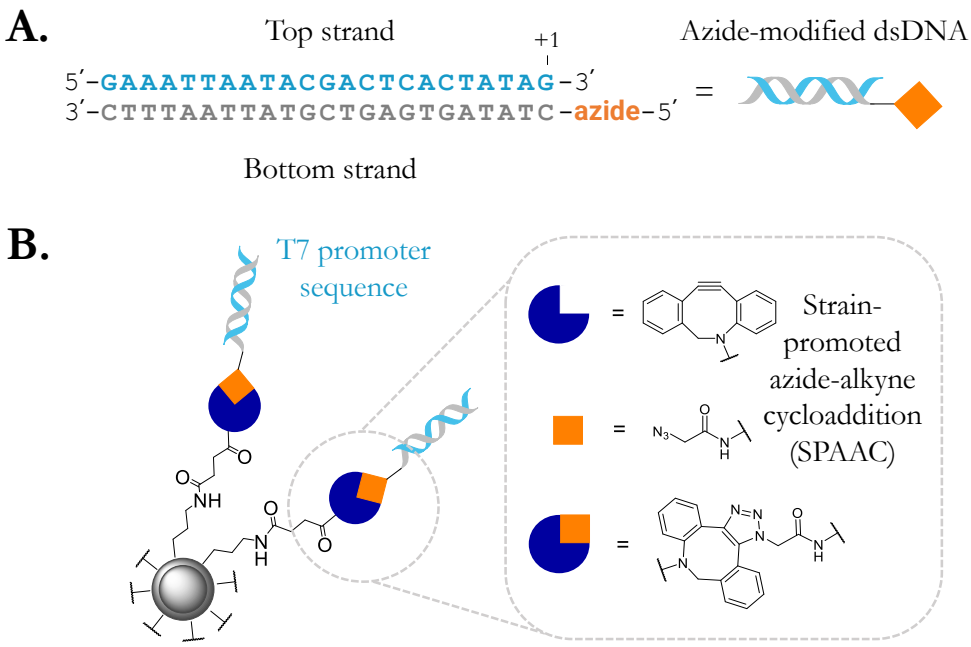

Fig. 3.1. Schematic of spherical nucleic acid synthesis with the T7 promoter. (A) Schematic showing the sequences of the "top" and "bottom" (azide-modified) T7 promoter strands. The transcription start site is labelled as +1. **(B)** Schematic detailing the conjugation of the dsDNA, comprising the "bottom" strand covalently bonded to the DBCO-modified silica shell through SPAAC and the "top" strand, in this case the T7 promoter sequence, hybridised on to synthesise the SNA.

The T7 promoter "bottom" strand was modified with an N_3 click-handle by reacting the pre-synthesised bifunctional 2-azidoacetic acid NHS ester with the commercially-available "bottom" strand, which had an active primary amine group at the 5′-end from the incorporation of a six-carbon amino linker. The resulting N_3-modified "bottom" strand was characterised by oligonucleotide mass spectrometry, which confirmed the successful NHS ester coupling with major peak (2) reflecting the expected molecular mass of 7305 Da (Fig. 3.2). The minor peak (1) is an impurity of the "bottom" T7 promoter strand with no active six-carbon amino linker. The DNA was not purified further as the impurity with no N_3 modification was not expected to interfere with the SPAAC or react with the DBCO-modified IONPs@SiO_2.

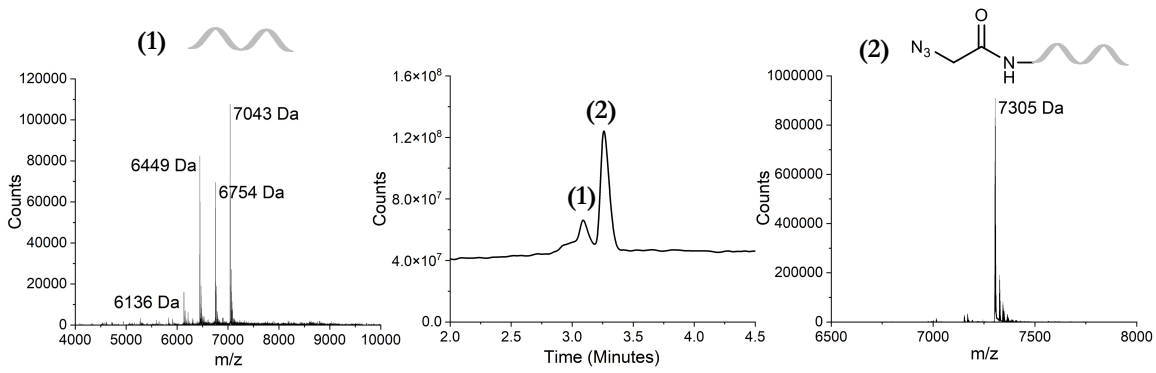

Fig. 3.2. Mass spectrometry data for azide-modified DNA T7 promoter. Oligonucleotide mass spectrometry of the azide-modified T7 promoter "bottom" strand, whereby the major peak (2) deconvolutes to give the expected mass of 7205 Da, indicating a successful terminal modification and the minor peak (1) corresponds to the "bottom" T7 promoter strand with no active six-carbon amino linker.

The N_3-modified "bottom" T7 promoter strand was annealed to the unmodified "top" T7 promoter strand in the same manner as Section 2.3.1 and analysed by PAGE (Fig. 3.3). The annealed dsDNA is of higher molecular mass than the individual "top" and "bottom" ssDNA T7 promoter strands and therefore the dsDNA travels a shorter distance through the 16% (v/v) PAGE gel in the direction of the electric current. The absence of bands associated with the free ssDNA and the presence of a single band in the final lane associated with the dsDNA indicates the success of the annealing reaction.

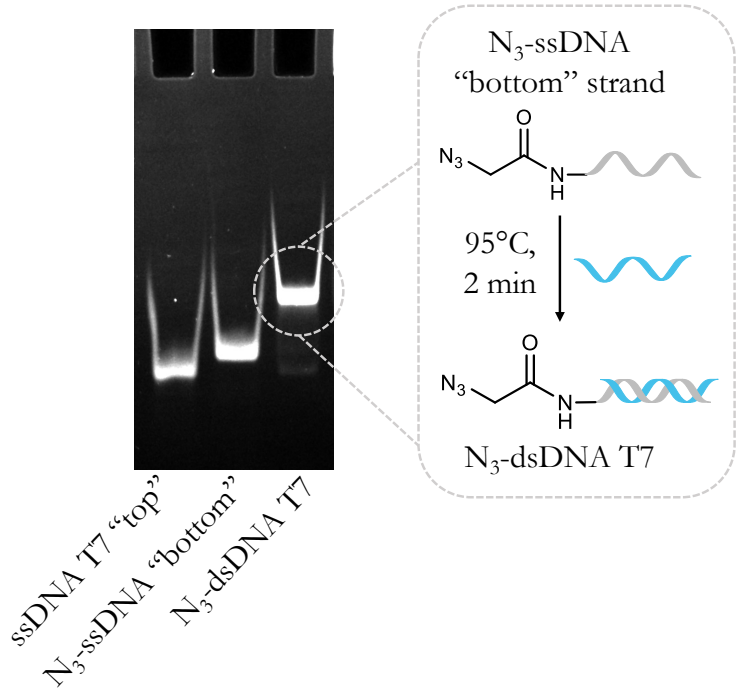

Fig. 3.3. Quantification of dsDNA T7 promoter formation. Native 16% (v/v) PAGE tracking the successful annealing of the T7 promoter "bottom" strand with (N_3-ssDNA "bottom") to the T7 promoter top strand (ssDNA T7 "top"), and the resulting dsDNA (N_3-dsDNA T7). The dsDNA is of higher molecular mass and so travels slower down the gel in the direction of the electric current (top to bottom of the gel).

3.2.2. Synthesis and characterisation of T7 promoter-bound SNAs

The SNA synthesis was carried out by reacting the N_3-modified dsDNA T7 promoter onto the surface of the DBCO-modified IONPs@SiO_2 by SPAAC. The dsDNA was frozen slowly (-7 °C for 4 h in an Optima LTC4R refrigerated bath, *Grant* Instruments, and then -20 °C in the freezer overnight) in the presence of DBCO-modified IONPs@SiO_2 and low concentrations of salt, before thawing at 4 °C for 1 h [156]. The resulting T7 promoter-bound SNAs were purified with the newly-developed agarose purification (detailed in Section 2.4.2) and characterised in-part by DLS. Indeed, the decrease in hydrodynamic diameter to D_{DLS} = 125.3 nm upon SNA formation, as compared with D_{DLS} = 142.0 nm for DBCO-modified IONPs@SiO_2, is indicative of the newly-formed colloid, stabilised by DNA-to-DNA electrostatic repulsion (Table 5). The shift in ζ-potential to a highly negative

value, decreasing to ζ = -36.6 mV from ζ = -13.9 mV for DBCO-modified IONPs@SiO_2, indicates further the presence of the phosphate DNA backbone (Table 5).

Table 5. dsDNA-modified IONPs@SiO_2 (T7 promoter-bound SNA) characterisation. Summary of the hydrodynamic diameter (analysis in number), PDI and ζ-potential, as determined by DLS with the mean calculated from n = 3 repeat measurements.

Nanoparticle	Hydrodynamic diameter (nm)	PDI	ζ-potential (mV)
T7 promoter-bound SNA	125.3	0.38	-36.6

The T7 promoter loading was determined by denaturing the dsDNA attached to the IONPs@SiO_2 at 95 °C for 5 min in urea-containing dye and comparing the amount of released DNA to a calibration curve of known concentration on a 1.5% (w/v) agarose gel (Fig. 3.4). In a similar vein to calculating the number of DBCO molecules loaded onto a single nanoparticle (detailed in Section 2.2.2 and in accordance with previous literature [150–153]), the concentration of attached T7 promoter strands was related to the calculated nanoparticle concentration in units of particles·ml^{-1} to give an estimated loading of 18 dsDNA per nanoparticle, which is in-line with literature values for SNAs comprising dsDNA[156].

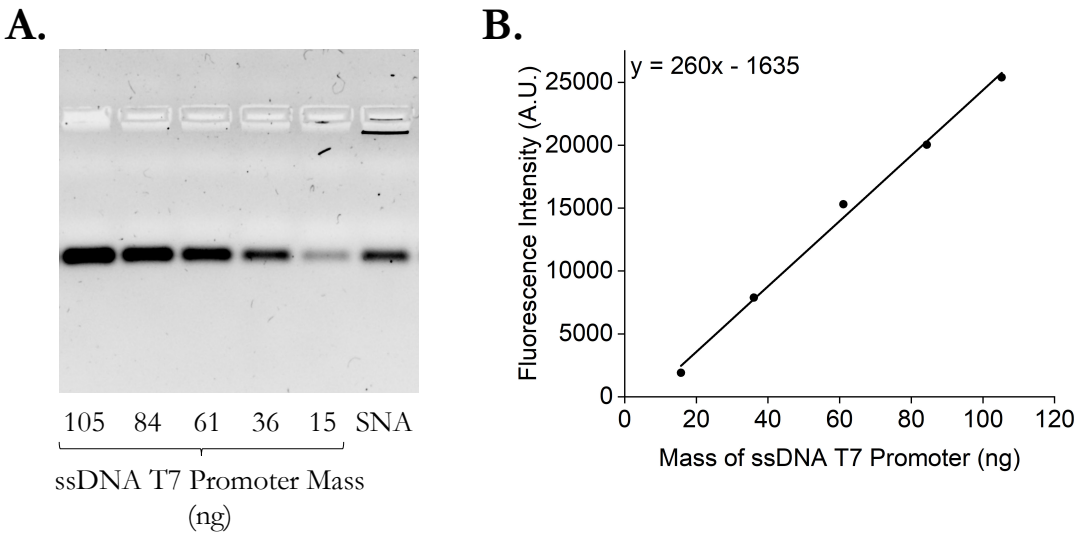

Fig. 3.4. Calibration curve to determine SNA T7 promoter loading. (A) 1.5% (w/v) agarose gel of known masses of the free T7 promoter and a known volume of SNA heated at 95 °C in urea-containing dye to release the bound T7 promoter. Due to SNA volume/concentration constraints, the data is indicative of n = 1 biological repeats. **(B)** Calibration curve of the nucleic acid stain GelRed® fluorescence intensities (determined by ImageJ software) against the known T7 promoter mass, the linear regression (fitted in Origin) was used to extrapolate the concentration of bound T7 promoter strands on the individual SNA particles.

3.2.3. Quantification of the effectiveness of the SNA purification

The concentration of the residual electrostatically-bound dsDNA before and after the newly-developed agarose purification was determined by incubating the SNAs in a native loading dye and comparing the amount of dsDNA pulled-off the SNAs with a calibration curve of known concentration on a 1.5% (w/v) agarose gel (Fig. 3.5). The concentration of electrostatically-bound dsDNA pulled-off the surface of the SNAs, travelling through the agarose gel on account of the applied electric current, decreased by a factor of ~10 after agarose purification from a concentration of 0.85 μM before purification to a concentration of 0.07 μM after purification.

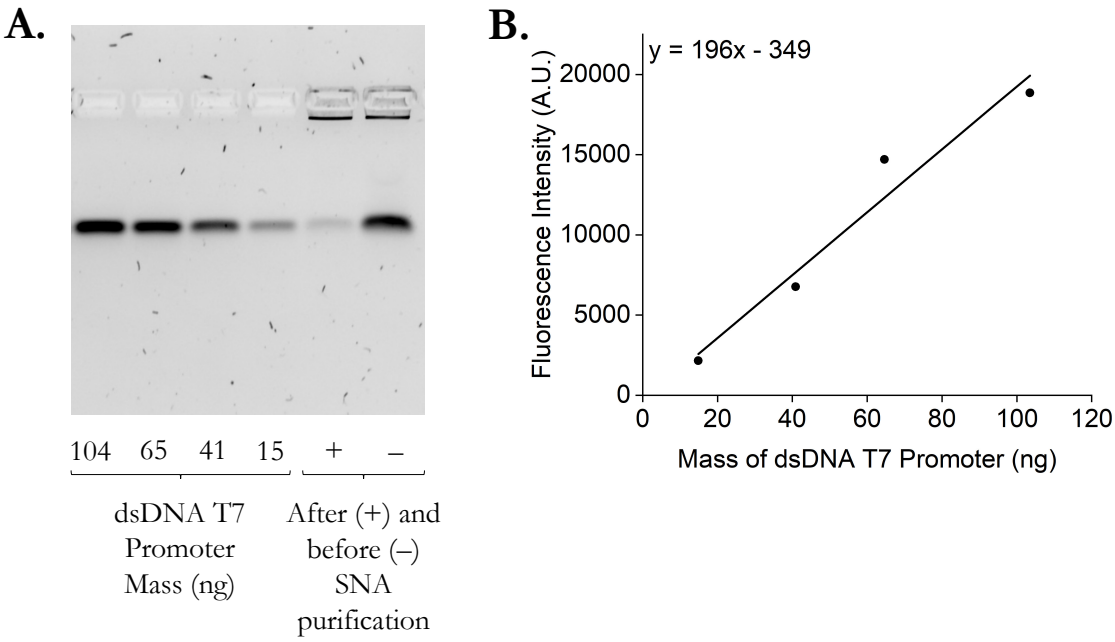

Fig. 3.5. Calibration curve to determine effectiveness of agarose purification. (A) 1.5% (w/v) agarose gel of known concentrations of the dsDNA T7 promoter sequence and a known volume of SNA before and after agarose purification. Due to SNA volume/concentration constraints, the data is indicative of n = 1 biological repeats. **(B)** Calibration curve of the nucleic acid stain GelRed® fluorescence intensities (determined by ImageJ software) against the known dsDNA T7 promoter mass, the linear regression (fitted in Origin) was used to extrapolate the concentration of dsDNA T7 promoter electrostatically-bound to the surface of the SNAs before and after agarose purification.

The effect of agarose purification and the "off" state of the T7 promoter-bound SNAs in the absence of a magnetic field was determined using an in-vitro transcription (IVT) assay. The assay takes advantage of the short RNA aptamer, Broccoli, and the fluorescence of (*Z*)-4-(3,5-difluoro-4-hydroxybenzylidene)-1,2-dimethyl-1*H*-imidazol-5(4*H*)-one (DFHBI) upon binding and RNA-fluorophore complex formation [180]. The inactive DNA template encoding Broccoli was synthesised by annealing together the template strand and coding strand (synthesised by Integrated DNA Technologies), whereby the T7 promoter region was absent in the coding strand forcing a ssDNA 3′-overhang. This modification took advantage of the T7 RNA polymerase only transcribing from an intact dsDNA T7 promoter sequence and possessing the ability to traverse discontinuities in the coding strand [181,182]. In the

presence of the Broccoli template with the dsDNA T7 promoter region present (full template), RNA expression was recovered as inferred by the increase in fluorescence intensity of the DFHBI upon RNA binding (47,042 A.U.) (Fig. 3.6). This is compared with the inactive template with the T7 promoter region missing in the coding strand, whereby minimal fluorescence intensity (1374 A.U.) was observed. Furthermore, the RNA expression was not perturbed by the addition of NH_2-modified IONPs@SiO_2 with a retention of fluorescence intensity from the RNA-DFHBI complex (40,078 A.U.). The tight "off" state with a lack of T7 promoter strands de-hybridising from the surface of the SNAs in the absence of the magnetic field (thereby preventing the completion of the dsDNA T7 promoter region and activation of the inactive DNA template encoding Broccoli) was only achieved after agarose purification of the SNAs. It was inferred by the fluorescence intensity of DFHBI as a result of the recovery of RNA expression and RNA-DFHBI complex formation averaging six-times higher before agarose purification (11,442 A.U.) compared with after agarose purification (2084 A.U.) and in the absence of an AMF. It was hypothesised that the discrepancy between the inactive DNA template and the "off" state of the SNA in the absence of an AMF and after agarose purification was due to the small amount of electrostatically-bound dsDNA T7 promoter remaining on the SNAs after agarose purification (Fig. 3.4).

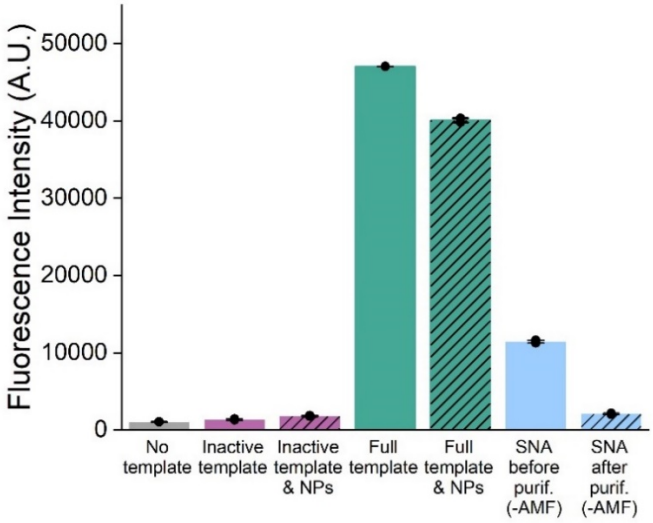

Fig. 3.6. Effect of SNA purification by agarose gel and presence of nanoparticles in RNA expression. IVT of the Broccoli RNA aptamer that after expression binds to the small molecule DFHBI and fluoresces. RNA expression was recovered with the full Broccoli template compared with the inactive Broccoli template (with the dsDNA T7 promoter missing from the coding strand) and the RNA expression and fluorescence intensity was not perturbed by the addition of NH_2-modified IONPs@SiO_2. The tight "off" state of the SNA (-AMF), comparable with the inactive template (negative control), was only achieved after agarose purification of the SNAs. Data is presented as mean values ± the standard deviation over n = 8 technical replicates.

3.3. Synthesis and validation of the inactive DNA template

3.3.1. Synthesis of the inactive DNA template

A method was developed to enable the synthesis and thus expression of longer inactive DNA templates (~1 kb), such as that encoding the fluorescent protein mNeonGreen (mNG), in-turn opening up the possibility of controlling the production of proteins with magnetic hyperthermia. The method involved synthesising the template strand with a ssDNA 3′-overhang (of the "bottom" T7 promoter sequence) and the coding strand with the T7 promoter sequence missing, again taking advantage of the T7 RNA polymerase only transcribing from a dsDNA T7 promoter [181,182]. The design of the inactive DNA template was to ensure that the T7 promoter strand released with magnetic hyperthermia was able to

hybridise to the complimentary 3′-overhang on the template strand and restore the dsDNA T7 promoter region, enabling the T7 RNA polymerase to bind and activate CFPS. To achieve this, two DNA templates encoding mNG were synthesised by PCR, one with and one without the dsDNA T7 promoter region, and then lambda exonuclease was exploited to convert linear dsDNA to ssDNA by degrading in the 5′ to 3′ direction (Fig. 3.7A). The enzyme has preferred activity on 5′-phosphorylated ends with non-phosphorylated strands degraded at a reduced rate. This was taken advantage of and a 5′-phosphorylated primer was used for the coding strand of the DNA template with the dsDNA T7 promoter region present and the template strand of the DNA template with the dsDNA T7 promoter region missing. This enabled the digestion of the individual phosphorylated strands by lambda exonuclease, whereby the timeframe of exonuclease treatment was optimised (30 min for the mNG template without the dsDNA T7 promoter and 35 min for the template with the dsDNA T7 promoter) to ensure only the phosphorylated strand was removed, leaving the desired ssDNA intact. The intact coding strand with the T7 promoter region missing and the intact template strand with the T7 promoter region present were then annealed together to synthesise the inactive DNA template encoding mNG. The synthesis of the inactive DNA template was quantified by 1.5% (w/v) agarose gel electrophoresis and compared with a 1 kb DNA ladder (NEB) (Fig. 3.7B).

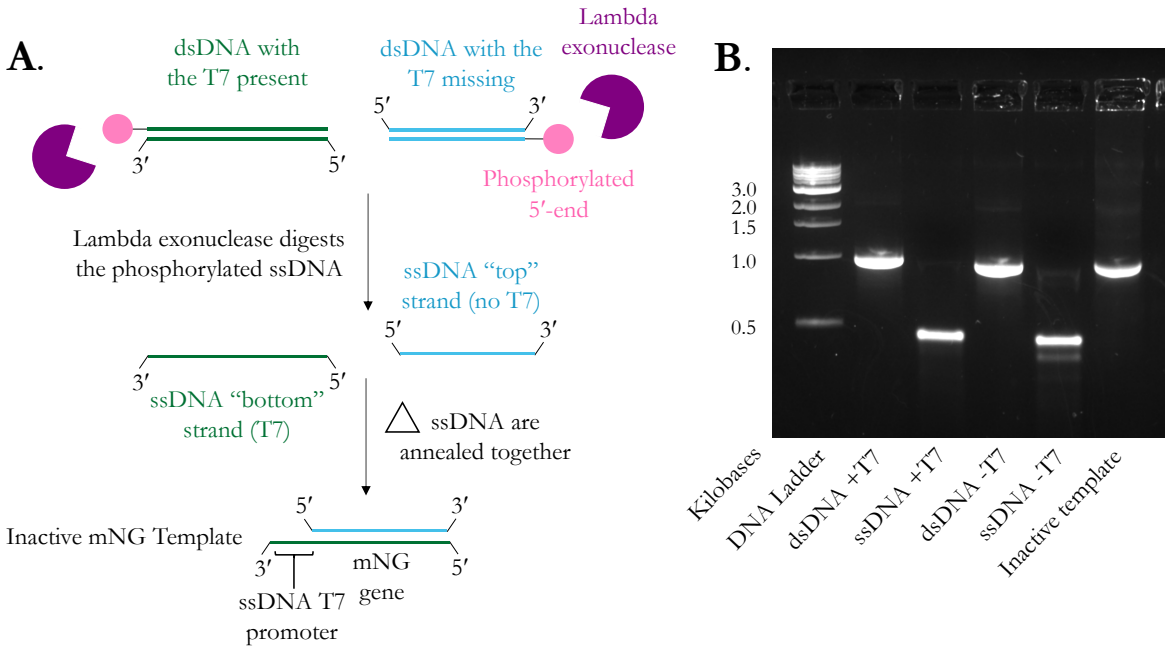

Fig. 3.7. Synthesis of the inactive mNG template. (A) Schematic showing the synthesis of dsDNA with and without the T7 promoter present and using 5′-phosphorylated primers to enable the subsequent digestion of the phosphorylated strands by lambda exonuclease prior to annealing the resulting ssDNA to create the inactive mNG template. Note: promoter (23 base pairs) and gene (~700 base pairs) length are not to scale. **(B)** Native 1.5% (w/v) agarose gel quantifying the synthesis of the inactive template with the dsDNA with (dsDNA +T7) and without (dsDNA -T7) the T7 promoter region present, its digestion to the ssDNA "bottom" strand with the T7 promoter present (ssDNA +T7) and the ssDNA "top" strand without the T7 promoter (ssDNA -T7) present, prior to the formation of the inactive template (inactive template).

3.3.2. CFPS and activation of the inactive DNA template

The loss of activity of the inactive DNA template encoding mNG was validated using the commercial CFPS system (PURExpress) that contains the molecular machinery (including the T7 RNA polymerase) required for protein expression. The fluorescence intensity was measured after 3 h of incubation to determine the levels of expressed mNG protein. The inactive DNA template alone had 6% activity compared with the expression of the full template containing the intact dsDNA T7 promoter region (Fig. 3.8). In contrast, the absence of a DNA template gave 2% activity compared with the full template. The influence of the IONPs@SiO_2 was explored, whereby the activity of PURExpress was not perturbed by the

addition of the nanoparticles with a retention of fluorescence intensity associated with mNG expression from the full template containing the intact dsDNA T7 promoter region.

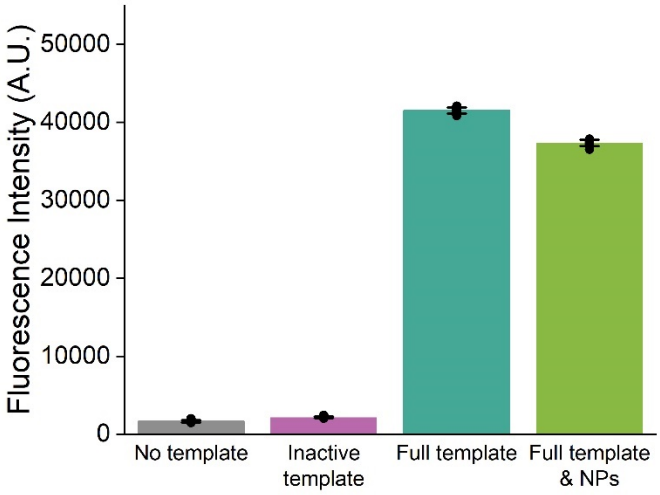

Fig. 3.8. Validation of the inactive DNA template and effect of magnetic nanoparticles. CFPS of mNG in the presence of NH_2-modified IONPs@SiO_2, showing negligible inhibition of mNG expression and fluorescence intensity compared with the full mNG template (dsDNA T7 promoter region present) without the nanoparticles present. Data is presented as mean values ± the standard deviation over n = 8 technical replicates.

After the bulk CFPS reactions containing the dsDNA T7 promoter region were incubated for 3 h, serial dilutions of these bulk CFPS reactions determined that the respective fluorescence intensity decreases linearly with concentration (Fig. 3.9).

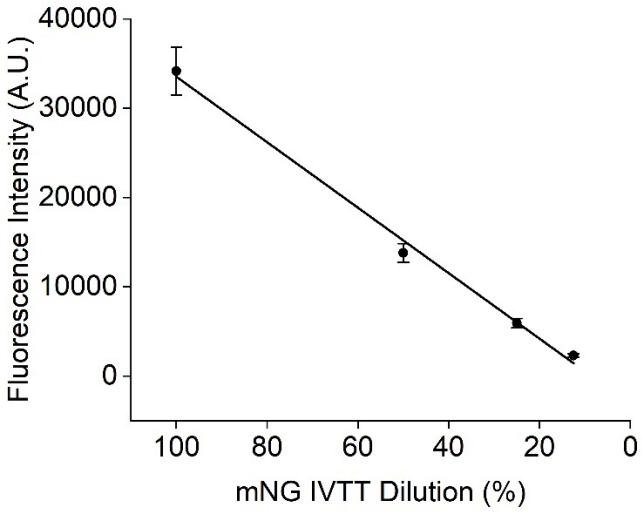

Fig. 3.9. Serial dilutions of bulk CFPS. Serial dilutions of bulk CFPS, whereby a linear relationship is observed between fluorescence intensity of the mNG protein synthesised and the concentration of the bulk CFPS, diluted with the outer buffer. Data is presented as mean values ± the standard deviation over n = 9 technical replicates.

3.4. Magnetic activation of cell-free protein synthesis

3.4.1. Application of magnetically-activated SNAs for the control of CFPS

The inactive DNA template was combined with the T7 promoter-bound SNAs (newly-synthesised magnetically-activated SNAs) and their ability to control CFPS with an applied AMF was investigated. The inductive heating as a result of magnetic hyperthermia was hypothesised to denature the covalently-bound dsDNA and release the hybridised ssDNA T7 promoter "top" strand from the surface of the nanoparticles. The ssDNA T7 promoter "top" strand would now be free to hybridise to the inactive DNA template encoding mNG, restoring the dsDNA T7 promoter region. The T7 RNA polymerase (in the PURExpress) would then be able to recognise the dsDNA T7 promoter region and activate CFPS of the encoded fluorescent mNG protein (Fig. 3.10).

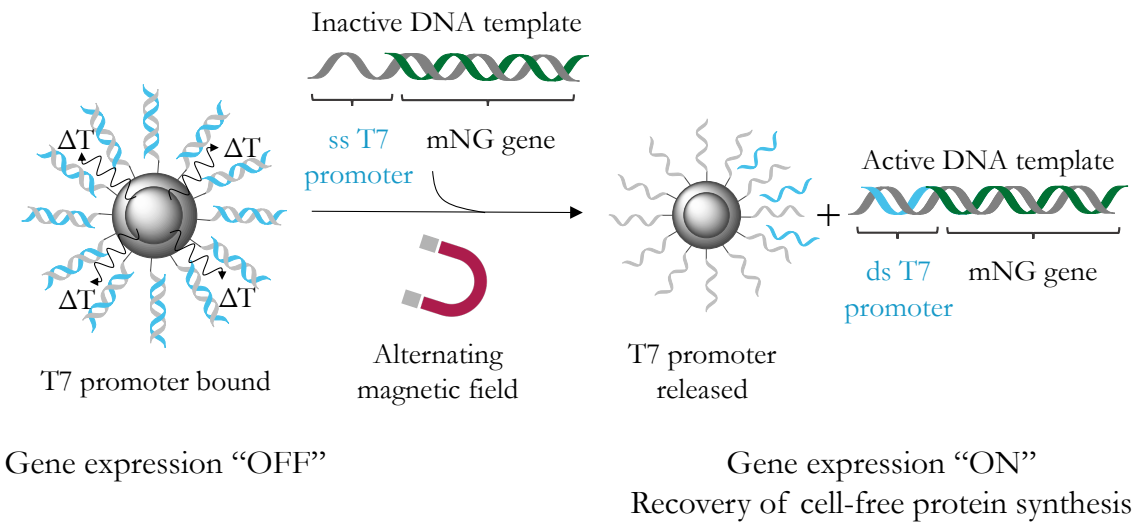

Fig. 3.10. Schematic detailing the mechanism behind controlling CFPS with magnetic hyperthermia and magnetically-activated SNAs. Schematic detailing the release of the hybridised ssDNA T7 promoter top sequence from the surface of the SNA as a result of inductive heating due to exposure to an applied AMF, and the subsequent hybridisation to the complimentary ssDNA T7 promoter on the template strand of the inactive template, restoring the dsDNA T7 promoter region and activating expression of the encoded fluorescent mNG protein. Note: promoter (23 bp) and gene (~700 bp) length are not to scale.

The AMF parameters optimised in Section 2.5, a magnetic field strength of 30 mT and a frequency of 103.4 kHz, were generated using the NAN201003 Magnetherm (Nanotherics Ltd) with an 18-turn coil of 50 mm internal diameter. The magnetic field-frequency product was maintained below the $H \times f = 5 \times 10^9$ A·m^{-1}·s^{-1} safety limit [118] at $H \times f = 2.47 \times 10^9$ A·m^{-1}·s^{-1}. The frequency was further compatible with the only clinically-available magnetic hyperthermia system (MagForce), which operates at a frequency of 100 kHz in order to minimise eddy currents within the body and reduce patient discomfort [102]. The timeframe of the applied AMF was mediated to ensure that the solution did not experience heating that was incompatible with PURExpress. The temperature of the bulk CFPS in the presence of the magnetically-activated SNAs was measured by submerging a fibre optic probe into the bulk solution, which was suspended inside the solenoid coil (Fig. 3.11). The timeframe was set at 25 min AMF exposure, peaking at a global temperature

of 39 °C, which is in the mild hyperthermia regime optimised to increase perfusion, improve blood flow and activate an immune response [100].

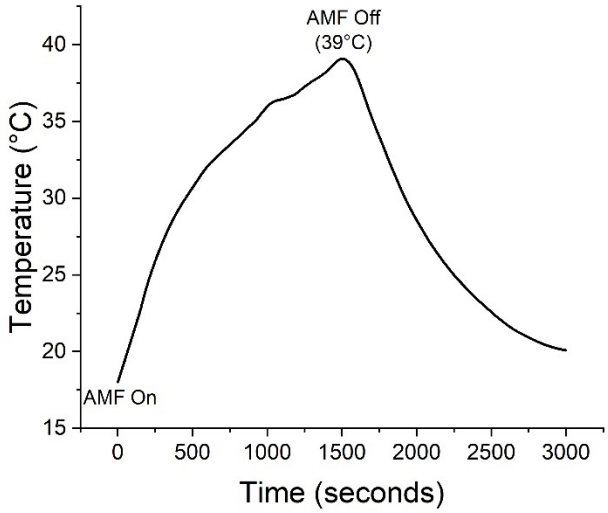

Fig. 3.11. Fibre optic probe data for the global heating experienced by bulk CFPS reactions in the applied AMF. Fibre optic probe data from the probe being submerged in the bulk CFPS solution and in the presence of magnetically-activated SNAs, inside the solenoid coil and exposure to an AMF for 25 min.

The magnetically-activated SNAs, inactive DNA template encoding mNG, and CFPS system (PURExpress) were exposed to an AMF (30 mT, 103.4 kHz) for 25 min, with a control experiment in the absence of an applied AMF. The expression of mNG was investigated by measuring the fluorescence intensity after a further incubation for 3 h, comparing the fluorescence to that of the inactive template alone (denoted the negative control) and the full template with the dsDNA T7 promoter region intact (denoted the positive control). The full template represented a theoretical 100% restoration of activity. A minor increase in fluorescence was observed in the control experiment (magnetically-activated SNAs, inactive DNA template, absence of an applied AMF) as compared with the negative control (solely the inactive DNA template) with a significant p-value of 0.016 (one-tailed and paired t-test) (Fig. 3.12). The significant p-value is likely due to the small amount

of electrostatically-bound dsDNA T7 promoter remaining on the SNAs after agarose purification (Fig. 3.4). The exposure of the magnetically-activated SNAs to an AMF (magnetic field strength of 30 mT and frequency of 103.4 kHz) for 25 min in the presence of the inactive DNA template and PURExpress resulted in the full recovery of mNG expression as compared with the positive control (full template with the dsDNA T7 promoter region intact) with a non-significant p-value of 0.30 (one-tailed and paired t-test). This regulation of biosynthesis in-situ and ability to activate gene expression in a selective manner was only achieved in the presence of the applied AMF.

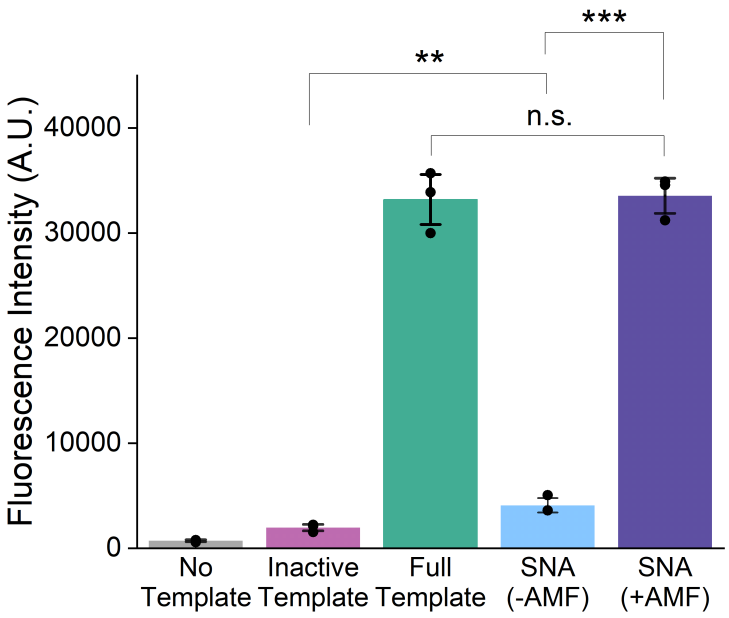

Fig. 3.12. Magnetic activation of CFPS. CFPS of mNG in the presence of magnetically-activated SNAs, with and without exposure to an applied AMF. Experiments that were not exposed to an AMF expressed minimal mNG, and their fluorescence intensity was comparable with the inactive DNA template only. Reactions exposed to an AMF expressed mNG and their fluorescence was consistent with reactions containing the full mNG template (dsDNA T7 promoter region present). Represents n = 3 biological replicates. Data is presented as mean values with error bars representing the standard deviation, *** represents $p < 0.002$ ($p = 0.0016$), ** represents $p < 0.02$ ($p = 0.016$), and n.s. represents p values that are not significant ($p = 0.30$) from one-tailed t-tests.

3.4.2. Control experiments to determine the role of magnetic hyperthermia

To be assured that the release of the hybridised ssDNA T7 promoter from the surface of the SNA was due to inductive heating rather than the increase in the temperature of the bulk solution, control CFPS reactions were carried out with the inactive DNA template and in the presence of the short dsDNA T7 promoter sequence, but without any IONPs@SiO_2 present. There was no observed positive trend after exposing the dsDNA T7 promoter with an applied AMF (30 mT, 103.4 kHz) for 25 min. This was inferred by the mNG expression and resulting fluorescence intensity of the CFPS reaction with the dsDNA and the applied AMF being within error (as measured by the standard deviation) at 8350 ± 1270 A.U. compared with the CFPS reaction with the dsDNA but without any applied AMF at 10,440 ± 829 A.U., and both markedly lower than the full template at a fluorescence intensity of 35,650 ± 3564 A.U. (Fig. 3.13). This highlighted that the unwinding of the dsDNA T7 promoter at the surface of the SNAs is a direct result of inductive heating from magnetic hyperthermia and not simply the heat generated from the solenoid coil.

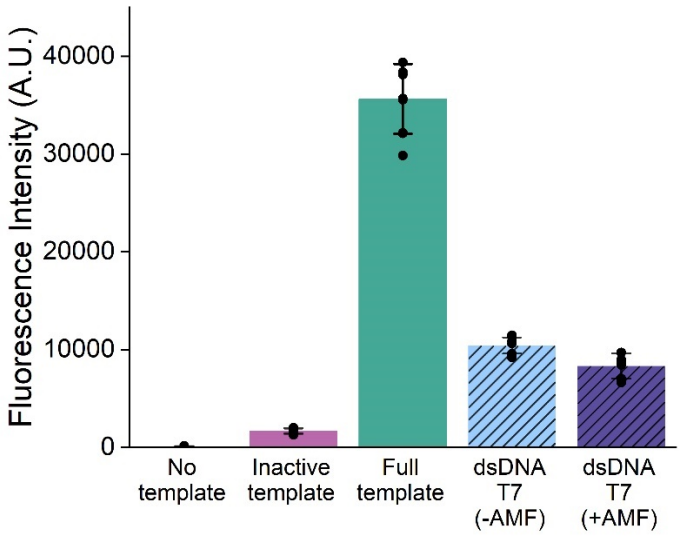

Fig. 3.13. Control CFPS reaction in the absence of magnetic nanoparticles. CFPS of mNG in the presence of dsDNA T7 promoter that was free in-solution with and without an applied AMF. Data is presented as mean values ± the standard deviation over n = 9 technical replicates.

To expand on these control experiments, the CFPS reactions in the presence of the short dsDNA T7 promoter sequence were carried out further with IONPs@SiO_2. In this case, the dsDNA T7 promoter was not connected to the IONPs@SiO_2 and instead was free in-solution. A minor increase in the fluorescence intensity (4453 A.U.) and mNG expression was observed for the CFPS reaction containing the free dsDNA T7 promoter and exposure to an applied AMF 30 mT, 103.4 kHz) for 25 min as compared with the identical CFPS reaction but in the absence of an applied AMF (2219 A.U.) (Fig. 3.14). The minor increase was hypothesised to be a result of dsDNA electrostatically-binding to the surface of the hydrophobic DBCO-modified IONPs@SiO_2, enabling the dsDNA to benefit from some of the localised heating in the applied AMF. Again, both of the fluorescence intensity values were much lower than that observed with the full template (39,659 A.U.). This control experiment demonstrates further the necessity of tethering of the dsDNA T7 promoter to the surface of the nanoparticles, ensuring that the dsDNA is in close proximity to maximise the

localised heating experienced by the dsDNA on account of the heat generated by the IONPs and to influence the extent of T7 promoter release for CFPS downstream.

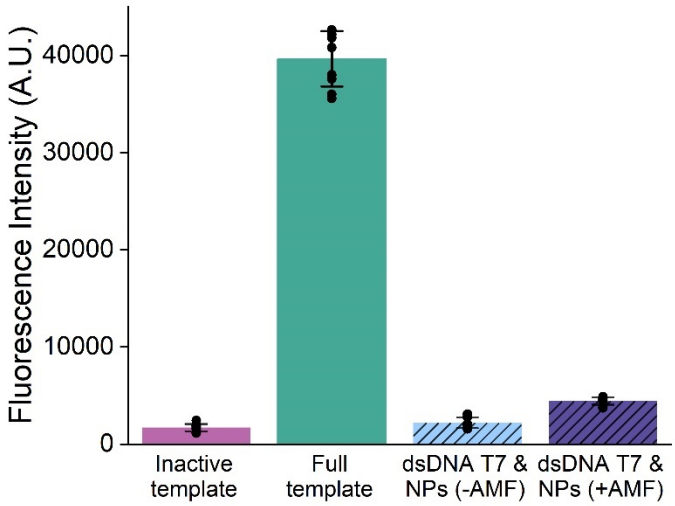

Fig. 3.14. Control CFPS reaction in the presence of magnetic nanoparticles. CFPS of mNG in the presence of dsDNA T7 promoter and DBCO-modified IONPs@SiO_2 that was free in-solution with and without an applied AMF. Data is presented as mean values ± the standard deviation over n = 9 technical replicates.

3.5. Conclusion

The reach of the technology has been expanded to include controlling CFPS using magnetic hyperthermia (a tissue-penetrating and clinically-approved anticancer therapy). This was achieved by modifying the magnetically-activated SNAs with the T7 promoter sequence and synthesising an inactive DNA template encoding the fluorescent protein mNG. The inactive DNA template comprised a ssDNA 3′-overhang (of the "bottom" T7 promoter sequence) and a coding strand with the T7 promoter sequence missing. This design took advantage of the T7 RNA polymerase only transcribing from a dsDNA T7 promoter and allowed for the released ssDNA T7 promoter "top" strand in an applied AMF to hybridise to the inactive DNA template encoding mNG [181,182]. The restoration of the dsDNA T7 promoter region as

a result of magnetic hyperthermia enabled the T7 RNA polymerase (in the PURExpress) to recognise the dsDNA T7 promoter region, activating CFPS of the encoded protein. Critically, the promising "off" state, showing negligible protein expression in the absence of the magnetic field, was only achieved with the newly-developed SNA purification technique. The magnetic field strength and frequency of the applied AMF were within the tolerable limit, set to minimise patient discomfort, and the magnetic excitation frequency of ~100 kHz is compatible with the only clinically available magnetic hyperthermia system by MagForce [102]. The ability to control CFPS with magnetic hyperthermia paves the way for real-time regulation of pharmaceutically-active biomolecule production, opening up new avenues for controlling biosynthesis.

4

Application of magnetically-activated spherical nucleic acids in the remote control of synthetic cells

4.1. Introduction

4.1.1. Applications of synthetic cells

The compartmentalisation of CFPS systems within lipid bilayers in order to construct synthetic cells represents a promising platform for controlling protein production, with applications in biotechnology and personalised medicine [69,179]. The size of synthetic cells are aligned with large liposomes, having comparable dimensions (diameters above 1 μm)

and curvature with eukaryotic cells [49]. However, synthetic cells offer greater complexity in design than liposomes, with complete programmability of biological functions and without the risk of uncontrolled replication (a drawback of living systems) [69]. Similarly to liposomes, the lipid membrane of synthetic cells can be functionalised with targeting ligands [183] to increase the concentration of synthetic cells at the therapeutic site of interest (localisation), and with stealth polymers [69–71] to improve circulation time in-vivo (stability) (Fig. 4.1). Life-like capabilities can also be incorporated, for example sense-and-respond behaviour and gene expression.

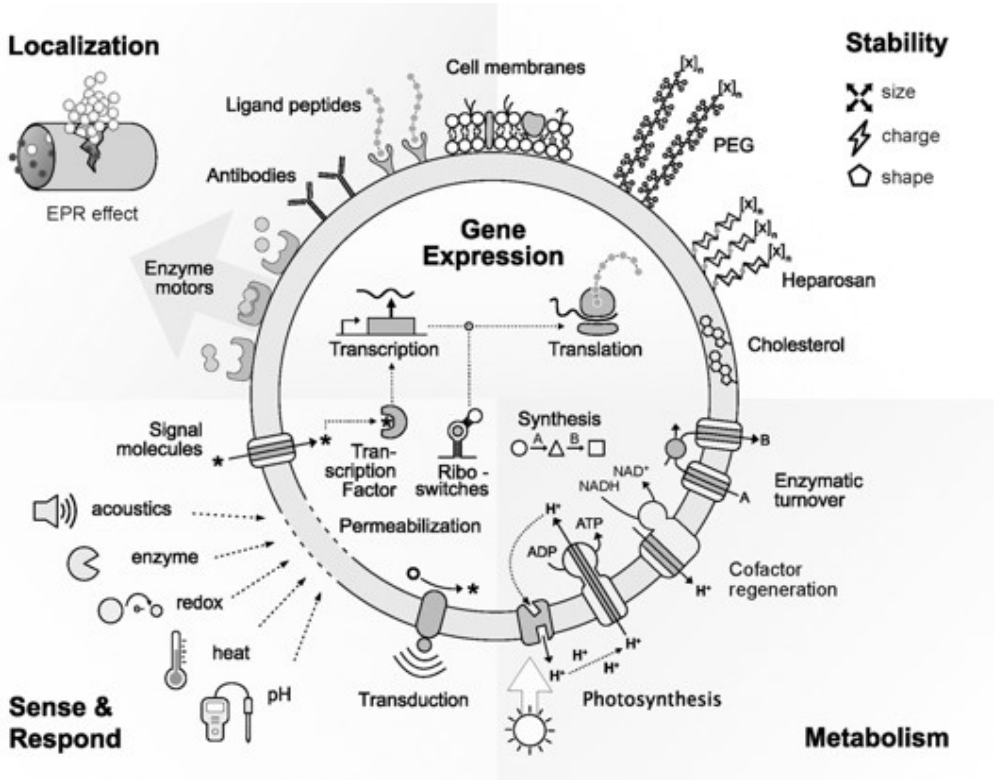

Fig. 4.1. Life-like capabilities of synthetic cells. Synthetic cells are minimal compartments that are capable of life-like behaviours as a result of an encapsulated CFPS system and DNA templates encoding a specific function. As such synthetic cells can impart sense and respond, metabolic, and gene-expressing capabilities. Beyond this, surface modification of the lipid membrane enables the incorporation of cell-targeting groups for localisation and stealth polymers for stability. Figure reproduced from "Synthetic cells in biomedical applications" by Sato et al.[69] (© 2021) under the license number 6058660464963 (John Wiley and Sons).

4.1.1.1 Sense-and-respond behaviour

The ability to incorporate "smart" sensing capabilities enables more precise delivery, releasing the pharmaceutically-active compound only at the therapeutic site of interest. As such, a range of stimuli-sensitive molecules have been incorporated into the membrane of synthetic cells to modulate phase transitions as a result of fluctuations in temperature [184,185], light[186–190], and magnetic fields [112,113]. Temperature-sensitive phospholipids and/or polymers are ubiquitous in stimuli-responsive membrane designs; they are engineered to have an amenable phase transition temperature that enables grain boundary defects to form at elevated temperatures, allowing for transport of the cargo across the membrane [112–114,184,185]. This mechanism has been exploited to release two model anti-cancer agents (tamoxifen and imatinib) at a mild hyperthermia temperature of 39.4 °C, inhibiting the growth of breast cancer cells [184]. The release of cargo at mild hyperthermia, in-particular under conditions mimicking a tumour microenvironment of 42 °C, has been used to release doxorubicin via aggregation of the polymer chains due to the disruption of hydrogen bonds, thereby increasing membrane perforation [185].

Light has been exploited to influence the release of cargo from synthetic cells, probing future application in chemophototherapy [93]. The incorporation of NIR active molecules into the lipid membrane has been used to promote membrane destabilisation and permeabilisation by way of mechanisms including: light-induced oxidation of unsaturated lipids by singlet oxygen species, releasing model cargo through the formation of membrane pores [186–188]; photo-crosslinking of unsaturated bonds in the bilayer, influencing conformational changes and membrane permeability [189]; photoisomerisation of molecules such as azobenzenes, inducing a conformational change from trans to cis isomers and bilayer disruption [190]. Indeed, light-induced oxidation and photo-crosslinking mechanisms have been applied in-

vivo with laser irradiation in the NIR regime, proving biocompatible [188,189]. NIR light is more suitable for penetrating bodily tissue (up to 5 mm for NIR ≅ 750 nm) than the commonly explored UVA light, which is more strongly attenuated by bodily tissue (by <1 mm) [92,93].

Magnetic hyperthermia has similarly been employed to modulate the phase transitions of temperature-sensitive phospholipids and rupture lipid bilayers to release pharmaceutically-active compounds by incorporating superparamagnetic nanoparticles as heating mediators in applied AMFs [112,113]. A compelling example by Theodosiou *et al.* encapsulated iron oxide nanoflowers, known to exhibit superior heating properties as a result of morphology and anisotropy factors [98], to modulate the release of an encapsulated cargo in lung cancer cells by inducing temperature increases that in-turn influenced the gel-to-liquid transition of the lipid bilayer at a temperature of 41.4 °C [113]. However, a reoccurring issue remains with the use of a magnetic excitation frequency (f = 395 kHz for Theodosiou *et al.* [113]) that is incompatible with the only clinically-approved magnetic hyperthermia generator by MagForce, operating at 100 kHz, and a magnetic field-frequency product ($H \times f = 7 \times 10^9$ A·m^{-1}·s^{-1} for Theodosiou *et al.* [113]) that exceeds the safety limits proposed by Hergt *et al* [118] *(*$H \times f = 5 \times 10^9$ A·m^{-1}·s^{-1}).

4.1.1.2. Gene-expressing capabilities

The “smart” capabilities of synthetic cells can be advanced by incorporating CFPS systems, opening up the possibility of controlling in-situ gene expression. The encapsulation of CFPS systems offers key advantages in their integration into “smart” drug delivery devices including: protecting the CFPS system and cargo from the external environment; preventing unwanted physiological responses such as anaphylaxis from the burst release of the cargo; concentrating the cargo in the interior, further enabling biochemical reactions and/or the

delivery of the cargo in high concentration at the therapeutic site of interest [69]. Indeed, the ability to encapsulate a CFPS system and produce proteins inside synthetic cells has been realised in-vivo, proving non-immunogenic and stable [72,73,75].

The added functionality of modulating CFPS and gene expression in the presence of an external stimulus and within synthetic cells has the potential to impact targeted drug delivery by catalysing the biosynthesis and/or release of therapeutically-active biomolecules only at the therapeutic site of interest. Notable examples are described in Section 1.4 including: modulating CFPS on sensing small molecules (such as cancer metabolites) with riboswitches, limited by cell permeability or failure of activation as a result of changes in disease physiochemistry [77–79,191]; modulating CFPS with elevated temperature and RNA thermometers, limited by off-target effects due to multiple disease states (infections, inflammatory diseases, cancers) being associated with mild hyperthermia [50,192]; modulating CFPS with UVA light, limited by cytotoxicity risks and inability of UVA light to penetrate bodily tissue by <1 mm [52,91,92].

The application of magnetic hyperthermia in the rupturing of lipid bilayers has been investigated for releasing small molecules from embedded liposomes of a diameter of 200 nm into larger vesicles that contain an enzyme to mediate catalysis and production of a new compound [114]. However, the AMF parameters ($H \times f = 1 \times 10^{10}$ A·m^{-1}·s^{-1} for Zhu *et al.* [114]) exceed the proposed safety limit [118]. In light of this, there is scope to develop a drug delivery platform based on gene-expressing synthetic cells that respond to magnetic hyperthermia, generated by exposure to AMFs within clinically-relevant magnetic field strengths and frequencies.

4.1.2. Chapter overview

In order to aid the translation of synthetic cells as drug delivery devices, there is a need to control their activity using AMFs that fall within clinically-relevant magnetic field strength and frequencies. The development of a platform that harnesses the heat dissipated from magnetic hyperthermia to control the function of synthetic cells has the potential to revolutionise targeted drug delivery, catalysing biosynthesis and/or release of pharmaceutically-active biomolecules only at the therapeutic site of interest. To realise this goal, the aim of this chapter is to detail the encapsulation of the magnetically-activated SNAs and an inactive DNA template encoding a protein of interest in a lipid bilayer, generating magnetically-controllable synthetic cells. This development process described herein consisted of the following activities:

- The encapsulation of magnetically-activated SNAs, inactive DNA template encoding mNG, and a CFPS system in a lipid bilayer using the inverted emulsion method, and activation of biosynthesis inside the resulting synthetic cell using magnetic hyperthermia, with and without an opaque blocking material.
- Expansion of the drug delivery platform, synthesising an inactive DNA template encoding a pore-forming protein for the selective release of an encapsulated model cargo in the presence of an AMF.

4.2. Magnetic-activation of gene-expressing synthetic cells

4.2.1. Magnetic-control of biosynthesis inside synthetic cells

To demonstrate the control of CFPS-containing synthetic cells with magnetic hyperthermia, magnetically-activated SNAs (T7 promoter-bound), the inactive DNA template encoding mNG, and CFPS system (PURExpress) were encapsulated inside lipid-based GUVs using the inverted emulsion method [52] (described in detail in Section 1.3.2). Egg-PC was chosen as the main lipid component of the GUVs due to its compatible transition temperature of 0 °C, ensuring that no grain boundary defects formed within the membrane as a result of the localised heating experienced from magnetic hyperthermia [193]. In the emulsion transfer method, the internal aqueous solution containing the magnetically-activated SNAs, inactive DNA template, PURExpress, and an internal buffer containing sucrose was suspended within an Egg-PC containing oil to form a w/o emulsion. The w/o emulsion was then centrifuged through a phase transfer column comprising an outer buffer containing glucose and a second Egg-PC monolayer. The act of forcing the w/o emulsion droplets across the second lipid monolayer engineered a lipid bilayer and resulted in GUV formation [49,52]. Texas Red™ dextran (TXR) dye was encapsulated as a component of the internal aqueous solution to allow for the GUVs to be visualised and imaged by fluorescence microscopy using the red channel fluorescence.

As before, the AMF parameters selected were a magnetic field strength of 30 mT and a frequency of 103.4 kHz, ensuring a magnetic field-frequency product below the safety limit [118] of $H \times f = 2.47 \times 10^9$ A·m^{-1}·s^{-1} and a frequency compatible with MagForce [102]. The timeframe was mediated to ensure that the inner solution did not heat to a temperature that resulted in the protein machinery denaturing and was found to be optimal at 10 min. The shorter timeframe required, compared with that optimised for the bulk CFPS (detailed in

Section 3.4), was hypothesised to be influenced by the compartmentalisation inside GUVs promoting a higher local concentration of magnetic nanoparticles. The temperature of the solution containing the CFPS system was measured by submerging a fibre optic probe and it did not exceed 33 °C during 10 min of AMF exposure with and without the magnetically-activated SNAs present, suggesting that the bulk heating observed is due to the heat dissipated from the solenoid coil (Fig. 4.2).

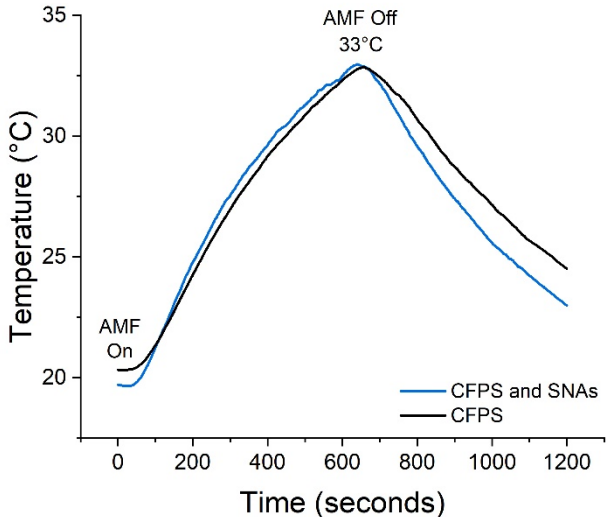

Fig. 4.2. Fibre optic probe data for the global heating experienced by magnetically-activated synthetic cells in the applied AMF. Fibre optic probe data from the probe being submerged in the CFPS solution and both in the presence and absence of the magnetically-activated SNAs, inside the solenoid coil and with exposure to an AMF for 10 min.

The GUVs containing the magnetically-activated SNAs (T7 promoter-bound), inactive DNA template encoding mNG, and PURExpress were exposed to an AMF (30 mT, 103.4 kHz) for 10 min, with a control experiment in the absence of an applied AMF. The expression of mNG inside the GUVs was investigated by measuring the fluorescence intensity of the expressed mNG using the green fluorescence channel of an epifluorescence microscope after a further incubation for 2.5 h and analysing the images using a circle detection-based image analysis script in MATLAB (https://zenodo.org/records/15692133). The fluorescence was compared with that of the inactive template alone (denoted the negative control) and the full template

with the dsDNA T7 promoter region intact (denoted the positive control). The synthetic cells encapsulating the magnetically-activated SNAs and the inactive DNA template, but without exposure to an applied AMF showed minimal mNG expression (mean fluorescence intensity = 3.03 grey units), compared with solely the inactive DNA template (mean fluorescence intensity = 0.00 grey units), demonstrating the robust "off" state (Fig. 4.3). The in-situ expression of mNG inside the synthetic cells was fully recovered after exposure to an applied AMF (30 mT, 103.4 kHz) for 10 min, compared with the full template (mean fluorescence intensity of 23.22 grey units vs 17.47 grey units). This regulation of biosynthesis in-situ and ability to selectively activate gene expression inside the synthetic cells was only achieved in the presence of the applied AMF and with the newly-developed magnetically-activated SNAs. This demonstration realises the remote control of synthetic cells with a tissue-penetrating and biocompatible stimulus using clinically-tolerable magnetic field strengths and frequencies.

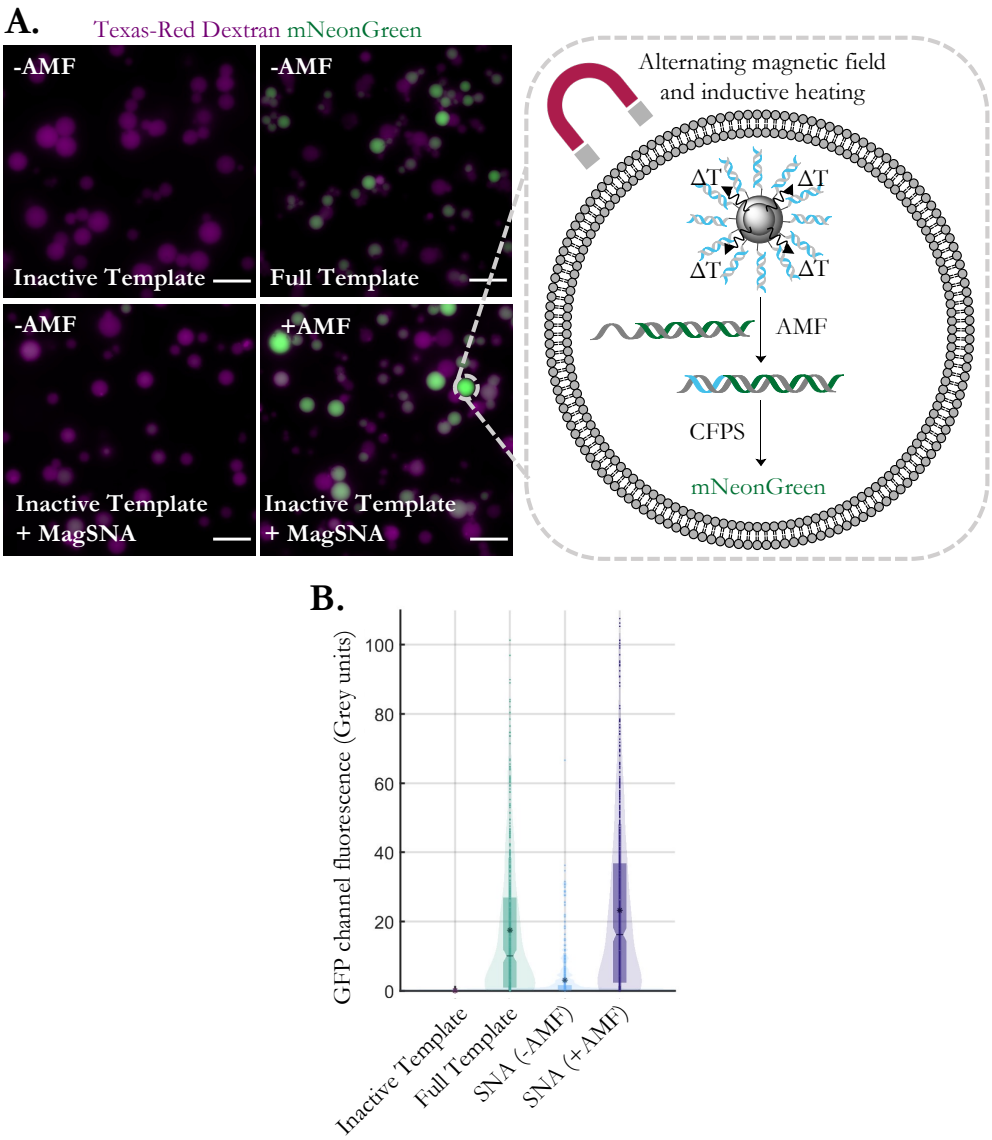

Fig. 4.3. On-demand activation of biosynthesis inside synthetic cells with magnetic hyperthermia. (A) Epifluorescence microscopy images visualising the in-situ expression of mNG inside synthetic cells with and without the application of an AMF and in the presence of encapsulated magnetically-activated SNAs. GUVs (visualised through TXR) expressed minimal mNG in the absence of an AMF, and their GFP channel fluorescence was comparable with GUVs that contained PURExpress and the inactive DNA template only. GUVs expressed mNG upon AMF exposure, as demonstrated by the increase in the green channel fluorescence, and were consistent with GUVs containing the full mNG template. Images represent n = 3 biological replicates. Scale bar = 20 µm. **(B)** Quantification of mNG expression in the individual GUVs using a circle detection-based image analysis script. Mean fluorescence intensity (inactive template) = 0.00 grey units; mean fluorescence intensity (SNA, –AMF) = 3.03 grey units; mean fluorescence intensity (full template) = 17.47 grey units; and mean fluorescence intensity (SNA, +AMF) = 23.22 grey units. Datasets respresent n = 3 biological replicates. The box plot, notch and asterisk represent the interquartile range, median and mean fluorescence intensity, respectively.

4.2.2. Determining the concentration of T7 promoter release in an AMF

To investigate the thermal parameters required for the release of the ssDNA T7 promoter "top" strand from the surface of the SNAs, we replicated the CFPS conditions inside the synthetic cells at a magnetically-activated SNA concentration of 400 nM and a concentration of the complementary T7 promoter "bottom" strand of 5 $ng \cdot \mu l^{-1}$ (free in-solution and not attached to the SNA). The presence of the T7 promoter "bottom" strand was to ensure that any ssDNA T7 promoter that was released hybridised to the complementary strand free in-solution and did not hybridise back onto the SNA. The CFPS buffer concentrations (50 mM HEPES, 400 mM potassium glutamate and 200 mM glucose at pH 7.6) were used to mimic the same conditions inside the synthetic cells.

The concentration of ssDNA T7 promoter released was tracked by the addition of the intercalating fluorescent dye, PicoGreen, commonly used to quantitate dsDNA with ssDNA present having minimal impact on the fluorescence intensity [194]. A solution of magnetically-activated SNAs, the ssDNA T7 promoter "bottom" strand, and the CFPS buffer were incubated at 40 °C, 45 °C, 50 °C and 55 °C or exposed to an AMF for 10 min, replicating the CFPS conditions inside the synthetic cells. A control sample at 4 °C was carried out and the resulting PicoGreen fluorescence intensity was used to normalise the other fluorescence intensities, thereby accounting for the fluorescence arising from dsDNA present on the surface of the SNA (that has not been released) and the free ssDNA T7 promoter "bottom" strand free in-solution. It is important to note that PicoGreen fluorescence is quenched on the surface of nanoparticles [195], hence the fluorescence associated with the free dsDNA was expected to be higher. After normalising, the fluorescence intensity of the dsDNA present after 10 min exposure to an AMF (30 mT, 103.4 kHz) was higher than that after 10 min at 40 °C (3818 A.U. vs. 4798 A.U.) and more closely aligned with the amount of dsDNA

present after 10 min at 45 °C (4798 A.U. vs. 5045 A.U.) (Fig. 4.4). It can be inferred that the surface of the SNA was heated to around 45 °C during exposure to this AMF (30 mT, 103.4 kHz). Taking into account that the temperature of the bulk did not exceed 33 °C during AMF exposure (10 min) when the magnetically-activated SNAs were present at the concentration required for CFPS inside synthetic cells (determined by a fibre optic probe), it is notable that the surface temperature of around 45 °C and the amount of ssDNA released from this heating was as a result of inductive heating (Fig. 4.4). This reiterates the importance of magnetic hyperthermia as the mechanism of release, being shown as a necessity to obtaining reasonable ssDNA T7 promoter release for downstream application.

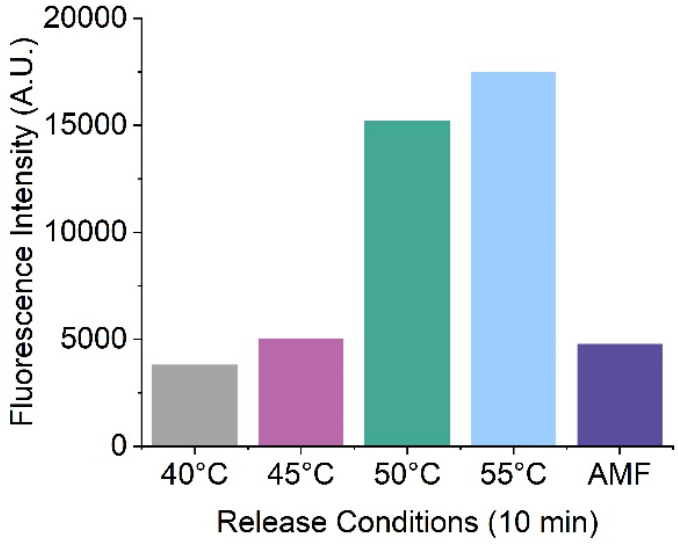

Fig. 4.4. Release studies of the magnetically-activated SNAs. Release studies and incubation of the magnetically-activated SNAs, T7 promoter "bottom" strand in-solution, and the CFPS buffer (50 mM HEPES, 400 mM potassium glutamate and 200 mM glucose at pH 7.6) at 40 °C, 45 °C, 50 °C and 55 °C, and compared with exposure to an AMF (30 mT, 103.4 kHz). The relative concentration of the released ssDNA T7 promoter "top" strand was inferred from a PicoGreen assay, measuring the newly-formed dsDNA upon annealing to the T7 promoter "bottom" strand that was free in-solution. The fluorescence intensity of the dsDNA present after 10 min exposure to an AMF was comparative to that after 10 min at 45 °C. It can be inferred that the temperature at the surface of the SNA is heated to around 45 °C during AMF exposure. The release is higher at 55 °C as this is near the T_m of the duplex. Data is presented from n = 1 technical repeat.

4.2.3. Magnetic-control of synthetic cells within an opaque blocking layer

Magnetic hyperthermia confers notable advantages over the previously published remote stimuli, predominantly UVA light, including the ability to penetrate bodily tissue by >10 cm with AMFs compared with <1 mm with UVA light [52,92,95]. UVA light also poses cytotoxicity risks, whereas AMFs are biologically benign and magnetic hyperthermia is clinically-approved to ablate malignant tumours as an anticancer therapy [91,102]. Our developed platform that has repurposed magnetic hyperthermia to control the function of gene-expressing synthetic cells uses magnetic field strengths and frequencies that are within the clinically-tolerable limit and compatible with the approved AMF generator by MagForce [102]. Moreover, our central scaffold of the magnetically-activated SNAs (comprising IONPs@SiO_2) is comparable with the clinical formulation NanoTherm® (aminosilane-coated ferrofluid) that is administered to patients undergoing magnetic hyperthermia treatment for glioblastoma [102].

To further demonstrate the superiority over the state-of-the-art and the applicability of AMFs as an external stimulus, protein production inside synthetic cells was activated within an opaque blocking material (black tube). These types of materials, being rigid polymers, have been used as mimics of hard tissues [196–198] and act further as a blocking layer that is impenetrable to the current state-of-the-art remote stimuli: small molecules and light [52]. As was previously observed, there was minimal leakage of mNG expression in the absence of an AMF (mean fluorescence intensity = 5.06 grey units) (Fig 4.5). The ability to control in-situ expression of mNG by releasing the T7 promoter sequence from the encapsulated magnetically-activated SNAs with magnetic hyperthermia was not perturbed by the opaque blocking layer (mean fluorescence intensity = 24.55 grey units). The conservation of green channel fluorescence that is associated with mNG expression only after exposure to an AMF

and now in an opaque blocking material, which is otherwise impenetrable to current activation methods, is an advancement in the external control of gene-expressing synthetic cells.

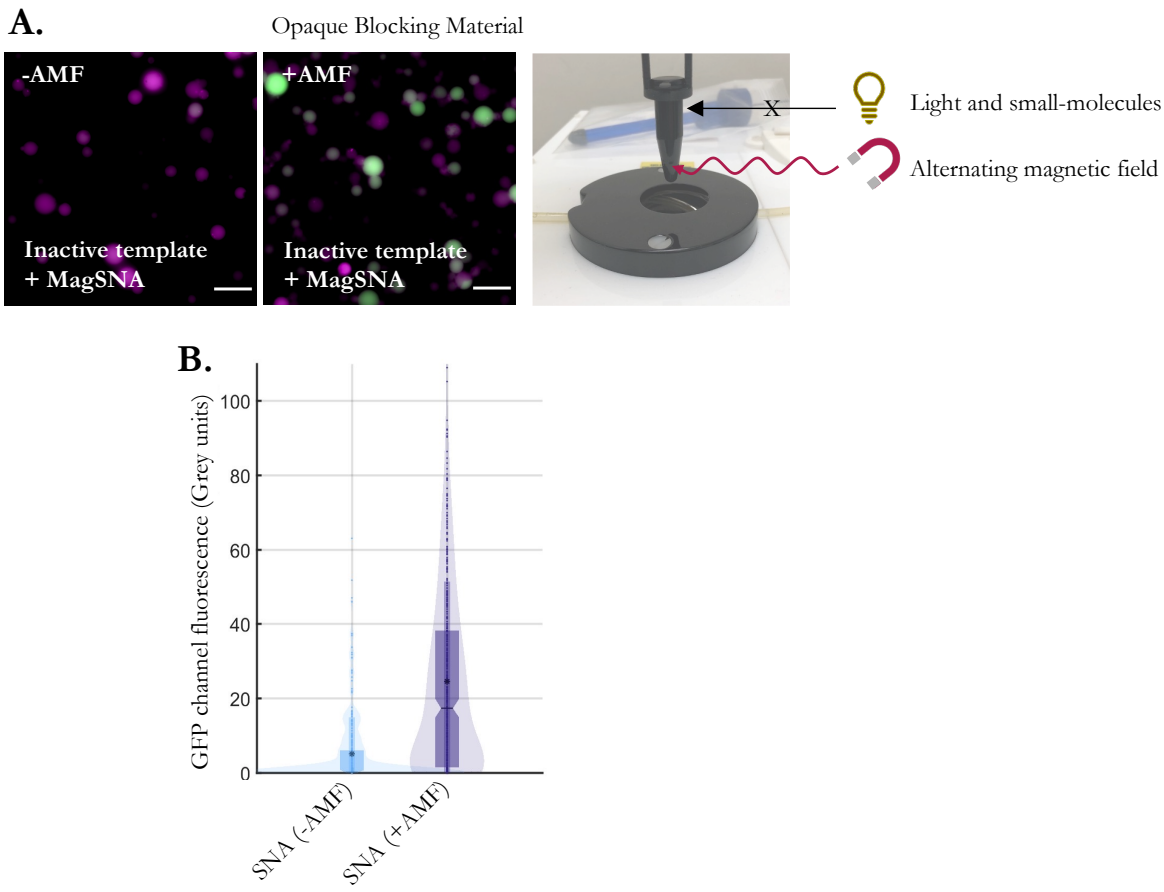

Fig. 4.5. On-demand activation of biosynthesis inside synthetic cells with magnetic hyperthermia and in an opaque blocking material. (A) Epifluorescence microscopy images visualising the in-situ expression of mNG inside synthetic cells with and without the application of an AMF and in the presence of encapsulated magnetically-activated SNAs. GUVs (visualised through TXR) expressed minimal mNG in the absence of an AMF. GUVs expressed mNG upon AMF exposure, as demonstrated by the increase in the green channel fluorescence, unperturbed by the opaque blocking layer. Images represent n = 3 biological replicates. Scale bar = 20 μm. **(B)** Quantification of mNG expression in the individual GUVs using a circle detection-based image analysis script. Mean fluorescence intensity (SNA, –AMF) = 5.06 grey units and mean fluorescence intensity (SNA, +AMF) = 24.55 grey units. Datasets represent n = 3 biological replicates. The box plot, notch and asterisk represent the interquartile range, median and mean fluorescence intensity, respectively.

4.3. Magnetically-induced cargo release from synthetic cells

4.3.1. Synthesis of the inactive DNA template

To realise the utility of the technology and show that the approach in generalisable, the inactive DNA template was replaced with one encoding the pore-forming protein alpha-hemolysin (α-HL). The magnetically-activated SNAs (T7-promoter bound) were exploited to activate CFPS of α-HL with magnetic hyperthermia, enabling the expression of α-HL and its insertion into the lipid membrane of the synthetic cells, thereby facilitating the release of encapsulated small molecules from the pore (1.2 nm diameter [199]).

The inactive DNA template encoding α-HL was synthesised in an identical manner to that described in Section 3.3. Two DNA templates encoding α-HL were synthesised by PCR: one with and one without the dsDNA T7 promoter region. A 5′-phosphorylated primer was used for the coding strand of the DNA template with the dsDNA T7 promoter region present and the template strand of the DNA template with the dsDNA T7 promoter region missing, enabling the digestion of the individual phosphorylated strands by lambda exonuclease, yielding two linear ssDNA sequences. The intact coding strand with the T7 promoter region missing and the intact template strand with the T7 promoter region present were then annealed together to synthesise the inactive DNA template encoding α-HL. The design exploits the T7 promoter strand that is released with magnetic hyperthermia for hybridisation to the ssDNA 3′-overhang on the template strand, restoring the dsDNA T7 promoter region and enabling the T7 RNA polymerase to bind and activate CFPS. The synthesis of the inactive DNA template was quantified by 1.5% (w/v) agarose gel electrophoresis and compared with a 1 kb DNA ladder (NEB) (Fig. 4.6).

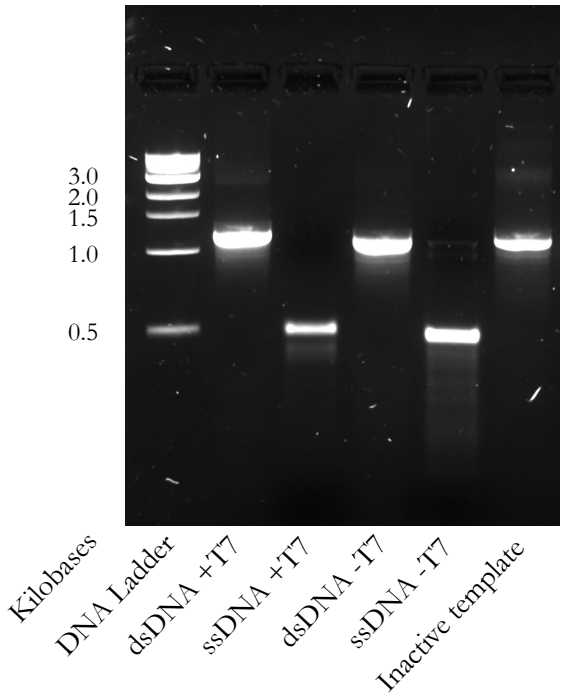

Fig. 4.6. Synthesis of the inactive α-HL template. Native 1.5% (w/v) agarose gel quantifying the synthesis of the inactive template with the dsDNA with (dsDNA +T7) and without (dsDNA -T7) the T7 promoter region present, its digestion to the ssDNA "bottom" strand with the T7 promoter present (ssDNA +T7) and the ssDNA "top" strand without the T7 promoter (ssDNA -T7) present, prior to the formation of the inactive template (inactive template).

4.3.2. Controlling the release of cargo from synthetic cells with magnetic hyperthermia

The ability of magnetic hyperthermia to activate the expression of α-HL inside synthetic cells and release a model cargo was investigated by encapsulating magnetically-activated SNAs (T7 promoter-bound), an inactive DNA template encoding α-HL, the fluorescent small molecule 2-(*N*-(7-nitrobenz-2-oxa-1,3-diazol-4-yl)amino)-2-deoxyglucose (2-NBDG), and a CFPS system (PURExpress) inside lipid-based GUVs using the inverted emulsion method [52] (described in detail in Section 1.3.2). In addition, control GUVs were also prepared without the magnetically-activated SNAs but with PURExpress and either the inactive α-HL template (negative control) or the full α-HL template with the dsDNA T7

promoter region intact (positive control). The positive control represented the maximum release of cargo that was tracked by the loss of fluorescence intensity in the green channel fluorescence associated with the 2-NBDG releasing through the in-situ synthesised α-HL pore. The GUVs were imaged by fluorescence microscopy at $t = 0$ h, as this was the timepoint in which the maximum fluorescence intensity of 2-NBDG encapsulated inside the synthetic cells was expected to occur. The GUVs were exposed to an AMF (30 mT, 103.4 kHz) for 10 min, (a control experiment was conducted without the application of an AMF), followed by incubation for 4 h to facilitate the CFPS of α-HL, its insertion into the lipid membrane, and the release of 2-NBDG as the model cargo. The release (or lack thereof) of 2-NBDG was investigated by measuring the mean fluorescence intensity in the green channel fluorescence at $t = 4$ h.

In the positive control containing the full α-HL DNA template with the dsDNA region intact, α-HL expression and cargo release was observed as tracked by the loss of 2-NBDG fluorescence (mean fluorescence intensity = 44.72 grey units at $t = 0$ h changing to 20.33 grey units at $t = 4$ h) (Fig. 4.7). In contrast, the 2-NBDG fluorescence was conserved for the negative control with synthetic cells that encapsulated the inactive α-HL template alone (mean fluorescence intensity = 49.80 grey units at $t = 0$ h changing to 41.97 grey units at $t = 4$ h). In the absence of an applied AMF, the synthetic cells encapsulating the magnetically-activated SNAs and the inactive α-HL template retained the 2-NBDG fluorescence after 4 h (mean fluorescence intensity = 38.81 grey units at $t = 0$ h changing to 40.90 grey units at $t = 4$ h), demonstrating a robust "off" state without the leakage of α-HL expression. However, following exposure to an applied AMF (30 mT, 103.4 kHz) for 10 min, the expression of α-HL and release of 2-NBDG fluorescence was similar to the positive control (mean fluorescence intensity = 38.81 grey units at $t = 0$ h changing to 17.92 grey units at $t = 4$ h). This demonstration of a viable release mechanism, activated

only in the presence of the magnetic field, holds promise for the controlled delivery of bioactive molecules in-vivo.

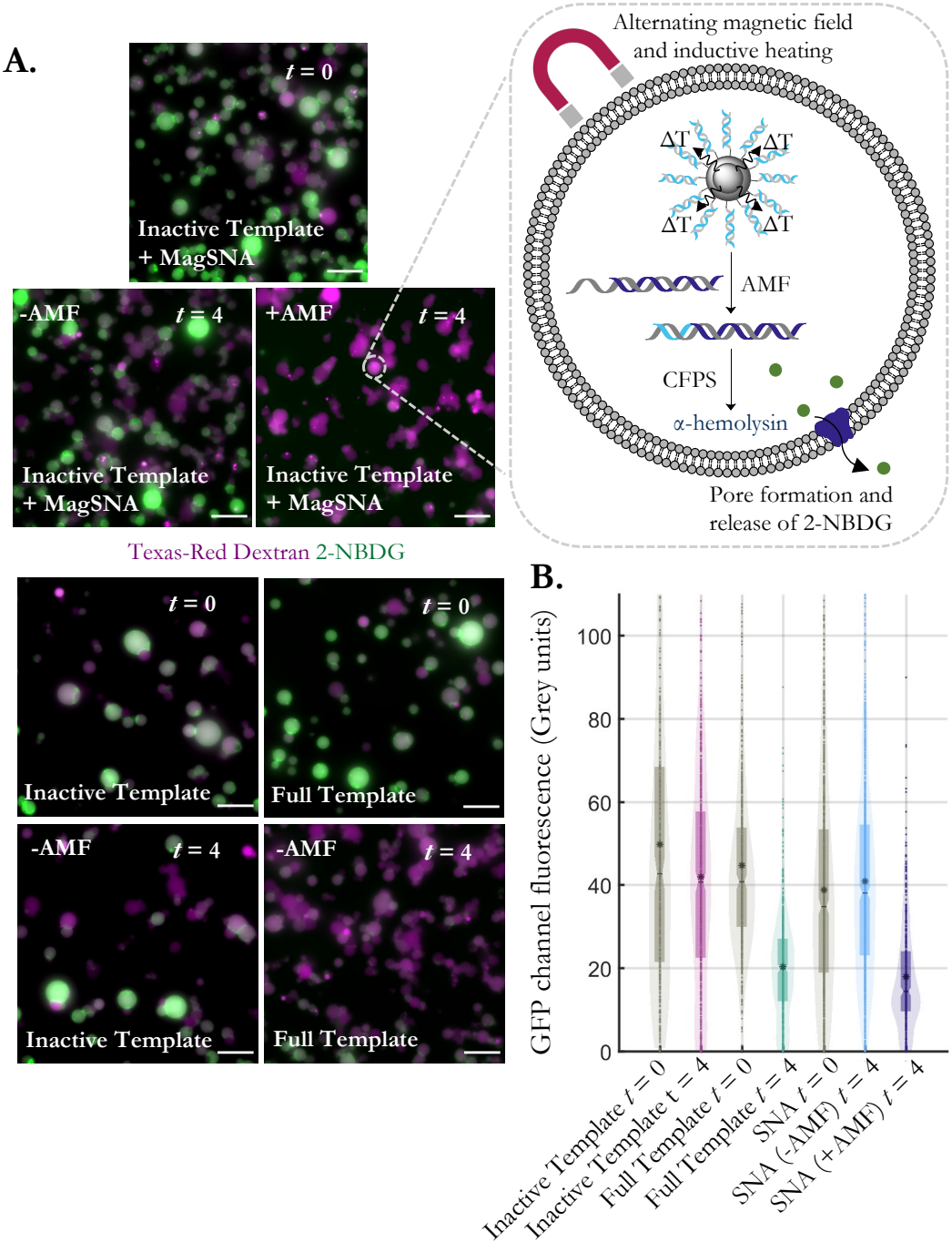

Fig. 4.7. Controlling the expression of a pore-forming protein, releasing cargo on-demand from synthetic cells with magnetic hyperthermia. (A) Epifluorescence microscopy images visualising the on-demand expression of α-HL inside synthetic cells, releasing the fluorescent small molecule 2-NBDG only in the presence of an AMF. The synthetic cells (visualised through the encapsulated TXR and the red channel fluorescence) that encapsulated the magnetically-activated SNAs and the inactive α-HL template retained the fluorescence intensity associated with 2-NBDG in the absence of the AMF, indicative

of minimal α-HL expression, preventing the formation of pores in the lipid membrane and the leakage of 2-NBDG. This was comparable with the negative control that contained the inactive α-HL template and PURExpress only. The synthetic cells that were exposed to an AMF showed a loss of 2-NBDG and its fluorescence overtime, representative of the in-situ α-HL expression activated by magnetic hyperthermia. This was comparable with the loss of 2-NBDG fluorescence observed in synthetic cells containing the full α-HL template (dsDNA T7 promoter region present). Images represent n = 4 biological replicates. Scale bar = 20 μm. **(B).** Quantification of 2-NBDG fluorescence in the individual GUVs using a circle detection-based image analysis script at $t = 0$ h and $t = 4$ h. Mean fluorescence intensity (full template) = 44.72 grey units at $t = 0$ h and mean fluorescence intensity (full template) = 20.33 grey units at $t = 4$ h; mean fluorescence intensity (inactive template) = 49.80 grey units at $t = 0$ h and mean fluorescence intensity (inactive template) = 41.97 grey units at $t = 4$ h; mean fluorescence intensity (SNA, no AMF) = 38.81 grey units at $t = 0$ h and mean fluorescence intensity (SNA, no AMF) = 40.90 grey units at $t = 4$ h; and mean fluorescence intensity (SNA, AMF) = 17.92 grey units at $t = 4$ h. Datasets represent n = 4 biological replicates. The box plot, notch and asterisk represent the interquartile range, median and mean fluorescence intensity, respectively.

4.4. Conclusion

The selective regulation of biosynthesis and release of cargo inside synthetic cells using the clinically-approved and tissue-penetrating anticancer therapy, magnetic hyperthermia, has been realised. Notably, the magnetic field strength and frequency of the applied AMF were within the tolerable limit, set to minimise patient discomfort, and the magnetic excitation frequency of ~100 kHz is compatible with the only clinically available magnetic hyperthermia system by MagForce [102]. The modular nature of the system has allowed multiple proteins to be synthesised in-situ and only in the presence of the AMF. Indeed, this programmability will allow for more pharmaceutically-relevant proteins (such as antibodies) to be accessed in the future, whereby the in-situ production of biologics holds promise for circumventing side effects caused by drug leakage during storage and/or in circulation that may arise from pre-loading vesicles [74]. The ability to control the activity of synthetic cells within an opaque blocking material renders the developed technology advantageous over small molecule or light activation, which are the current state-of-the-art. To develop the

technology, the stability in a sophisticated tissue model should be investigated[200] and the targeting activity in-vivo [72,73,75]. Furthermore, the lipid bilayer can be functionalised with targeting ligands [183], to increase synthetic cell concentration at the therapeutic site of interest, and stealth polymers [69–71], to improve stability and circulation. This compelling proof-of-concept, comprising a platform that harnesses the heat dissipated from magnetic hyperthermia to control the on-demand synthesis and release of biomolecules from synthetic cells, has the potential to revolutionise targeted drug delivery, thereby opening up applications for synthetic cells as "smart" drug delivery devices.

5

Conclusions and future directions

5.1. Conclusions

A controllable drug delivery platform has been developed, which mimics the SNA architecture and harnesses the heat dissipated from magnetic hyperthermia (a tissue-penetrating anticancer therapy) to release DNA strands and control the downstream function of the gene. Notably, the magnetic field strength (30 mT) and excitation frequency (103.4kHz) of the applied AMF are within a tolerable limit set to minimise patient discomfort, and the magnetic excitation frequency of ~100 kHz is compatible with the only

clinically available magnetic hyperthermia system by MagForce [102]. The utilisation of click chemistry allowed for the easy replacement of the model DNA sequence with an ASO and the T7 promoter sequence. As such, magnetic hyperthermia was initially utilised to selectively control gene knockdown by releasing an ASO sequence as a result of the localised heating denaturing the bound dsDNA, enabling the specific binding of the newly-released ASO to its cognate mRNA and the catalytic downregulation of a model mRNA sequence (mRNA encoding the fluorescent protein mVenus).

The reach of the delivery platform was expanded by modifying these magnetically-activated SNAs with the T7 promoter sequence, enabling the selective control of CFPS inside synthetic cells. This was achieved by synthesising an inactive DNA template encoding the protein of interest, comprising a ssDNA 3′-overhang (of the "bottom" T7 promoter sequence) and a coding strand with the T7 promoter sequence missing. This design took advantage of the T7 RNA polymerase only transcribing from a dsDNA T7 promoter and allowed for the released ssDNA T7 promoter "top" strand from the surface of the SNAs in an applied AMF to hybridise to the inactive DNA template encoding the protein of interest [181,182]. The restoration of the dsDNA T7 promoter region as a result of magnetic hyperthermia allowed for the T7 RNA polymerase (in the PURExpress) to recognise the dsDNA T7 promoter region, activating CFPS of the encoded protein. This mechanism was exploited to synthesise the green fluorescent protein mNG and the pore-forming protein α-HL inside synthetic cells on-demand and only in the presence of the AMF. The latter allowed for an initial release system to be tested, whereby the in-situ synthesised α-HL subsequently inserted itself into the lipid membrane and released a model cargo encapsulated inside the synthetic cells.

Critically, the promising “off” state, showing negligible gene knockdown and/or protein expression in the absence of the magnetic field, was only achieved with the newly-developed SNA purification technique. This involved pulling pre-adsorbed DNA from the surface of the nanoparticle using an electric current that was applied through a 1.5% (w/v) agarose gel; the covalently-constructed SNA did not travel through the gel and was then extracted through brief sonication of the excised well in Milli-Q water.

The modular nature of the system and inherent programmability will allow for more pharmaceutically-relevant proteins (such as antibodies) to be accessed in the future by simply changing the inactive DNA template, and the in-situ production of biologics holds promise for circumventing side effects caused by drug leakage during storage and/or in circulation that may arise from pre-loading vesicles [74]. The bound ASO sequence can also be replaced with other clinically relevant therapeutics such as mRNA.

This compelling proof-of-concept, a technology that harnesses the heat dissipated from magnetic hyperthermia to control the function of nucleic acids, has the potential to revolutionise targeted drug delivery, activating the drug itself or catalysing biosynthesis and release of therapeutically-active biomolecules only at the target tissue. This remote control of nucleic acids with a non-invasive, tissue-penetrating, and biocompatible external stimulus holds promise as a complementary strategy to active targeting for improving the biodistribution of SNAs and/or synthetic cells in-vivo, realising the technologies as “smart” drug delivery devices.

5.2. Other investigated directions

Herein lists approaches that were undertaken but ultimately unsuccessful, and are therefore not discussed further in this thesis:

- Initially, triethylene glycol-capped IONPs were synthesised by thermal decomposition. However, attempts to encapsulate in silica via the Stöber method were unsuccessful with the majority of the nanoparticles comprising by-product silica with no IONP core.
- A variety of ligand exchanges were attempted including with an in-house synthesised multifunctional phosphonic acid linker (incorporating both PEG and furan groups), and separately a commercially available carboxylic acid linker (citrate). The former exchange was utilised to attach maleimide-modified DNA and take advantage of retro-Diels Alder in an AMF. However, the release was problematic, likely because the temperature required for retro-Diels Alder, being on the order of 100 ºC, was incompatible with the heating efficiency of the IONPs. Concerns were also raised as to whether the phosphate backbone of the DNA would displace the phosphonic acid linker. The latter exchange was used to attach DNA through coupling amine-modified DNA to the surface. This reaction proved unsuccessful with little to no detectable loading.
- A variety of methods were explored to determine the loading of DNA including using PicoGreen (to intercalate with dsDNA on the surface); attaching a fluorophore (fluorescein) to the 5′ end of the non-covalently bound DNA and tracking fluorescence both when hybridised and released, separating out the NPs in the latter through centrifugation and pelleting to analyse only the supernatant. In all cases the fluorescence of the dye was quenched by the presence of the NPs, which were challenging to entirely remove.

- A variety of methods were explored to isolate the NPs including using Amicon ultrafiltration devices and an assortment of magnets. The NPs aggregated in the Amicon filter and were troublesome to remove without harsh sonication, which gave rise to concerns of DNA fragmentation. The small size of the NPs (impacting their residual magnetism) meant that they did not separate out with conventional magnets.
- Circular dichroism was explored to detect DNA on the surface of the NPs, however, the absorption of the IONPs was too strong in the wavelengths associated with DNA between 200 and 300 nm. The absorbance of IONPs was also problematic for determining DNA loading through UV-Vis spectroscopy and the peak associated with DNA at 260 nm.

5.3. Future directions

5.3.1. SNA engineering

The current design serves as a compelling proof-of-concept, though there is scope for further improvement, in particular with regards to the release efficiency of ssDNA from the surface of the SNAs as a result of magnetic hyperthermia. One route to improve the release efficiency is to improve the magnetic heating efficiency of the IONPs. To this end, it would be advantageous to investigate various strategies for enhancing the specific heat absorption rate including: increasing the size of the magnetic nanoparticles; doping with divalent transition metal cations (such as Mn^{2+}, Ni^{2+}, Co^{2+} and Zn^{2+}); and changing the morphology (such as nano-cubes and nanoflowers) [98]. This would allow for greater inductive heating in an AMF, enabling the bound-dsDNA to experience a temperature closer to its T_m, with the added potential of then releasing a higher concentration of ssDNA as a result of more efficient denaturation at the surface of the nanoparticles. In addition, the distance between the surface of the IONP core and the bound dsDNA could be reduced by thinning the silica shell or exploring direct conjugation to increase the heating experienced by the dsDNA on

account of magnetic hyperthermia, particularly as the heating decays exponentially with distance from the surface of the nanoparticle [109].

In the current iteration of the technology, the "off" state, in which no DNA is released in the absence of the magnetic field, is not as robust at body temperature (~37 °C) compared with ambient temperature (25 °C). To enable the translation of the system to in-vivo applications, the length of the bound dsDNA could be increased to influence a higher T_m and/or a capping group could be introduced to the terminal base such as a 5′dimethoxytrityl-uridine cap that has been shown to stabilise the duplex and prevent fraying/wobbling at the terminus of the dsDNA [201]. Following these optimisations, temperatures in the mild hyperthermia regime (between 39 – 43 °C), known to increase perfusion, improve blood flow and activate an immune response, could be accessed, whereby this increase in temperature will also influence the release of a higher DNA concentration by increasing the AMF exposure timeframe [100]. This dual therapeutic (mild hyperthermia coupled with drug release) has been used for triggering retro-Diels Alder release of chemotherapeutics using magnetic hyperthermia to attenuate tumour growth in xenograft-bearing mice, with the maintenance of bulk heating in the mild hyperthermia regime [202].

5.3.2. Controlling gene silencing with magnetic hyperthermia

To develop the magnetic-control of gene knockdown towards clinical application, the magnetically-activated SNAs (ASO-bound) should be translated to a cell model (prior to application in an in-vivo mouse model) and the ASO replaced with one that targets a pharmaceutically-relevant oncogene. Initially, the transfection and intracellular trafficking of the magnetically-activated SNAs could be investigated. Fluorescence microscopy could be utilised to aid visualisation by incorporating rhodamine dye into the silica shell, by modifying APTS [203], and incorporating a fluorescent dye (such as fluorescein) onto the

terminal base of the ASO. Indeed, the serum nuclease resistance could be investigated by incubation with fetal bovine serum, measuring the remaining dsDNA on the surface by the fluorescence intensity of free fluorescein in the supernatant, and the cytotoxicity of the magnetically-activated SNAs could be explored by treating the cells with increasing concentrations and measuring cell viability.

The ASO sequence could be replaced with another ASO sequence that instead targets oncogenes in solid tumours, capitalising on the ability of AMFs to penetrate bodily tissue. Various ASOs are in clinical trials to treat solid tumours including: WGI-0301, an ASO targeting Akt-1 mRNA, whereby the overexpression of Akt-1 is associated with tumour growth and drug resistance [204,205]; Oblimersin, an ASO targeting Bcl-2 mRNA, whereby the overexpression of Bcl-2 is associated with chemotherapy resistance [206,207]; and OGX-011, an ASO targeting clusterin, whereby clusterin inhibits apoptosis and promotes tumour progression [208,209] amongst others [210]. The knockdown activity of the ASO that is taken forward could then be investigated in a suitable cell line with and without an applied AMF, measuring both the levels of mRNA with reverse transcription quantitative polymerase chain reaction (rt-qPCR) and protein with western blotting. Suitable controls include benchmarking the magnetically-induced knockdown against gymnotic delivery (no transfection agent) and scrambled ASO sequences [211]. The timeframe, magnetic field strength, and magnetic excitation frequency of the applied AMF could be optimised, whereby the bulk heating observed in the AMF with the current parameters could be mediated by exploring a pulsed regime with intermittent AMF exposure applied sequentially, previously demonstrated in-vivo [212]. Future work could be carried out with a more complex tissue model, including an ex-vivo human skin model [200] and further an in-vivo mouse model [72,73,75].

5.3.3. Controlling the in-situ synthesis and release of biologics from synthetic cells with magnetic hyperthermia

The newly-developed magnetically-activated synthetic cells have the potential act as a new therapeutic, bridging molecular therapies and live cell therapies (such as CAR T-cell therapy and genetically-engineering immune cells). To this end, the technology needs to be expanded to include clinical biologics and translated to a cell model (prior to application in an in-vivo mouse model) to assess its applicability as a controllable drug delivery platform.

The modular nature of the technology could allow for more pharmaceutically-relevant proteins to be accessed. For instance, future work may focus on harnessing magnetic hyperthermia to catalyse the on-demand synthesis and release of biologics in combination with chemotherapeutics to develop a targeted adjuvant therapy. To achieve this, the inactive DNA template could be changed to encode a range of biologics with varying sizes, including: Trastuzumab antibody ~148 kDa [175], Pseudomonas *aeruginosa* exotoxin T (ExoT) ~66 kDa [213], 7D12 nanobody ~15 kDa [214]. Anti-/nano-bodies bind to receptors on cancer cells, disrupting signalling pathways for therapeutic effect, and have been produced by CFPS [175,214]. ExoT has potent anticancer effects that requires targeting in-vivo, proving a model candidate for in-situ production with AMFs [213].

The on-demand synthesis of biologics could be investigated initially by CFPS in-solution and without encapsulation inside synthetic cells. The SNAs, inactive DNA template, and CFPS system could be exposed to an AMF (and a control without an AMF), and compared with the inactive DNA template alone (negative control) and the full template (positive control). The synthesis of the biologics can be analysed by PAGE and enzyme-linked immunosorbent assays (ELISA). Anti-/nano-bodies are often used with chemotherapeutics

such as docetaxel [215]. To release the biomolecules and docetaxel from the synthetic cells with magnetic hyperthermia, an inactive DNA template of the pore-forming protein Perfringolysin O (PFO) (25-30 nm pore diameter) could be synthesised, as PFO has previously been used to release molecules from synthetic cells [216]. The SNAs, inactive DNA template encoding the biologic and PFO, docetaxel and CFPS system could then be encapsulated in a lipid bilayer, forming synthetic cells. These synthetic cells could be incubated with a suitable cell line (such as SKBR-3 cells that overexpress HER2 receptors for Trastuzumab) and exposed to an AMF (and a control experiment without an AMF), and compared with synthetic cells containing the inactive DNA template encoding PFO alone (negative control) and the full template encoding PFO (positive control). Cell viability/cytotoxicity tests could be performed in a time course.

The magnetically-activated synthetic cells could then be applied to a sophisticated tissue model [200] and the targeting activity evaluated in-vivo [72,73,75]. The lipid bilayer could be functionalised with targeting ligands [183] to increase synthetic cell concentration at the therapeutic site of interest, and "stealth" polymers[69–71] to improve stability and prevent protein corona. Poly(sarcosine) (PSar) could be investigated as the "stealth" polymer, as growing concerns surrounding PEG and its patient hypersensitivity has driven research into PSar as a promising, less immunogenic, alternative [217,218]. PSar is synthesised by ring-opening polymerisation of sarcosine *N*-carboxyanhydride; notably, the utilisation of an alkyne-modified initiator (such as propargylamine) would allow for the "stealth" polymer to be conjugated to commercially-available N_3-modified lipids by copper-catalysed click chemistry. The "stealth" polymer and/or the lipids themselves could be functionalised with targeting groups such as folate molecules, exploiting the overexpression of folate receptors on the surface of cancers to target payloads [183]. To assess the targeting ability, mNG-expressing synthetic cells as described in Section 4.2, modified with and without folate,

could be incubated with SKBR-3 cells (that overexpress folate receptors) and compared with the folate receptor-negative control cell line C30. Fluorescence microscopy would be useful to measure the proximity of the synthetic cells (by visualising encapsulated TXR dye in the red channel fluorescence) to the SKBR-3 cells, assessing the folate targeting. The AMF parameters could be optimised to ensure cell survival and mNG expression (tracked by the green channel fluorescence).

6

Methodology

6.1. Materials

All solvents and reagents were purchased from Sigma-Aldrich/Merck unless stated otherwise. Iron acetylacetonate was purchased from Fluorochem Ltd. DBCO-NHS ester was purchased from Cambridge Bioscience Ltd. DreamTaq DNA polymerase master mix, TXR-dextran (10 kDa) and 25 µL gene frames were purchased from Thermo Fisher Scientific. RNase H, ssRNA ladder, HiScribe® T7 High Yield RNA Synthesis Kit, murine RNase inhibitor, PURExpress, lambda exonuclease, purple loading dye (6X) and RNA gel loading dye (2X) was purchased from New England Biolabs. Egg PC was purchased from Avanti

Polar Lipids. ASO, T7 promoter and DNA primer sequences were synthesised by Integrated DNA Technologies. Native Loading Dye (2X) was gifted by Dr Denis Hartmann (University of Oxford).

6.2. Characterisation

DLS was performed with a Zetasizer-Nano-ZS (Malvern Instruments, Ltd) at 25 °C with nanoparticle solution at a concentration of 50 mg L^{-1} to obtain the hydrodynamic diameter, polydispersity index and zeta potential.

XRD patterns were obtained using an Xcalibur PX Ultra diffractometer (Oxford Diffraction Ltd.) equipped with a CoKα radiation source (λ = 1.79 Å) operated at 40 mA. The crystallite diameter was evaluated by considering the X-ray wavelength, λ = 0.154 nm, with the crystallite-shape factor *K* set to 0.9, and the line broadening at the full half-width maximum of the most intense peak (in radians) and the Bragg angle (q = 0.31 rad)[141].

$$D_{\mathrm{XRD}} = \frac{K\lambda}{\beta \cos(\theta)} \qquad \textbf{Eq. 1}$$

TEM images were captured using a CX100 II TEM (JEOL, Ltd) at 100kV. Nanoparticle dispersions (0.1 mg mL^{-1} in ethanol) were drop-casted onto carbon-coated copper grids and air-dried at room temperature. Particle size analysis was performed on >100 particles using ImageJ (an open-source platform: https://imagej.net/licensing/open-source) software.

The magnetic properties were characterised using an MPMS-5S superconducting quantum interference device (SQUID) magnetometer (Quantum Design, Ltd).

Alternating magnetic fields were generated using an NAN201003 Magnetherm (Nanotherics Ltd) with an 18-turn coil of 50 mm internal diameter and at a magnetic field strength of 30 mT and a frequency of 103.4 kHz.

Oligo mass spectrometry was carried out on a Xevo G2 QTOF mass spectrometer (Waters Corporation) and ^{1}H NMR spectroscopy was carried out on an AVF400 Bruker UltraShield™ 400 MHz (Bruker Corporation).

6.3. Chapter 2 methods

6.3.1. Synthesis of the oleylamine-capped iron oxide nanoparticles

Iron acetylacetonate (1.0595 g, 3 mmol) was dissolved in 15 mL of benzyl ether and 15 mL of oleylamine. The reaction vessel was evacuated and filled with argon five times (the vacuum was held for 5 min per cycle), following which it was purged with argon for 5 min to remove any remaining moisture. Under an argon atmosphere, the solution was heated to 110 °C at 3 °C min^{-1} then dehydrated for 1 h, before being heated to 293 °C at 20 °C min^{-1} and held for 1 h. The solution was magnetically stirred throughout the synthesis at 500 rpm. Ethanol (40 mL) was subsequently added to the reaction mixture and the black material was precipitated and separated via centrifugation (4297 x *g*, 10 min). The precipitate was dissolved in cyclohexane. Undispersed residue was removed by centrifugation (4297 x g, 10 min). The product was precipitated with ethanol and centrifuged (4297 x g, 10 min) to remove the solvent, and re-dispersed into cyclohexane. The resulting oleylamine-capped iron oxide nanoparticles were stored at 4 °C in cyclohexane [137,138].

6.3.2. Silica encapsulation and amine modification of the iron oxide nanoparticles

IGEPAL-*co*-520 (0.5 mL, 0.5 g, 1 mmol) was dispersed in cyclohexane (11 mL, 101 mmol) and injected with oleylamine-capped iron oxide nanoparticles dispersed in cyclohexane (1 mL, 15 mg mL^{-1}). The dispersion was sonicated for 10 min at ambient conditions. Ammonium hydroxide 1M (0.13 mL, 0.13 mmol) was added to the aforementioned reaction mixture that was being magnetically stirred at 600 rpm. The

controlled addition of TEOS (317 µL, 1.42 mmol) was performed using fractionated drop-method, in which 39.6 µL of TEOS was added every 3 h. A total of three additions were carried out per day and reacted overnight, meaning the fourth addition was carried out 24 h after the first addition and the seventh addition was carried out 48 h after the first addition. APTES (39.4 µL, 0.17 mmol) was added 3 h after the eight addition of TEOS and the reaction was left overnight. The reaction was then diluted with ethyl acetate. Centrifugation (4297 x *g*, 10 min) was applied to pelletise the nanoparticles and enable the removal of the solvent. The nanoparticles were then dispersed in ethanol by sonication and diluted with ethyl acetate (1 part nanoparticle-ethanol dispersion to 3 parts ethyl acetate) before pelletising by centrifugation (4297 x *g*, 10 min) and removing the solvent. This step was repeated twice more to remove the IGEPAL-*co*-520. The resulting silica-encapsulated iron oxide nanoparticles were then dispersed in ethanol (1 mL) to give a concentration of 15 mg mL^{-1}, and the dispersion was stored at 4 °C [145].

6.3.3. Modification with the DBCO click-handle

Amine-modified silica-encapsulated iron oxide nanoparticles (300 µL, 5 mg mL^{-1}) were re-dispersed in MOPS buffer (0.1 M, pH 7.4). To this, DBCO-NHS ester (150 µL, 100 mM in dimethylformamide) was added. The resulting dispersion was briefly sonicated and incubated overnight at 25 °C in a ThermoMixer C with shaking at 1000 rpm. The DBCO-modified silica-encapsulated iron oxide nanoparticles were purified by centrifugation (17,000 x *g*, 10 min) followed by three washes in ethanol, and then stored in ethanol at 4 °C and in a concentration of 5 mg mL^{-1}.

6.3.4. Synthesis of 2-azidoacetic acid NHS ester

2-azidoacetic acid (0.185 ml, 2.475 mmol), *N*-hydroxysuccinimide (0.3395 g, 2.965 mmol) and dicyclohexylcarbodiimide (0.6111 g, 2.965 mmol) were added to a 50 mL round-bottom

flask suspended in an ice bath, followed by the addition of dichloromethane (2.6 mL). The reaction was then magnetically stirred for 3 h at 500 rpm. After 3 h, the reaction mixture was diluted with ethyl acetate (EtOAc) and the precipitate filtered off. The filtrate was reduced *in vacuo* and purified using flash column chromatography and petroleum ether (PE) and ethyl acetate (3:1 PE:EtOAc – 2:1 PE:EtOAc – 1:1 PE:EtOAc). The tubes, in which the product crystallised out, were combined, the solvent removed and dissolved in a minimal amount of EtOAc. The desired compound was then precipitated from solution by addition of PE. It was then filtered off, washed with PE and dried to yield 2-azidoacetic acid NHS ester as a white, crystalline solid (118.5 mg, 0.60 mmol, 24%). The compound was then stored under Argon at -20 °C [155].

^{1}H-NMR (400 MHz, $CDCl_3$) δ/ppm 4.17 (s, 2H, Ac-CH_2), 2.81 (s, 4H, NHS-CH_2).

6.3.5. Modification of DNA with the azide click-handle

Water (15 µl), sodium bicarbonate ($NaHCO_3$) (5 µl, 1 M), 5′-amino modified C6 DNA with the sequence 5′-[AmC6]-GTGCTGCTTCATGTGGTC-3′ (reverse compliment of the ASO sequence) (5 µl, 200 µM) and 2-azidoacetic acid NHS ester (25 µl, 50 mM) were pipetted into a centrifuge tube. The reaction was vortexed and left to react for 4 h in an Eppendorf ThermoMixer® C at 300 rpm. The resulting DNA was purified through Amicon ultrafiltration 3K and stored at -20 °C.

6.3.6. Annealing and formation of the dsDNA

The 5′-azide-modified reverse compliment of the ASO was annealed to the ASO sequence in equimolar concentrations (240 µM) in water prior to heating at 95 °C for 5 min (and cooling to room temperature over the course of 1 h) and analysis by PAGE. A native 16% (v/v) PAGE was set-up at a 5 mL scale containing 40% (w/v)

acrylamide/bisacrylamide solution (2 mL), 10X Tris-Borate-EDTA (TBE) buffer (0.5 mL), water (2.5 mL), ammonium persulfate (40 µL, 10% w/v) and TEMED (2.5 µL). The reaction was briefly vortexed and left to set for 30 min. The samples were prepared by mixing the DNA (180 ng for ssDNA and 90 ng for dsDNA, 10 µL) in Native Loading Dye (2X, 10 µL). Gels were run with 1X TBE buffer at 250 V for 40 min and then stained in 3X Gel Red for 10 min. Gels were imaged using Azure 200 Gel Imager (Azure Biosystems).

6.3.7. Freeze-directed synthesis of SNAs

DBCO-modified silica-encapsulated iron oxide nanoparticles (5 mg mL^{-1}, 50 µL) were dispersed in water (395.9 µL) via addition of sodium chloride (300 mM, 37.50 µL of 4 M stock solution) and sonication of the resulting dispersion. Azide-modified dsDNA or amine-modified dsDNA (3 µM, 16.6 µL of 90.55 µM stock solution) was then added to the sonicated dispersion and the reaction was vortexed for several seconds. The reaction was then maintained at -7 °C for 4 h (using an Optima LTC4R refrigerated bath, *Grant* Instruments) and then placed in the freezer overnight at -20 °C before thawing at 4 °C for 1 h [156]. The resulting DNA-modified silica-encapsulated iron oxide nanoparticles (magnetically-activated SNAs) were purified by centrifugation at 17,000 x *g* for 13 min. The pellet was redissolved in a minimal volume of water (<30 µL). This process was repeated three times and the resulting magnetically-activated SNAs were stored at 4 °C in Milli-Q water.

6.3.8. RNase H assay

The 5X buffer (150 mM HEPES, 500 mM KCl, 100 mM $MgCl_2$, 10 mM dithiothreitol) was prepared in advance and stored at -20 °C. A reaction volume of 10 µL was prepared, comprising mVenus mRNA (0.22 µL, 1359 ng/µL for a final concentration of 30 ng/µL), 5X buffer (2.00 µL, 5X for a final concentration of 1X), RNase H enzyme (1.50 µL, 4 U/µL

for a final concentration of 0.6 U/μL), ASO or magnetically-activated SNA (0.40 μL, 5 ng/μL for a final concentration of 0.2 ng/μL), and Milli-Q water (5.88 μL). For the negative control, the ASO was replaced with an equivalent volume Milli-Q water. The reactions were incubated at 37 °C for 1 h. A 1.5% (w/v) TBE agarose gel was prepared by dissolving LE agarose (0.75 g) in 3X Gel Red (17 mL), 10X TBE buffer (5 mL) and water (28 mL) in the microwave (mid-high at intervals of 20 s). The gel was left to set for 30 min. The ssRNA ladder (NEB) was prepared by mixing 2 μL with water (8 μL). RNA loading dye (2X) was added in equal parts to all samples (10 μL) and the reactions (and RNase H) was denatured by heating to 70 °C for 10 min. The samples were loaded into the wells of the gel and exposed to 110 V for 40 min, following which they were imaged using Azure 200 Gel Imager (Azure Biosystems).

6.3.9. Strain-promoted azide-alkyne click chemistry synthesis of SNAs

6.3.9.1. TWEEN®20

DBCO-modified silica-encapsulated iron oxide nanoparticles (2.5 mg mL^{-1}, 185 μL) were dispersed in 0.01 M PBS buffer with 0.05% TWEEN®20 (183.9 μL) by brief sonication. To this, azide-modified dsDNA (0.1 μM, 1.5 μL of 25 μM stock solution) was added and the reaction was vortexed for several seconds. A control reaction was set-up with amine-modified dsDNA (1 μM, 1.5 μL of 25 μM stock solution). The reactions were left to react for overnight in an Eppendorf ThermoMixer® C at 800 rpm. The magnetically-activated SNAs were pelleted by centrifugation at 17,000 x *g* for 13 min and dissolved in Milli-Q water. This process was repeated three times and the resulting magnetically-activated SNAs were stored at 4 °C in Milli-Q water.

6.3.9.2. Ranging NaCl concentration and MOPS concentration

DBCO-modified silica-encapsulated iron oxide nanoparticles (15 mg mL^{-1}, 10 µL) were re-dispersed in MOPS buffer (0.1 M, pH 7.4) and NaCl (0.5 M) by pelletising at 17,000 x *g* for 13 min and dissolving in in the MOPS/NaCl buffer stock (10 µL). The resulting dispersion was sonicated briefly. Azide-modified dsDNA (21.1 µM, 20 µL of 31.6 µM stock solution) was then added, and the reaction was vortexed for several seconds. A control reaction was set-up with amine-modified dsDNA (6.32 µL of 100 µM stock solution and 13.68 µL of respective buffer). The reactions were left to react for overnight in an Eppendorf ThermoMixer® C at 800 rpm. The magnetically-activated SNAs were pelleted by centrifugation at 17,000 x *g* for 13 min and dissolved in water. This process was repeated three times and the resulting magnetically-activated SNAs were stored at 4 °C in water.

To access the ranging concentrations of MOPS and NaCl, a range of stock solutions of MOPS/NaCl were prepared according to the tables below.

Table 6.1. Preparation of MOPS buffer stock concentrations.

MOPS Buffer Concentration (M)	Mass of MOPS (g)	Volume (ml)
0.5	1.57	15
0.1	0.31	15
0.1	0.31	15

Table 6.2. Preparation of MOPS buffer stock concentrations with additional NaCl.

NaCl Concentration (M)	Mass of NaCl (g)	MOPS buffer concentration (M)	Volume of MOPS buffer (ml)
0.5	0.029	0.5	1
0.75	0.044	0.1	1
1	0.058	0.1	1

6.3.9.3. Heating in TE buffer

DBCO-modified silica-encapsulated iron oxide nanoparticles (15 mg mL^{-1}, 10 µL) were re-dispersed in TE buffer (10 mM Tris-HCl, 1 mM EDTA, pH 8) by pelletising at 17,000 x *g* for 13 min and dissolving in TE buffer (10 µL), followed by a brief sonication. Azide-modified dsDNA (21.1 µM, 20 µL of 31.6 µM stock solution) was then added and the reaction was vortexed for several seconds. A control reaction was set-up with amine-modified dsDNA (6.32 µL of 100 µM stock solution and 13.68 µL of respective buffer). The reactions were left to react overnight in an Eppendorf ThermoMixer® C at 800 rpm. The magnetically-activated SNAs were pelleted by centrifugation at 17,000 x *g* for 13 min and dissolved in TE buffer. This washing process was repeated three times and the resulting magnetically-activated SNAs were stored at 4 °C in TE buffer.

The magnetically-activated SNAs (with azide and amine-modified dsDNA) (suspended in TE buffer) were heated at 55 °C for 5 min with shaking in an Eppendorf ThermoMixer® C at 800 rpm. The magnetically-activated SNAs were then pelleted by centrifugation at 17,000 x *g* for 13 min and dissolved in water. This process was repeated three times and the resulting magnetically-activated SNAs were stored at 4 °C in water.

6.3.10. Salt-aging synthesis of SNAs

An NaCl stock solution at 2 M was prepared (0.2338 g, 2 ml) in water. DBCO-modified silica-encapsulated iron oxide nanoparticles (2.5 mg mL^{-1}, 185 µL) were dispersed in 0.05% TWEEN®20 (183.9 µL) by brief sonication. To this, azide-modified dsDNA or amine-modified dsDNA (0.1 µM, 1.5 µL of 25 µM stock solution) was added and the reaction was vortexed for several seconds. The NaCl concentration was slowly increased by adding a volume of 2 M NaCl stock every 20 minutes as follows: 9.3 µL of 2M NaCl was added at t = 20 min to give an NaCl concentration of 0.05 M; 9.7 µL of 2M NaCl was added at

t = 40 min to give an NaCl concentration of 0.10 M; 20.0 μL of 2M NaCl was added at *t* = 1 h to give an NaCl concentration of 0.20 M; 22.5 μL of 2M NaCl was added at *t* = 1 h 20 min to give an NaCl concentration of 0.30 M; 25.0 μL of 2M NaCl was added at *t* = 1 h 40 min to give an NaCl concentration of 0.40 M; 27.8 μL of 2M NaCl was added at *t* = 2 h to give an NaCl concentration of 0.50 M; 31.2 μL of 2M NaCl was added at *t* = 2 h 20 min to give an NaCl concentration of 0.60 M; 35.1 μL of 2M NaCl was added at *t* = 2 h 40 min to give an NaCl concentration of 0.70 M; 39.8 μL of 2M NaCl was added at *t* = 3 h to give an NaCl concentration of 0.80 M; 45.5 μL of 2M NaCl was added at *t* = 3 h 20 min to give an NaCl concentration of 0.90 M; 52.3 μL of 2M NaCl was added at *t* = 3 h 40 min to give an NaCl concentration of 1.00 M. The reaction was left to react overnight in an Eppendorf ThermoMixer® C at 800 rpm. The magnetically-activated SNAs were pelleted by centrifugation at 17,000 x *g* for 13 min and dissolved in water. This process was repeated three times and the resulting magnetically-activated SNAs were stored at 4 °C in water.

6.3.11. Agarose gel purification of SNAs

The magnetically-activated SNAs were purified by agarose gel electrophoresis, during which 6X purple loading dye (5 μL) was added and the reaction briefly vortexed. A 1.5% (w/v) TBE agarose gel was prepared by dissolving LE agarose (0.75 g) in 3X Gel Red (17 mL), 10X TBE buffer (5 mL) and water (28 mL) in a microwave oven (mid-high at intervals of 20 s until the LE agarose was dissolved). The gel was left to set for 30 min before the aforementioned magnetically-activated SNAs were loaded into the wells and the gel was exposed to 110 V for 20 min to pull off any non-covalently bound dsDNA. The well with the magnetically-activated SNAs was excised and briefly sonicated to release the purified SNAs. The purified, magnetically-activated SNAs were pelleted by centrifugation at

17,000 x *g* for 13 min and dissolved in Milli-Q water. The magnetically-activated SNAs were stored in Milli-Q water at 4 °C.

6.3.12. Magnetic control of gene knockdown

The 5X buffer (150 mM HEPES, 500 mM KCl, 100 mM $MgCl_2$, 10 mM dithiothreitol) was prepared in advance and stored at -20 °C. Reaction volumes of 10 µL were prepared, comprising mVenus mRNA (0.22 µL, 1359 ng/µL for a final concentration of 30 ng/µL), 5X buffer (2.00 µL, 5X for a final concentration of 1X), RNase H enzyme (1.50 µL, 4 U/µL for a final concentration of 0.6 U/µL), ASO or purified magnetically-activated SNA (0.40 µL, 5 ng/µL for a final concentration of 0.2 ng/µL), and water (5.88 µL). For the negative control, the ASO was replaced with an equivalent volume of Milli-Q water. One of the reactions with the purified magnetically-activated SNAs present was exposed to an AMF (magnetic fields strength of 30 mT and a magnetic excitation frequency of 103.4 kHz) using the NAN201003 Magnetherm (Nanotherics Ltd) with an 18-turn coil of 50 mm internal diameter for 90 min. The reactions were then all incubated at 37 °C in a thermal cycler for 1 h. A 1.5% (w/v) TBE agarose gel was prepared by dissolving LE agarose (0.75 g) in 3X Gel Red (17 mL), 10X TBE buffer (5 mL) and water (28 mL) in the microwave (mid-high at intervals of 20 s). The gel was left to set for 30 min. The ssRNA ladder (NEB) was prepared by mixing 2 µL with water (8 µL). RNA loading dye (2X) was added in equal parts to all samples (10 µL) and the reactions (and RNase H) was denatured by heating to 70 °C for 10 min. The samples were loaded into the wells of the gel and run for 40 min at 110 V and imaged using Azure 200 Gel Imager (Azure Biosystems).

6.4. Chapter 3 methods

6.4.1. Modification of the T7 promoter "bottom" strand

A mixture of water (15 µl), $NaHCO_3$ (5 µl, 1 M), 5′-amino modified C6 DNA with the sequence 5′-[AmC6]-CTATAGTGAGTCGTATTAATTTC-3′ (reverse compliment of the T7 promoter sequence) (5 µl, 200 µM) and 2-azidoacetic acid NHS ester (25 µl, 50 mM) was pipetted into a centrifuge tube. The reaction was vortexed and left to react for 4 h in an Eppendorf ThermoMixer® C at 300 rpm. The resulting DNA was purified through Amicon ultrafiltration 3K and stored at -20 °C.

6.4.2. Annealing and formation of the dsDNA T7 promoter

The 5′-azide-modified reverse compliment of the T7 promoter was annealed to the T7 promoter sequence in equimolar concentrations prior to heating at 95 °C for 5 min, followed by cooling to room temperature over the course of 1 h and then analysis by PAGE. A native 16% (v/v) PAGE was set-up at a 5 mL scale containing 40% (w/v) acrylamide/bisacrylamide solution (2 mL), 10X TBE buffer (0.5 mL), water (2.5 mL), ammonium persulfate (40 µL, 10% w/v) and TEMED (2.5 µL). The reaction was briefly vortexed and left to set for 30 min. The samples were prepared by mixing the DNA (180 ng for ssDNA and 90 ng for dsDNA, 10 µL) in Native Loading Dye (2X, 10 µL). Gels were run with 1X TBE buffer at 250 V for 40 min and then stained in 3X Gel Red for 10 min. Gels were imaged using Azure 200 Gel Imager (Azure Biosystems).

6.4.3. Freeze-directed synthesis of SNAs

DBCO-modified, silica-encapsulated iron oxide nanoparticles (5 mg mL^{-1}, 50 µL) were dispersed in water (395.9 µL). Sodium chloride was added (300 mM, 37.50 µL of 4 M stock solution) and the resulting dispersion was sonicated briefly. Azide-modified dsDNA (3 µM,

16.6 μL of 90.55 μM stock solution) was then added and the reaction was vortexed for several seconds. The reaction was then cooled for 4 h at -7 °C (Optima LTC4R refrigerated bath, *Grant* Instruments) and stored the freezer overnight at -20 °C before thawing via exposure to 4 °C [156]. The resulting DNA-modified silica-encapsulated iron oxide nanoparticles (magnetically-activated SNAs) were pelletised by centrifugation at 17,000 x *g* for 13 min following which the pellets were dissolved in water (<30 μL). This process was repeated three times and the resulting magnetically-activated SNAs were stored at 4 °C in water. The resulting magnetically-activated SNAs (T7 promoter-bound) were pelletised by centrifugation at 17,000 x *g* for 13 min. The pellets were dissolved in water (<30 μL), following which the magnetically-activated SNAs were purified by agarose gel electrophoresis, whereby 6X purple loading dye (5 μL) was added and the reaction briefly vortexed. A 1.5% (w/v) TBE agarose gel was prepared by dissolving LE agarose (0.75 g) in 3X Gel Red (17 mL), 10X TBE buffer (5 mL) and water (28 mL) in the microwave (mid-high at intervals of 20 s). The gel was left to set for 30 min before the aforementioned magnetically-activated SNAs were loaded into the wells and the gel was exposed to 110 v for 20 min to pull off any non-covalently bound azide-modified dsDNA T7 promoter. The well with the magnetically-activated SNAs was excised and briefly sonicated to release the purified SNAs. The purified magnetically-activated SNAs were pelleted by centrifugation at 17,000 x *g* for 13 min and dissolved in water. The magnetically-activated SNAs were stored in Milli-Q water at 4 °C.

6.4.4. In-vitro transcription assay

A stock solution of the inactive DNA template (negative control) was made up by mixing the non-template strand with the T7 promoter present (2 μM) and the coding strand with the T7 promoter missing (2 μM). A stock solution of the full DNA template (positive control)

was made up by mixing equal volumes of the non-template strand with the T7 promoter present (2 μM), the coding strand with the T7 promoter missing (2 μM), and the T7 promoter "top" strand (2 μM). In a similar manner, the magnetically-activated SNA was incorporated into a stock solution containing equal volumes of the non-template strand with the T7 promoter present (2 μM), the coding strand with the T7 promoter missing (2 μM), and the magnetically-activated SNA (equivalent ssDNA T7 promoter "top" strand loading of 2 μM).

Reactions of 10 μL were made up according to the HiScribe® T7 High Yield RNA Synthesis Kit with IVT buffer (10X, 1 μL), ATP (100 mM, 1 μL, GTP (100 mM, 1 μL), UTP (100 mM, 1 μL), CTP (100 mM, 1 μL), dithiothreitol (100 mM, 1 μL), KCl (1 M, 0.5 μL), DFHBI (600 μM, 1 μL), and T7 RNAP (1 μL). The "no template" sample had added water (1.5 μL). The "inactive template" sample had the inactive DNA template (0.57 μL) and water (0.93 μL). The "full template" sample had the full DNA template with the T7 promoter "top" strand (0.57 μL) and water (0.93 μL). The "SNA" sample had the full DNA template with the magnetically-activated SNA (0.57 μL) and water (0.93 μL). The reactions with DBCO-modified IONPs@SiO_2 present had 0.30 μL (1.5 mg ml^{-1}) with water 0.93 μL (in replacement of solely water). The in-vitro transcription (IVT) was run at 37 °C in the thermal cycler for 3 h. The reactions were diluted with 10 μL of water and transferred to Perkin Elmer 384-well black flat-bottom OptiPlates. Fluorescence was measured using a Tecan Spark fluorescence plate reader (Tecan Group Ltd) (bandwidth, 5 nm; z position, 19,681 μm; ExDFHBI, 472 nm; EmDFHBI, 507 nm).

6.4.5. Synthesis of the inactive DNA template

DreamTaq MM (2X) (60 μL) was mixed with phosphorylated T7 forward primer or -T7 forward primer (2.4 μL, 25 μM), CT-rev or phosphorylated CT-rev respectively (2.4 μL, 25 μM), mNG PURExpress control template plasmid [52] (1.2 μL, 2 ng/μL) and water

(54 µL). Reactions were thermally cycled according to the following program using a ProFlex PCR System (ThermoFisher): 95 °C dwell for 60 s, followed by 35 cycles of (95 °C for 30 s, 49 °C for 30 s and 72 °C for 65 s), followed by 72 °C for 10 min, and finally a dwell (HOLD) at 4 °C. All PCR products were validated by 1.5% (w/v) TBE agarose gel electrophoresis and purified using a Monarch PCR & DNA Cleanup Kit NEB.

The double stranded mNG template with the dsDNA T7 promoter region (1000 ng, 10.66 µL) or the double stranded mNG template without the dsDNA T7 promoter region (1000 ng, 10.66 µL) were diluted with water (11.34 µL). Lambda exonuclease (0.5 µL) and lambda exonuclease reaction buffer (10X, 2.5 µL) was added to a final volume of 25 µL. The reaction was allowed to proceed at 37 °C for 30 min (template without the dsDNA T7 promoter) and 35 min (template with the dsDNA T7 promoter) before the lambda exonuclease was denatured at 70 °C for 10 min. The crude reaction mixtures were combined and annealed at 95 °C for 5 min (before slow cooling to room temperature). The resulting inactive mNG template was purified by Monarch PCR & DNA Cleanup Kit NEB and the purity was validated by 1.5% (w/v) TBE agarose gel electrophoresis.

6.4.6. Bulk cell-free protein synthesis of mNG

Cell-free protein synthesis reactions (3 µL) were prepared with PURExpress Solution A (1.2 µL), PURExpress Solution B (0.9 µL) and supplemented with murine RNase inhibitor (0.075 µL). Inactive mNG template (5 ng μL^{-1}, 0.30 µL) and water (0.52 µL) were added for the negative control, full mNG template (with the dsDNA T7 promoter present) (5 ng μL^{-1}, 0.30 µL) and water (0.52 µL) were added for the positive control, and, for the magnetically-activated SNA samples, inactive mNG template (5 ng μL^{-1}, 0.30 µL), magnetically-activated SNAs (200 nM, 0.30 µL) and water (0.22 µL) were added. If necessary, the reactions were exposed to an alternating magnetic field (103.4 kHz, 30 mT) for 25 min and

left for a further 25 min at ambient temperature. All reactions were then incubated for 3 h in a thermal cycler at 25 °C and diluted with 17 μL of water. Reactions were transferred to black Perkin Elmer 384-well flat-bottom OptiPlates. Fluorescence was measured using a Tecan Spark fluorescence plate reader (Tecan Group Ltd) (bandwidth, 5 nm; z position, 17,764 μm; ExmNG, 495 nm; EmmNG, 517 nm).

Control CFPS reactions were carried out with the same protocol but the magnetically-activated SNAs were replaced with dsDNA T7 promoter (200 nM, 0.30 μL). Similarly, in the control with DBCO-modified IONPs@SiO_2 present (free in solution), SNAs were replaced with dsDNA T7 promoter (200 nM, 0.30 μL) and additional DBCO-modified IONPs@SiO_2 were added (1.5 mg/ml, 0.30 μL).

6.5. Chapter 4 methods

6.5.1. Synthesis of the inactive DNA template encoding α-HL

The inactive α-HL template was synthesised using the same protocol described in Section 6.4.5 but with a PURExpress control template plasmid encoding the α-HL protein.

6.5.2. Assembly of synthetic cells (both mNG- and α-HL-expressing)

Egg PC dissolved in chloroform (25 mg mL^{-1}, 150 μL) was transferred to a 2 mL glass vial (per two experimental conditions). The vials were tilted 45° and rotated slowly while held under N_2 flow to distribute the lipids evenly up the walls. The vials were then held under a vacuum for 3 h to remove residual chloroform. Mineral oil (filtered through a 0.22 μm PES membrane) was added to the Egg PC films (0.647 g) to give a final concentration of 5 mg mL^{-1} Egg PC. Vials were vortexed for 1 min and then incubated in the oven at 80 °C for 10 min with the lids removed. The vials had their lids reapplied and sealed tightly using Teflon tape and parafilm. They were then vortexed aggressively for 1 min and sonicated in

a sonication bath for 1 h at 50 °C. Lipid-containing oil was stored at room temperature overnight and vortexed, then sonicated for 10 min at room temperature immediately before use. A total of 250 μL of 5 mg mL^{-1} Egg PC in mineral oil was transferred to 1.5 mL centrifuge tubes and placed on ice. A total of 10 μL inner solution (PURExpress containing 5 ng μL^{-1} inactive mNG template or full mNG template, 400 nM magnetically-activated SNAs (as measured by calibration curve), 1.0 U μL^{-1} murine RNase inhibitor, 25 μM TXR-dextran (10 kDa) and 200 mM sucrose) was added into the chilled lipid-containing oil, ensuring the tip was constantly moved through the lipid-containing oil to disperse the inner solution. Tubes were passed across a centrifuge rack once using light pressure to form cloudy water-in-oil (w/o) emulsions. Meanwhile, 100 μL of lipid-containing oil was layered on top of 250 μL of chilled outer solution (50 mM HEPES, 400 mM potassium glutamate and 200 mM glucose (pH 7.6)) and placed at room temperature. w/o emulsions were then added on top of this oil phase, and this tube was left at room temperature for 1 min. Centrifuge tubes containing the w/o emulsion above the outer solution were centrifuged at 16,000 x *g* and 4 °C, for 30 min. After centrifugation, the oil phase and ~200 μL of the outer solution were removed from the tube and discarded. Using a fresh tip, ~10 μL of the remaining outer solution was ejected against the GUV pellet to displace it from the tube, and the intact GUV pellet was transferred to a new tube containing 250 μL outer solution. The pellet was subsequently resuspended by gently pipetting up and down. Vesicles were centrifuged at 10,000 x *g* and 4 °C for 10 min, then the outer solution was removed and the pellets were gently suspended in 25 μL of fresh outer solution [52].

The α-HL-containing synthetic cells were assembled using the same protocol, but instead the inner solution consisted of PURExpress containing 5 ng μL^{-1} inactive α-HL template or full α-HL template, 400 nM magnetically-activated SNAs (as measured by calibration

curve), 1.0 U μL^{-1} murine RNase inhibitor, 25 μM TR-dextran (10 kDa), 250 μM 2-NBDG and 200 mM sucrose.

6.5.3. Magnetic-activation of synthetic cells (both mNG- and α-HL-expressing)

To assess mNG expression from inside the synthetic cells, the GUV pellets were suspended in 25 μL outer solution and placed in colourless or black (opaque) microcentrifuge tubes. If necessary, the synthetic cells were exposed to an alternating magnetic field (103.4 kHz, 30 mT) for 10 min and left for a further 10 min at room temperature. All reactions were then incubated in a thermal cycler at 25 °C for 2.5 h and worked up with 25 μL of outer solution (50 mM HEPES, 400 mM potassium glutamate and 200 mM glucose (pH 7.6)). Fluorescence microscopy was performed using an EVOSÒ FL Fluorescence Microscope using a ×100 oil immersion objective lens. GUVs were imaged using the brightfield, TXR and GFP filters.

The synthesis of the α-HL pore-forming protein, its insertion in the lipid membrane, and the release of the 2-NBDG small molecule was assessed by resuspending the GUV pellets in 50 μL of outer solution and splitting each condition (inactive template, full template, and inactive template/magnetically-activated SNAs) into two centrifuge tubes. One centrifuge tube for each GUV sample (25 μL) was imaged for timepoint $t = 0$ h using an EVOSÒ FL Fluorescence Microscope (×100 oil immersion objective lens). GUVs were imaged using the brightfield, TXR and GFP filters. The other centrifuge tube for the sample containing the inactive template/magnetically-activated SNAs (25 μL) was exposed to an alternating magnetic field (103.4 kHz, 30 mT) for 10 min and left for a further 10 min at room temperature. All reactions (including the three $t = 0$ h samples and the sample exposed to an AMF) were then incubated in a thermal cycler for 4 h at 25 °C. The reactions were imaged

for timepoint $t = 4$ h using an EVOSÒ FL Fluorescence Microscope (×100 oil immersion objective lens).

The microscope settings for the TXR and GFP channels were kept constant across all images. The TXR and GFP channel brightness was adjusted and normalised across all images within a single experiment in Image J (an open-source platform: https://imagej.net/licensing/open-source), and then the separate channels were saved as individual PNG files. All images corresponding to a single sample were stored within the same directory. "Background" images were created by manually selecting vesicle-free regions of microscopy images (one from each sample within the experiment) and measuring the mean pixel intensity. PNG files were input into the vesicle_analysis script as described in previous literature (see Magnetic Activation of Spherical Nucleic Acids for the Remote Control of Synthetic Cells (Source data)) for script).

6.6. DNA Sequences

DNA name	DNA sequence	Modification
ASO sequence (top strand)	GACCACATGAAGCAGCAC	
ASO sequence (bottom strand)	GTGCTGCTTCATGTGGTC	5′-amine C6 modifier
mVenus DNA template	GAAATTAATACGACTCACTATAGGGTCTAG AAATAATTTTGTTTAACTTTAAGAAGGAGG TATACATATGGTGAGCAAGGGCGAGGAGCT GTTCACCGGGGTGGTGCCCATCCTGGTCGA GCTGGACGGCGACGTAAACGGCCACAAGTT CAGCGTGTCCGGCGAGGGCGAGGGCGATGC CACCTACGGCAAGCTGACCCTGAAGCTCAT CTGCACCACCGGCAAGCTGCCCGTGCCCTG GCCCACCCTCGTGACCACCCTCGGCTACGG CCTGCAGTGCTTCGCCCGCTACCCCGACCAC ATGAAGCAGCACGACTTCTTCAAGTCCGCC ATGCCCGAAGGCTACGTCCAGGAGCGCACC ATCTTCTTCAAGGACGACGGCAACTACAAG ACCCGCGCCGAGGTGAAGTTCGAGGGCGAC	

	ACCCTGGTGAACCGCATCGAGCTGAAGGGC ATCGACTTCAAGGAGGACGGCAACATCCTG GGGCACAAGCTGGAGTACAACTACAACAGC CACAACGTCTATATCACCGCCGACAAGCAG AAGAACGGCATCAAGGCCAACTTCAAGATC CGCCACAACATCGAGGACGGCGGCGTGCAG CTCGCCGACCACTACCAGCAGAACACCCCC ATCGGCGACGGCCCCGTGCTGCTGCCCGAC AACCACTACCTGAGCTACCAGTCCAAGCTG AGCAAAGACCCCAACGAGAAGCGCGATCA CATGGTCCTGCTGGAGTTCGTGACCGCCGC CGGGATCACTCTCGGCATGGACGAGCTGTA CAAGTAATGAGGATCCCGGGAATTCTCGAG TAAGGTTAACCTGCAGGAGGCCTTTAATTA AGGTGGTGCGGCCGCGCTAGCGGTCCCGGG GGATCGATCCGGCTGCTAACAAAGCCCGAA AGGAAGCTGAGTTGGCTGCTGCCACCGCTG AGCAATAACTAGCATAACCCCTTGGGGCCT CTAAACGGGTCTTGAGGGGTTTTTTGCTGAA AGGAGGAACTATATC	
DNA template encoding the Broccoli aptamer (non-template strand with the T7 promoter present)	GGGTCTAGGAGCCCACACTCTACTCGACAG ATACGAATATCTGGACCCGACCGTCTCCTA GACCCTATAGTGAGTCGTATTA	
DNA template encoding the Broccoli aptamer (coding strand with the T7 promoter missing)	TAGGAGACGGTCGGGTCCAGATATTCGTAT CTGTCGAGTAGAGTGTGGGCTCCTAGACCC	
T7 promoter sequence (top strand)	GAAATTAATACGACTCACTATAG	
T7 promoter sequence (bottom strand)	CTATAGTGAGTCGTATTAATTTC	5′-amine C6 modifier
-T7 forward primer (mNG)	GTTTAACTTTAAGAAGGAGGTATACATATG GTGAG	

Phosphorylated CT-Rev	GATATAGTTCCTCCTTTCAG	5′-phosphorylated
Phosphorylated T7 forward primer	GAAATTAATACGACTCACTATAGGGTCTAG	5′-phosphorylated
CT-Rev	GATATAGTTCCTCCTTTCAG	
mNG linear template	gaaattaatacgactcactatagggtctagaaataattttgtttaactttaag aaggaggtatacatATGGTGAGCAAAGGCGAAGAG GATAATATGGCAAGCCTGCCTGCAACACAT GAACTGCATATTTTTGGTAGCATTAACGGC GTGGATTTTGATATGGTTGGTCAAGGCACC GGTAATCCGAATGATGGTTATGAAGAACTG AATCTGAAAAGCACCAAAGGCGATCTGCAG TTTAGCCCGTGGATTCTGGTTCCGCATATTG GTTATGGTTTTCATCAGTATCTGCCGTATCC GGATGGTATGAGCCCGTTTCAGGCAGCAAT GGTTGATGGTAGCGGTTATCAGGTTCATCGT ACCATGCAGTTTGAAGATGGTGCAAGCCTG ACCGTTAATTATCGTTATACCTATGAAGGCA GCCACATTAAAGGTGAAGCACAGGTTAAAG GTACAGGTTTTCCGGCAGATGGTCCGGTTAT GACCAATAGTCTGACCGCAGCAGATTGGTG TCGTAGCAAAAAAACCTATCCGAACGATAA AACCATCATCAGCACCTTCAAATGGTCATA TACCACCGGCAATGGTAAACGTTATCGTAG CACCGCACGTACCACCTATACCTTTGCAAA ACCGATGGCAGCAAACTATCTGAAAAATCA GCCGATGTATGTGTTTCGCAAAACGGAACT GAAACATTCCAAAACCGAGCTGAACTTTAA AGAATGGCAGAAAGCATTTACCGATGTGAT GGGTATGGATGAGCTGTACAAATAATGAgga tcccgggaattctcgagtaaggttaacctgcaggaggcctttaattaagg tggtgcggccgcgctagcggtcccgggggatcgatccggctgctaac aaagcccgaaaggaagctgagttggctgctgccaccgctgagcaataa ctagcataacccctttggggcctctaaacgggtcttgaggggtttttgctg aaaggaggaactatatc	
α-HL linear template	TAATACGACTCACTATAGGGTCTAGAAATA ATTTTGTTTAACTTTAAGAAGGAGGTATACA TATGGCAGATTCTGATATTAATATTAAAACC GGTACTACAGATATTGGAAGCAATACTACA GTAAAAACAGGTGATTTAGTCACTTATGAT AAAGAAAATGGCATGCACAAAAAAGTATTT TATAGTTTTATCGATGATAAAAATCACAAT	

	AAAAAACTGCTAGTTATTAGAACAAAAGGT ACCATTGCTGGTCAATATAGAGTTTATAGC GAAGAAGGTGCTAACAAAAGTGGTTTAGCC TGGCCTTCAGCCTTTAAGGTACAGTTGCAAC TACCTGATAATGAAGTAGCTCAAATATCTG ATTACTATCCAAGAAATTCGATTGATACAA AAAACTATATGAGTACTTTAACTTATGGATT CAACGGTAATGTTACTGGTGATGATACAGG AAAAATTGGCGGCCTTATTGGTGCAAATGT TTCGATTGGTCATACACTGAACTATGTTCAA CCTGATTTCAAAACAATTTTAGAGAGCCCA ACTGATAAAAAAGTAGGCTGGAAAGTGATA TTTAACAATATGGTGAATCAAAATTGGGGA CCATACGATCGAGATTCTTGGAACCCGGTA TATGGCAATCAACTTTTCATGAAAACTAGA AATGGTTCTATGAAAGCAGCAGATAACTTC CTTGATCCTAACAAAGCAAGTTCTCTATTAT CTTCAGGGTTTTCACCAGACTTCGCTACAGT TATTACTATGGATAGAAAAGCATCCAAACA ACAAACAAATATAGATGTAATATACGAACG AGTTCGTGATGATTACCAATTGCATTGGACT TCAACAAATTGGAAAGGTACCAATACTAAA GATAAATGGACAGATCGTTCTTCAGAAAGA TATAAAATCGATTGGGAAAAAGAAGAAATG ACAAATTAATGAGGATCCCGGGAATTCTCG AGTAAGGTTAACCTGCAGGAGGCCTTTAAT TAAGGTGGTGCGGCCGCGCTAGCGGTCCCG GGGGATCGATCCGGCTGCTAACAAAGCCCG AAAGGAAGCTGAGTTGGCTGCTGCCACCGC TGAGCAATAACTAGCATAACCCCTTGGGGC CTCTAAACGGGTCTTGAGGGGTTTTTTG	
-T7 forward primer (α-HL)	ATGGCAGATTCTGATATTAATATTAAAAC	

References

1. Minchin, S. & Lodge, J. Understanding biochemistry: structure and function of nucleic acids. *Essays Biochem.* **63**, 433–456 (2019).
2. Heinemann, U. & Roske, Y. Symmetry in Nucleic-Acid Double Helices. *Symmetry* **12**, 737-755 (2020).
3. Ekundayo, B. & Bleichert, F. Origins of DNA replication. *PLoS Genet.* **15**, e1008320 (2019).
4. Bedinger, P., Hochstrasser, M., Victor Jongeneel, C. & Alberts, B. M. Properties of the T4 bacteriophage DNA replication apparatus: The T4 dda DNA helicase is required to pass a bound RNA polymerase molecule. *Cell* **34**, 115–123 (1983).
5. García-Muse, T. & Aguilera, A. Transcription–replication conflicts: how they occur and how they are resolved. *Nat. Rev. Mol. Cell Biol.* **17**, 553–563 (2016).
6. Cooper, G. M. DNA Replication. in *The Cell: A Molecular Approach. 2nd edition* (Sinauer Associates, 2000).
7. Song, H., Shen, R., Mahasin, H., Guo, Y. & Wang, D. DNA replication: Mechanisms and therapeutic interventions for diseases. *MedComm (2020)* **4**, e210-243 (2023).
8. Baranello, L., Levens, D., Gupta, A. & Kouzine, F. The importance of being supercoiled: how DNA mechanics regulate dynamic processes. *Biochim. Biophys. Acta* **1819**, 632–638 (2012).
9. Nudler, E. RNA Polymerase Backtracking in Gene Regulation and Genome Instability. *Cell* **149**, 1438–1445 (2012).

10. Alberts, B. *et al.* From DNA to RNA. in *Molecular Biology of the Cell. 4th edition* (Garland Science, 2002).
11. Berg, M. D. & Brandl, C. J. Transfer RNAs: diversity in form and function. *RNA Biol.* **18**, 316–339 (2020).
12. Asano, K. Why is start codon selection so precise in eukaryotes? *Translation (Austin)* **2**, e28387 (2014).
13. Cooper, G. M. Translation of mRNA. in *The Cell: A Molecular Approach. 2nd edition* (Sinauer Associates, 2000).
14. Friedmann, T. & Roblin, R. Gene Therapy for Human Genetic Disease? *Science* **175**, 949–955 (1972).
15. Roberts, T. C., Langer, R. & Wood, M. J. A. Advances in oligonucleotide drug delivery. *Nat. Rev. Drug Discov.* **19**, 673–694 (2020).
16. Rinaldi, C. & Wood, M. J. A. Antisense oligonucleotides: the next frontier for treatment of neurological disorders. *Nat. Rev. Neurol.* **14**, 9–21 (2018).
17. Corbett, K. S. *et al.* SARS-CoV-2 mRNA vaccine design enabled by prototype pathogen preparedness. *Nature* **586**, 567–571 (2020).
18. Paunovska, K., Loughrey, D. & Dahlman, J. E. Drug delivery systems for RNA therapeutics. *Nat. Rev. Genet.* **23**, 265–280 (2022).
19. Crooke, S. T., Liang, X.-H., Baker, B. F. & Crooke, R. M. Antisense technology: A review. *JBC* **296**, 100416-100455 (2021).
20. Moccia, M. *et al.* Advances in Nucleic Acid Research: Exploring the Potential of Oligonucleotides for Therapeutic Applications and Biological Studies. *Int. J. Mol. Sci.* **25**, 146-166 (2023).
21. Yamada, Y. Nucleic Acid Drugs—Current Status, Issues, and Expectations for Exosomes. *Cancers (Basel)* **13**, 5002-5021 (2021).

22. Sun, X., Setrerrahmane, S., Li, C., Hu, J. & Xu, H. Nucleic acid drugs: recent progress and future perspectives. *Sig. Transduct. Target Ther.* **9**, 316-347 (2024).

23. Kulkarni, J. A. *et al.* The current landscape of nucleic acid therapeutics. *Nat. Nanotechnol.* **16**, 630–643 (2021).

24. Le, B. T. *et al.* Thiomorpholino oligonucleotides as a robust class of next generation platforms for alternate mRNA splicing. *PNAS* **119**, e2207956119 (2022).

25. Pradeep, S. P., Malik, S., Slack, F. J. & Bahal, R. Unlocking the potential of chemically modified peptide nucleic acids for RNA-based therapeutics. *RNA* **29**, 434–445 (2023).

26. Dhuri, K. *et al.* Antisense Oligonucleotides: An Emerging Area in Drug Discovery and Development. *J. Clin. Med.* **9**, 2004-2028 (2020).

27. Pradeep, S. P., Malik, S., Slack, F. J. & Bahal, R. Unlocking the potential of chemically modified peptide nucleic acids for RNA-based therapeutics. *RNA* **29**, 434–445 (2023).

28. Shen, X. & Corey, D. R. Chemistry, mechanism and clinical status of antisense oligonucleotides and duplex RNAs. *Nucleic Acids Res.* **46**, 1584–1600 (2018).

29. Deprey, K., Batistatou, N. & Kritzer, J. A. A critical analysis of methods used to investigate the cellular uptake and subcellular localization of RNA therapeutics. *Nucleic Acids Res.* **48**, 7623–7639 (2020).

30. Stein, C. A. *et al.* Efficient gene silencing by delivery of locked nucleic acid antisense oligonucleotides, unassisted by transfection reagents. *Nucleic Acids Res.* **38**, e3-11 (2010).

31. Breunig, M., Lungwitz, U., Liebl, R. & Goepferich, A. Breaking up the correlation between efficacy and toxicity for nonviral gene delivery. *Proc. Natl. Acad. Sci. USA* **104**, 14454–14459 (2007).

32. Egli, M. & Manoharan, M. Chemistry, structure and function of approved oligonucleotide therapeutics. *Nucleic Acids Res.* **51**, 2529–2573 (2023).

33. Springer, A. D. & Dowdy, S. F. GalNAc-siRNA Conjugates: Leading the Way for Delivery of RNAi Therapeutics. *Nucleic Acid Ther.* **28**, 109–118 (2018).

34. Kularatne, R. N., Crist, R. M. & Stern, S. T. The Future of Tissue-Targeted Lipid Nanoparticle-Mediated Nucleic Acid Delivery. *Pharmaceuticals* **15**, 897-914 (2022).

35. Mehta, M. *et al.* Lipid-Based Nanoparticles for Drug/Gene Delivery: An Overview of the Production Techniques and Difficulties Encountered in Their Industrial Development. *ACS Mater. Au* **3**, 600–619 (2023).

36. Hou, X., Zaks, T., Langer, R. & Dong, Y. Lipid nanoparticles for mRNA delivery. *Nat. Rev. Mater.* **6**, 1078–1094 (2021).

37. Chatterjee, S., Kon, E., Sharma, P. & Peer, D. Endosomal escape: A bottleneck for LNP-mediated therapeutics. *Proc. Natl. Acad Sci. USA* **121**, e2307800120 (2024).

38. Paunovska, K. *et al.* Analyzing 2000 in Vivo Drug Delivery Data Points Reveals Cholesterol Structure Impacts Nanoparticle Delivery. *ACS Nano* **12**, 8341–8349 (2018).

39. Suk, J. S., Xu, Q., Kim, N., Hanes, J. & Ensign, L. M. PEGylation as a strategy for improving nanoparticle-based drug and gene delivery. *Adv. Drug Deliv. Rev.* **99**, 28–51 (2016).

40. Chaudhary, N. *et al.* Amine headgroups in ionizable lipids drive immune responses to lipid nanoparticles by binding to the receptors TLR4 and CD1d. *Nat. Biomed. Eng.* **8**, 1483–1498 (2024).

41. Li, S. *et al.* Payload distribution and capacity of mRNA lipid nanoparticles. *Nat. Commun.* **13**, 5561-5574 (2022).

42. Cutler, J. I., Auyeung, E. & Mirkin, C. A. Spherical Nucleic Acids. *J. Am. Chem. Soc.* **134**, 1376–1391 (2012).

43. Choi, C. H. J., Hao, L., Narayan, S. P., Auyeung, E. & Mirkin, C. A. Mechanism for the endocytosis of spherical nucleic acid nanoparticle conjugates. *Proc. Natl. Acad. Sci. USA* **110**, 7625–7630 (2013).

44. Kapadia, C. H., Melamed, J. R. & Day, E. S. Spherical Nucleic Acid Nanoparticles: Therapeutic Potential. *BioDrugs* **32**, 297–309 (2018).

45. Cutler, J. I., Zheng, D., Xu, X., Giljohann, D. A. & Mirkin, C. A. Polyvalent Oligonucleotide Iron Oxide Nanoparticle "Click" Conjugates. *Nano Lett.* **10**, 1477–1480 (2010).

46. Zhang, K., Hao, L., Hurst, S. J. & Mirkin, C. A. Antibody-Linked Spherical Nucleic Acids for Cellular Targeting. *J. Am. Chem. Soc.* **134**, 16488–16491 (2012).

47. Xu, C., Hu, S. & Chen, X. Artificial cells: from basic science to applications. *Mater. Today (Kidlington)* **19**, 516–532 (2016).

48. Yan, X., Liu, X., Zhao, C. & Chen, G.-Q. Applications of synthetic biology in medical and pharmaceutical fields. *Sig. Transduct. Target Ther.* **8**, 1–33 (2023).

49. Waeterschoot, J., Gosselé, W., Lemež, Š. & Casadevall i Solvas, X. Artificial cells for in vivo biomedical applications through red blood cell biomimicry. *Nat. Commun.* **15**, 2504-2521 (2024).

50. Monck, C., Elani, Y. & Ceroni, F. Genetically programmed synthetic cells for thermo-responsive protein synthesis and cargo release. *Nat. Chem. Biol.* **20**, 1380-1386 (2024).

51. Guindani, C., da Silva, L. C., Cao, S., Ivanov, T. & Landfester, K. Synthetic Cells: From Simple Bio-Inspired Modules to Sophisticated Integrated Systems. *Angew. Chem. Int. Ed.* **61**, e202110855 (2022).

52. Smith, J. M., Hartmann, D. & Booth, M. J. Engineering cellular communication between light-activated synthetic cells and bacteria. *Nat. Chem. Biol.* **19**, 1138–1146 (2023).

53. Garenne, D. *et al.* Cell-free gene expression. *Nat. Rev. Methods Primers* **1**, 1–18 (2021).

54. Gregorio, N. E., Levine, M. Z. & Oza, J. P. A User's Guide to Cell-Free Protein Synthesis. *Methods Protoc.* **2**, 24-58 (2019).

55. Nirenberg, M. W. & Matthaei, J. H. The dependence of cell-free protein synthesis in E. coli upon naturally occurring or synthetic polyribonucleotides. *PNAS* **47**, 1588–1602 (1961).

56. Kim, J., Copeland, C. E., Seki, K., Vögeli, B. & Kwon, Y.-C. Tuning the Cell-Free Protein Synthesis System for Biomanufacturing of Monomeric Human Filaggrin. *Front Bioeng. Biotechnol.* **8**, 590341-590355 (2020).

57. Cui, Y., Chen, X., Wang, Z. & Lu, Y. Cell-Free PURE System: Evolution and Achievements. *Biodes. Res.* 9847014 (2022).

58. Kwon, Y.-C. & Jewett, M. C. High-throughput preparation methods of crude extract for robust cell-free protein synthesis. *Sci. Rep.* **5**, 8663-8674 (2015).

59. Cole, S. D. *et al.* Quantification of Interlaboratory Cell-Free Protein Synthesis Variability. *ACS Synth. Biol.* **8**, 2080–2091 (2019).

60. Shimizu, Y. *et al.* Cell-free translation reconstituted with purified components. *Nat. Biotechnol.* **19**, 751–755 (2001).

61. Kochetkov, S. n, Rusakova, E. e & Tunitskaya, V. l. Recent studies of T7 RNA polymerase mechanism. *FEBS Letters* **440**, 264–267 (1998).

62. Muller, D. K., Martin, C. T. & Coleman, J. E. T7 RNA polymerase interacts with its promoter from one side of the DNA helix. *Biochemistry* **28**, 3306–3313 (1989).

63. Maslak, M. & Martin, C. T. Kinetic analysis of T7 RNA polymerase transcription initiation from promoters containing single-stranded regions. *Biochemistry* **32**, 4281–4285 (1993).

64. Gonzales, D. T., Yandrapalli, N., Robinson, T., Zechner, C. & Tang, T.-Y. D. Cell-Free Gene Expression Dynamics in Synthetic Cell Populations. *ACS Synth. Biol.* **11**, 205–215 (2022).

65. Walde, P., Cosentino, K., Engel, H. & Stano, P. Giant Vesicles: Preparations and Applications. *Chem. Bio. Chem.* **11**, 848–865 (2010).

66. Baimanov, D., Cai, R. & Chen, C. Understanding the Chemical Nature of Nanoparticle–Protein Interactions. *Bioconjugate Chem.* **30**, 1923–1937 (2019).

67. Pattipeiluhu, R. *et al.* Unbiased Identification of the Liposome Protein Corona using Photoaffinity-based Chemoproteomics. *ACS Cent. Sci.* **6**, 535–545 (2020).

68. Giulimondi, F. *et al.* Interplay of protein corona and immune cells controls blood residency of liposomes. *Nat. Commun.* **10**, 3686-3697 (2019).

69. Sato, W., Zajkowski, T., Moser, F. & Adamala, K. P. Synthetic cells in biomedical applications. *WIREs Nanomedicine and Nanobiotechnology* **14**, e1761-1793 (2022).

70. Gabizon, A. *et al.* Prolonged Circulation Time and Enhanced Accumulation in Malignant Exudates of Doxorubicin Encapsulated in Polyethylene-glycol Coated Liposomes1. *Cancer Res.* **54**, 987–992 (1994).

71. Sercombe, L. *et al.* Advances and Challenges of Liposome Assisted Drug Delivery. *Front. Pharmacol.* **6**, 1-13 (2015).

72. Krinsky, N. *et al.* Synthetic Cells Synthesize Therapeutic Proteins inside Tumors. *Adv. Healthc. Mater.* **7**, 1701163 (2018).

73. Chen, Z. *et al.* Synthetic beta cells for fusion-mediated dynamic insulin secretion. *Nat. Chem. Biol.* **14**, 86–93 (2018).

74. Yang, C., Kong, L. & Zhang, Z. Bioreactor: Intelligent platform for drug delivery. *Nano Today* **44**, 101481 (2022).

75. Chen, G. *et al.* Implanted synthetic cells trigger tissue angiogenesis through de novo production of recombinant growth factors. *PNAS* **119**, e2207525119 (2022).

76. Diltemiz, S. E. *et al.* Use of artificial cells as drug carriers. *Mater. Chem. Front.* **5**, 6672–6692 (2021).

77. Martini, L. & Mansy, S. S. Cell-like systems with riboswitch controlled gene expression. *Chem. Commun.* **47**, 10734–10736 (2011).

78. Adamala, K. P., Martin-Alarcon, D. A., Guthrie-Honea, K. R. & Boyden, E. S. Engineering genetic circuit interactions within and between synthetic minimal cells. *Nat. Chem.* **9**, 431–439 (2017).

79. Dwidar, M. *et al.* Programmable Artificial Cells Using Histamine-Responsive Synthetic Riboswitch. *J. Am. Chem. Soc.* **141**, 11103–11114 (2019).

80. Sadler, F. W., Dodevski, I. & Sarkar, C. A. RNA thermometers for the PURExpress system. *ACS Synth. Biol.* **7**, 292–296 (2018).

81. Chowdhury, S., Maris, C., Allain, F. H.-T. & Narberhaus, F. Molecular basis for temperature sensing by an RNA thermometer. *EMBO J.* **25**, 2487–2497 (2006).

82. Zhang, K., Zhu, X., Jia, F., Auyeung, E. & Mirkin, C. A. Temperature-Activated Nucleic Acid Nanostructures. *J. Am. Chem. Soc.* **135**, 14102–14105 (2013).

83. Li, F., Gao, Q., Yang, M. & Guo, W. Regulation of Catalytic DNA Activities with Thermosensitive Gold Nanoparticle Surfaces. *Langmuir* **34**, 14932–14939 (2018).

84. Jia, H., Heymann, M., Härtel, T., Kai, L. & Schwille, P. Temperature-sensitive protein expression in protocells. *Chem. Commun.* **55**, 6421–6424 (2019).

85. Hartmann, D., Smith, J. M., Mazzotti, G., Chowdhry, R. & Booth, M. J. Controlling gene expression with light: a multidisciplinary endeavour. *Biochemical Society Transactions* **48**, 1645–1659 (2020).

86. Booth, M. J., Schild, V. R., Graham, A. D., Olof, S. N. & Bayley, H. Light-activated communication in synthetic tissues. *Sci. Adv.* **2**, e1600056 (2016).

87. Kalia, V. C. Quorum sensing inhibitors: An overview. *Biotechnology Advances* **31**, 224–245 (2013).

88. Hartmann, D. & Booth, M. J. Handcuffed antisense oligonucleotides for light-controlled cell-free expression. *Chem. Commun.* **59**, 5685–5688 (2023).

89. Hartmann, D. & Booth, M. J. Accessible light-controlled knockdown of cell-free protein synthesis using phosphorothioate-caged antisense oligonucleotides. *Commun. Chem.* **6**, 1–8 (2023).

90. Mazzotti, G., Hartmann, D. & Booth, M. J. Precise, Orthogonal Remote-Control of Cell-Free Systems Using Photocaged Nucleic Acids. *J. Am. Chem. Soc.* **145**, 9481–9487 (2023).

91. Smith, J. M., Chowdhry, R. & Booth, M. J. Controlling Synthetic Cell-Cell Communication. *Front. Mol. Biosci.* **8**, 1-9 (2022).

92. Ash, C., Dubec, M., Donne, K. & Bashford, T. Effect of wavelength and beam width on penetration in light-tissue interaction using computational methods. *Lasers Med. Sci.* **32**, 1909–1918 (2017).

93. Miranda, D. & Lovell, J. F. Mechanisms of light-induced liposome permeabilization. *Bioengineering & Translational Medicine* **1**, 267–276 (2016).

94. Zhang, P. *et al.* Near Infrared-Guided Smart Nanocarriers for MicroRNA-Controlled Release of Doxorubicin/siRNA with Intracellular ATP as Fuel. *ACS Nano* **10**, 3637–3647 (2016).

95. Derfus, A. M. *et al.* Remotely Triggered Release from Magnetic Nanoparticles. *Adv. Mater.* **19**, 3932–3936 (2007).

96. Chen, R., Canales, A. & Anikeeva, P. Neural Recording and Modulation Technologies. *Nat. Rev. Mater.* **2**, 16093-16109 (2017).

97. Mirvakili, S. M. & Langer, R. Wireless on-demand drug delivery. *Nat. Electron* **4**, 464–477 (2021).

98. Liu, X. *et al.* Comprehensive understanding of magnetic hyperthermia for improving antitumor therapeutic efficacy. *Theranostics* **10**, 3793–3815 (2020).

99. Norris, M. D., Seidel, K. & Kirschning, A. Externally Induced Drug Release Systems with Magnetic Nanoparticle Carriers: An Emerging Field in Nanomedicine. *Adv. Therapeutics* **2**, 1800092 (2019).

100. Pereira Gomes, I. *et al.* Thermosensitive Nanosystems Associated with Hyperthermia for Cancer Treatment. *Pharmaceuticals* **12**, 171-183 (2019).

101. Gavilán, H. *et al.* Magnetic nanoparticles and clusters for magnetic hyperthermia: optimizing their heat performance and developing combinatorial therapies to tackle cancer. *Chem. Soc. Rev.* **50**, 11614–11667 (2021).

102. Chang, D. *et al.* Biologically Targeted Magnetic Hyperthermia: Potential and Limitations. *Front. Pharmacol.* **9**, 831-851 (2018).

103. Pitt, W. G., Husseini, G. A. & Staples, B. J. Ultrasonic Drug Delivery – A General Review. *Expert Opin. Drug Deliv.* **1**, 37–56 (2004).

104. Saliev, T. & Akishev, M. Ultrasound binary microbubble drug delivery and drug synthesis for cancer treatment. *J. Anal. Sci. Tech.* **16**, 11-28 (2025).

105. Thapa, R. K. & Kim, J. O. Nanomedicine-based commercial formulations: current developments and future prospects. *J. Pharm. Investig.* **53**, 19–33 (2023).

106. Wei, H. *et al.* Exceedingly small iron oxide nanoparticles as positive MRI contrast agents. *Proc. Natl. Acad. Sci. USA* **114**, 2325–2330 (2017).

107. Vangijzegem, T. *et al.* Superparamagnetic Iron Oxide Nanoparticles (SPION): From Fundamentals to State-of-the-Art Innovative Applications for Cancer Therapy. *Pharmaceutics* **15**, 236-268 (2023).

108. Pucci, C., Degl'Innocenti, A., Gümüş, M. B. & Ciofani, G. Superparamagnetic iron oxide nanoparticles for magnetic hyperthermia: recent advancements, molecular effects, and future directions in the omics era. *Biomater. Sci.* **10**, 2103–2121 (2022).

109. Riedinger, A. *et al.* Subnanometer Local Temperature Probing and Remotely Controlled Drug Release Based on Azo-Functionalized Iron Oxide Nanoparticles. *Nano Lett.* **13**, 2399–2406 (2013).

110. Yu, L. *et al.* Evaluation of Hyperthermia of Magnetic Nanoparticles by Dehydrating DNA. *Sci. Rep.* **4**, 7216 (2014).

111. Dias, J. T. *et al.* DNA as a Molecular Local Thermal Probe for the Analysis of Magnetic Hyperthermia. *Angew. Chem. Int. Ed.* **52**, 11526–11529 (2013).

112. Luiz, M. T. *et al.* Hybrid Magnetic Lipid-Based Nanoparticles for Cancer Therapy. *Pharmaceutics* **15**, 751-772 (2023).

113. Theodosiou, M. *et al.* Iron oxide nanoflowers encapsulated in thermosensitive fluorescent liposomes for hyperthermia treatment of lung adenocarcinoma. *Sci. Rep.* **12**, 8697-8712 (2022).

114. Zhu, K. K. *et al.* Magnetic Modulation of Biochemical Synthesis in Synthetic Cells. *J. Am. Chem. Soc.* **146**, 13176–13182 (2024).

115. Atkinson, W. J., Brezovich, I. A. & Chakraborty, D. P. Usable Frequencies in Hyperthermia with Thermal Seeds. *IEEE Transactions on Biomedical Engineering*, **31**, 70–75 (1984).

116. Herrero de la Parte, B. *et al.* Proposal of New Safety Limits for In Vivo Experiments of Magnetic Hyperthermia Antitumor Therapy. *Cancers* **14**, 3084-3094 (2022).

117. Brezovich, I. A. Low frequency hyperthermia: capacitive and ferromagnetic thermoseed methods. *Med. Phys. Monogr.* **16**, 82–111 (1988).

118. Dutz, S. & Hergt, R. Magnetic nanoparticle heating and heat transfer on a microscale: Basic principles, realities and physical limitations of hyperthermia for tumour therapy. *Int. J. Hyperthermia* **29**, 790–800 (2013).

119. Giljohann, D. A., Seferos, D. S., Prigodich, A. E., Patel, P. C. & Mirkin, C. A. Gene Regulation with Polyvalent siRNA−Nanoparticle Conjugates. *J. Am. Chem. Soc.* **131**, 2072–2073 (2009).

120. Cutler, J. I. *et al.* Polyvalent Nucleic Acid Nanostructures. *J. Am. Chem. Soc.* **133**, 9254–9257 (2011).

121. Amendola, V., Pilot, R., Frasconi, M., Maragò, O. M. & Iatì, M. A. Surface plasmon resonance in gold nanoparticles: a review. *J. Phys. Condens. Matter* **29**, 203002 (2017).

122. Jin, R., Wu, G., Li, Z., Mirkin, C. A. & Schatz, G. C. What Controls the Melting Properties of DNA-Linked Gold Nanoparticle Assemblies? *J. Am. Chem. Soc.* **125**, 1643–1654 (2003).

123. Mitchell, G. P., Mirkin, C. A. & Letsinger, R. L. Programmed Assembly of DNA Functionalized Quantum Dots. *J. Am. Chem. Soc.* **121**, 8122–8123 (1999).

124. Young, K. L. *et al.* Hollow Spherical Nucleic Acids for Intracellular Gene Regulation Based upon Biocompatible Silica Shells. *Nano Lett.* **12**, 3867–3871 (2012).

125. Song, Y. *et al.* Multimodal Gadolinium-Enriched DNA–Gold Nanoparticle Conjugates for Cellular Imaging. *Angew. Chem. Int. Ed.* **48**, 9143–9147 (2009).

126. Giljohann, D. A. *et al.* Oligonucleotide Loading Determines Cellular Uptake of DNA-Modified Gold Nanoparticles. *Nano Lett.* **7**, 3818–3821 (2007).

127. Massich, M. D. *et al.* Regulating Immune Response Using Polyvalent Nucleic Acid−Gold Nanoparticle Conjugates. *Mol. Pharmaceutics* **6**, 1934–1940 (2009).

128. Kouri, F. M. *et al.* miR-182 integrates apoptosis, growth, and differentiation programs in glioblastoma. *Genes Dev.* **29**, 732–745 (2015).

129. Jensen, S. A. *et al.* Spherical nucleic acid nanoparticle conjugates as an RNAi-based therapy for glioblastoma. *Sci. Transl. Med.* **5**, 209ra152 (2013).

130. Randeria, P. S. *et al.* siRNA-based spherical nucleic acids reverse impaired wound healing in diabetic mice by ganglioside GM3 synthase knockdown. *Proc. Natl. Acad. Sci. USA* **112**, 5573–5578 (2015).

131. Lewandowski, K. T. *et al.* Topically Delivered Tumor Necrosis Factor-α–Targeted Gene Regulation for Psoriasis. *J. Invest. Dermatol.* **137**, 2027–2030 (2017).

132. Sun, G.-Y. *et al.* Terminal Deoxynucleotidyl Transferase-Catalyzed Preparation of pH-Responsive DNA Nanocarriers for Tumor-Targeted Drug Delivery and Therapy. *ACS Appl. Mater. Interfaces* **11**, 14684–14692 (2019).

133. Jain, K., Vedarajan, R., Watanabe, M., Ishikiriyama, M. & Matsumi, N. Tunable LCST behavior of poly(N-isopropylacrylamide/ionic liquid) copolymers. *Polym. Chem.* **6**, 6819–6825 (2015).

134. Karimi, M. *et al.* pH-Sensitive stimulus-responsive nanocarriers for targeted delivery of therapeutic agents. *Wiley Interdiscip. Rev. Nanomed. Nanobiotechnol.* **8**, 696–716 (2016).

135. AlSawaftah, N. M., Awad, N. S., Pitt, W. G. & Husseini, G. A. pH-Responsive Nanocarriers in Cancer Therapy. *Polymers (Basel)* **14**, 936 (2022).

136. Sana, B., Finne-Wistrand, A. & Pappalardo, D. Recent development in near infrared light-responsive polymeric materials for smart drug-delivery systems. *Materials Today Chemistry* **25**, 100963 (2022).

137. J. Kemp, S., Matthew Ferguson, R., P. Khandhar, A. & M. Krishnan, K. Monodisperse magnetite nanoparticles with nearly ideal saturation magnetization. *RSC Advances* **6**, 77452–77464 (2016).

138. Xu, Z., Shen, C., Hou, Y., Gao, H. & Sun, S. Oleylamine as Both Reducing Agent and Stabilizer in a Facile Synthesis of Magnetite Nanoparticles. *Chem. Mater.* **21**, 1778–1780 (2009).

139. Sun, S. *et al.* Monodisperse MFe_2O_4 (M = Fe, Co, Mn) Nanoparticles. *J. Am. Chem. Soc.* **126**, 273–279 (2004).

140. LaGrow, A. P. *et al.* Unravelling the growth mechanism of the co-precipitation of iron oxide nanoparticles with the aid of synchrotron X-Ray diffraction in solution. *Nanoscale* **11**, 6620–6628 (2019).

141. Storozhuk, L. *et al.* Stable Iron Oxide Nanoflowers with Exceptional Magnetic Heating Efficiency: Simple and Fast Polyol Synthesis. *ACS Appl. Mater. Interfaces* **13**, 45870–45880 (2021).

142. Magnetite R061111 - RRUFF Database: Raman, X-ray, Infrared, and Chemistry. https://rruff.info/magnetite/R061111 (accessed 23/09/2022).

143. Holzwarth, U. & Gibson, N. The Scherrer equation versus the 'Debye-Scherrer equation'. *Nature Nanotech.* **6**, 534–534 (2011).

144. Obaidat, I. M., Issa, B. & Haik, Y. Magnetic Properties of Magnetic Nanoparticles for Efficient Hyperthermia. *Nanomaterials (Basel)* **5**, 63–89 (2015).

145. Harman, C. L. G. *et al.* Controlled synthesis of SPION@SiO_2 nanoparticles using design of experiments. *Mater. Adv.* **3**, 6007–6018 (2022).

146. Ureña-Horno, E., Kyriazi, M.-E. & Kanaras, A. G. A method for the growth of uniform silica shells on different size and morphology upconversion nanoparticles. *Nanoscale Adv.* **3**, 3522–3529 (2021).

147. Han, Y. *et al.* Unraveling the Growth Mechanism of Silica Particles in the Stöber Method: In Situ Seeded Growth Model. *Langmuir* **33**, 5879–5890 (2017).

148. Chigrinova, M. *et al.* Rearrangements and addition reactions of biarylazacyclooctynones and the implications to copper-free click chemistry. *Org. Biomol. Chem.* **11**, 3436–3441 (2013).

149. Kotagiri, N. *et al.* Antibody Quantum Dot Conjugates Developed via Copper-Free Click Chemistry for Rapid Analysis of Biological Samples Using a Microfluidic Microsphere Array System. *Bioconjugate Chem.* **25**, 1272–1281 (2014).

150. Nanoparticle Volume, Mass and Concentration. *nanoComposix* https://nanocomposix.com/pages/nanoparticle-volume-mass-and-concentration (accessed 08/07/2024).

151. Chircov, C. *et al.* Iron Oxide–Silica Core–Shell Nanoparticles Functionalized with Essential Oils for Antimicrobial Therapies. *Antibiotics (Basel)* **10**, 1138 (2021).

152. Hendel, T. *et al.* In Situ Determination of Colloidal Gold Concentrations with UV–Vis Spectroscopy: Limitations and Perspectives. *Anal. Chem.* **86**, 11115–11124 (2014).

153. Kimoto, S. *et al.* Characterization of nanosized silica size standards. *Aerosol Sci. Technol.* **51**, 936–945 (2017).

154. Tm Calculator | Oligo melting temperature. https://www.promega.co.uk/resources/tools/biomath/tm-calculator/ (accessed 11/06/2025).

155. Munneke, S., Kodar, K., Painter, G. F., Stocker, B. L. & Timmer, M. S. M. The modular synthesis of multivalent functionalised glycodendrons for the detection of lectins including DC-SIGN. *RSC Adv.* **7**, 45260–45268 (2017).

156. Liu, B. & Liu, J. Freezing Directed Construction of Bio/Nano Interfaces: Reagentless Conjugation, Denser Spherical Nucleic Acids, and Better Nanoflares. *J. Am. Chem. Soc.* **139**, 9471–9474 (2017).

157. Hao, Y., Li, Y., Song, L. & Deng, Z. Flash Synthesis of Spherical Nucleic Acids with Record DNA Density. *J. Am. Chem. Soc.* **143**, 3065–3069 (2021).

158. Holmes, T. R. & Paller, A. S. Gene Regulation Using Spherical Nucleic Acids to Treat Skin Disorders. *Pharmaceuticals* **13**, 360-364 (2020).

159. Zhao, Y., Wang, Z., Zhang, W. & Jiang, X. Adsorbed Tween 80 is unique in its ability to improve the stability of gold nanoparticles in solutions of biomolecules. *Nanoscale* **2**, 2114–2119 (2010).

160. Horny, M.-C., Dupuis, V., Siaugue, J.-M. & Gamby, J. Release and Detection of microRNA by Combining Magnetic Hyperthermia and Electrochemistry Modules on a Microfluidic Chip. *Sensors* **21**, 185 (2021).

161. Saiyed, Z. M., Ramchand, C. N. & Telang, S. D. Isolation of genomic DNA using magnetic nanoparticles as a solid-phase support. *J. Phys. Condens. Matter* **20**, 204153 (2008).

162. Zhao, Z. *et al.* A simple magnetic nanoparticles-based viral RNA extraction method for efficient detection of SARS-CoV-2. *BioRxiv* doi.org/10.1101/2020.02.22.961268 (2020).

163. Xu, J. *et al.* A one step method for isolation of genomic DNA using multi-amino modified magnetic nanoparticles. *RSC Adv.* **11**, 3324–3332 (2021).

164. Spitzmüller, L. *et al.* Dissolution control and stability improvement of silica nanoparticles in aqueous media. *J. Nanopart. Res.* **25**, 40-57 (2023).

165. Carlson, E. D., Gan, R., Hodgman, C. E. & Jewett, M. C. Cell-free protein synthesis: Applications come of age. *Biotechnology Advances* **30**, 1185–1194 (2012).

166. Swartz, J. Developing cell-free biology for industrial applications. *JIMB* **33**, 476–485 (2006).

167. Caschera, F. Cell-free protein synthesis platforms for accelerating drug discovery. *Biotechnology Notes* **6**, 126–132 (2025).

168. He, M., Stoevesandt, O. & Taussig, M. J. *In situ* synthesis of protein arrays. *Curr. Opin. Biotechnol.* **19**, 4–9 (2008).

169. Borkowski, O. *et al.* Large scale active-learning-guided exploration for in vitro protein production optimization. *Nat. Commun.* **11**, 1872-1880 (2020).

170. Morita, E. H., Sawasaki, T., Tanaka, R., Endo, Y. & Kohno, T. A wheat germ cell-free system is a novel way to screen protein folding and function. *Protein Sci.* **12**, 1216–1221 (2003).

171. Takai, K., Sawasaki, T. & Endo, Y. Development of Key Technologies for High-Throughput Cell-Free Protein Production with the Extract from Wheat Embryos. in *Advances in Protein Chemistry and Structural Biology* (ed. Joachimiak, A.) vol. 75 53–84 (Academic Press, 2008).

172. Hunt, A. C. *et al.* A rapid cell-free expression and screening platform for antibody discovery. *Nat. Commun.* **14**, 3897-3911 (2023).

173. Tsuboyama, K. *et al.* Mega-scale experimental analysis of protein folding stability in biology and design. *Nature* **620**, 434–444 (2023).

174. Zawada, J. F. *et al.* Cell-free technologies for biopharmaceutical research and production. *Current Opinion in Biotechnology* **76**, 102719 (2022).

175. Cai, Q. *et al.* A simplified and robust protocol for immunoglobulin expression in scherichia coli cell-free protein synthesis systems. *Biotechnology Progress* **31**, 823–831 (2015).

176. Topouzis, S. *et al.* Novel drugs approved by the EMA, the FDA and the MHRA in 2024: A year in review. *Br. J. Pharmacol.* **182**, 1416–1445 (2025).

177. Kanter, G. *et al.* Cell-free production of scFv fusion proteins: an efficient approach for personalized lymphoma vaccines. *Blood* **109**, 3393–3399 (2006).

178. Lu, Y., Chan, W., Ko, B. Y., VanLang, C. C. & Swartz, J. R. Assessing sequence plasticity of a virus-like nanoparticle by evolution toward a versatile scaffold for vaccines and drug delivery. *PNAS* **112**, 12360–12365 (2015).

179. Siquenique, S., Ackerman, S., Schroeder, A. & Sarmento, B. Bioengineering lipid-based synthetic cells for therapeutic protein delivery. *Trends in Biotechnology* **43**, 348–363 (2025).

180. Filonov, G. S., Moon, J. D., Svensen, N. & Jaffrey, S. R. Broccoli: Rapid Selection of an RNA Mimic of Green Fluorescent Protein by Fluorescence-Based Selection and Directed Evolution. *J. Am. Chem. Soc.* **136**, 16299–16308 (2014).

181. Kukarin, A., Rong, M. & McAllister, W. T. Exposure of T7 RNA Polymerase to the Isolated Binding Region of the Promoter Allows Transcription from a Single-stranded Template. *JBC* **278**, 2419–2424 (2003).

182. Rong, M., Durbin, R. K. & McAllister, W. T. Template Strand Switching by T7 RNA Polymerase. *JBC* **273**, 10253–10260 (1998).

183. Ahmadi, M., A. Ritter, C., Woedtke, T. von, Bekeschus, S. & Wende, K. Package delivered: folate receptor-mediated transporters in cancer therapy and diagnosis. *Chem. Sci.* **15**, 1966–2006 (2024).

184. Jose, A., Ninave ,Kunal Manoj, Karnam ,Sriravali & and Venuganti, V. V. K. Temperature-sensitive liposomes for co-delivery of tamoxifen and imatinib for synergistic breast cancer treatment. *J. Liposome Res.* **29**, 153–162 (2019).

185. Liu, W.-X. *et al.* Dynamic multiphase semi-crystalline polymers based on thermally reversible pyrazole-urea bonds. *Nat. Commun.* **10**, 4753-4761 (2019).

186. Pashkovskaya, A. *et al.* Light-Triggered Liposomal Release: Membrane Permeabilization by Photodynamic Action. *Langmuir* **26**, 5726–5733 (2010).

187. Luo, D. *et al.* Rapid Light-Triggered Drug Release in Liposomes Containing Small Amounts of Unsaturated and Porphyrin–Phospholipids. *Small* **12**, 3039–3047 (2016).

188. Rwei, A. Y. *et al.* Repeatable and adjustable on-demand sciatic nerve block with phototriggerable liposomes. *PNAS* **112**, 15719–15724 (2015).

189. Sine, J. *et al.* Photo activation of HPPH encapsulated in "Pocket" liposomes triggers multiple drug release and tumor cell killing in mouse breast cancer xenografts. *Int. J. Nanomedicine* **10**, 125–145 (2015).

190. Cui, Z.-K. *et al.* Nonphospholipid Fluid Liposomes with Switchable Photocontrolled Release. *Langmuir* **30**, 10818–10825 (2014).

191. Tabuchi, T. & Yokobayashi, Y. High-throughput screening of cell-free riboswitches by fluorescence-activated droplet sorting. *Nucleic Acids Res.* **50**, 3535–3550 (2022).

192. Maloney, E. & Duffy, D. Deciphering the relationship between temperature and immunity. *Discov. Immunol.* **3**, kyae001 (2024).

193. Moschetta, A., Frederik, P. M., Portincasa, P., van Berge-Henegouwen, G. P. & van Erpecum, K. J. Incorporation of cholesterol in sphingomyelin- phosphatidylcholine vesicles has profound effects on detergent-induced phase transitions. *J. Lipid Res.* **43**, 1046–1053 (2002).

194. Dragan, A. I. *et al.* Characterization of PicoGreen Interaction with dsDNA and the Origin of Its Fluorescence Enhancement upon Binding. *Biophys. J.* **99**, 3010–3019 (2010).

195. Samanta, A., Zhou, Y., Zou, S., Yan, H. & Liu, Y. Fluorescence Quenching of Quantum Dots by Gold Nanoparticles: A Potential Long Range Spectroscopic Ruler. *Nano Lett.* **14**, 5052–5057 (2014).

196. Tatarinov, A., Sarvazyan, N. & Sarvazyan, A. Use of multiple acoustic wave modes for assessment of long bones: model study. *Ultrasonics* **43**, 672–680 (2005).

197. Culjat, M. O., Goldenberg, D., Tewari, P. & Singh, R. S. A Review of Tissue Substitutes for Ultrasound Imaging. *Ultrasound Med. Biol.* **36**, 861–873 (2010).

198. Clarke, A. J., Evans, J. A., Truscott, J. G., Milner, R. & Smith, M. A. A phantom for quantitative ultrasound of trabecular bone. *Phys. Med. Biol.* **39**, 1677–1687 (1994).

199. Song, L. *et al.* Structure of Staphylococcal α-Hemolysin, a Heptameric Transmembrane Pore. *Science* **274**, 1859–1865 (1996).

200. Wurbs, A. *et al.* A human ex vivo skin model breaking boundaries. *Sci. Rep.* **14**, 24054 (2024).

201. 3'-Uaq Cap CPG. https://www.glenresearch.com/duplex-stability/3-uaq-cap-cpg20-2980.html (accessed on 07/07/2025).

202. Seidel, K. *et al.* Synthesis of Magnetic-Nanoparticle/Ansamitocin Conjugates—Inductive Heating Leads to Decreased Cell Proliferation In Vitro and Attenuation Of Tumour Growth In Vivo. *Chemistry – A European Journal* **23**, 12326–12337 (2017).

203. Wacker, J. B., Lignos, I., Parashar, V. K. & Gijs, M. A. M. Controlled synthesis of fluorescent silica nanoparticles inside microfluidic droplets. *Lab Chip* **12**, 3111–3116 (2012).

204. Hua, H. *et al.* Targeting Akt in cancer for precision therapy. *J. Hematol. Oncol.* **14**, 128 (2021).

205. Zhejiang Haichang Biotech Co., Ltd. *A Phase I, First in Human, Open-Label, Dose-Escalation Study to Evaluate the Safety, Tolerability, and Pharmacokinetics of WGI-*

0301, a Lipid Nanoparticle Suspension of Akt-1 Antisense Oligonucleotide, in Patients With Advanced Solid Tumors. https://clinicaltrials.gov/study/NCT05267899 (2023).

206. National Cancer Institute (NCI). *A Phase I Study of Antisense Bcl-2 Oligonucleotide (G3139) in Combination With Carboplatin and Paclitaxel in Patients With Advanced Solid Tumors*. https://clinicaltrials.gov/study/NCT00054548 (2013).

207. Moulder, S. L. *et al.* Phase I/II Study of G3139 (Bcl-2 Antisense Oligonucleotide) in Combination with Doxorubicin and Docetaxel in Breast Cancer. *Clin. Cancer Res.* **14**, 7909–7916 (2008).

208. Chia, S. *et al.* Phase II Trial of OGX-011 in Combination with Docetaxel in Metastatic Breast Cancer. *Clin. Cancer Res.* **15**, 708–713 (2009).

209. Zhang, H. *et al.* Clusterin inhibits apoptosis by interacting with activated Bax. *Nat. Cell Biol.* **7**, 909–915 (2005).

210. Çakan, E. *et al.* Therapeutic Antisense Oligonucleotides in Oncology: From Bench to Bedside. *Cancers (Basel)* **16**, 2940-2975 (2024).

211. Yanagidaira, M. *et al.* Effects of combinations of gapmer antisense oligonucleotides on the target reduction. *Mol. Biol. Rep.* **50**, 3539–3546 (2023).

212. Shaikh, S. *et al.* Intermittent alternating magnetic fields diminish metal-associated biofilm in vivo. *Sci. Rep.* **13**, 22456-22468 (2023).

213. Goldufsky, J. *et al.* Pseudomonas aeruginosa exotoxin T induces potent cytotoxicity against a variety of murine and human cancer cell lines. *J. Med. Microbiol.* **64**, 164–173 (2015).

214. Haueis, L., Stech, M. & Kubick, S. A Cell-free Expression Pipeline for the Generation and Functional Characterization of Nanobodies. *Front. Bioeng. Biotechnol.* **10**, 1-11 (2022).

215. Johnson, K. C. C. *et al.* The survival benefit of adjuvant trastuzumab with or without chemotherapy in the management of small (T1mic, T1a, T1b, T1c), node negative HER2+ breast cancer. *NPI Breast Cancer* **10**, 49-57 (2024).

216. Verherstraeten, S. *et al.* Perfringolysin O: The Underrated Clostridium perfringens Toxin? *Toxins* **7**, 1702–1721 (2015).

217. Ashford, M. B., England, R. M. & Akhtar, N. Highway to Success—Developing Advanced Polymer Therapeutics. *Advanced Therapeutics* **4**, 2000285 (2021).

218. England, R. M., Moss, J. I., Gunnarsson, A., Parker, J. S. & Ashford, M. B. Synthesis and Characterization of Dendrimer-Based Polysarcosine Star Polymers: Well-Defined, Versatile Platforms Designed for Drug-Delivery Applications. *Biomacromolecules* **21**, 3332–3341 (2020).